Title

Transformation of Canonical Helicity under the Collision and Merging of Two Magnetic Flux Ropes

Author

DeHaas, Timothy Alexander

Publication Date

2017

UNIVERSITY OF CALIFORNIA

Los Angeles

Transformation of Canonical Helicity under the Collision and Merging of Two Magnetic Flux Ropes

A dissertation submitted in partial satisfaction
of the requirements for the degree
Doctor of Philosophy in Physics

by

Timothy Alexander DeHaas

2017

ABSTRACT OF THE DISSERTATION

Transformation of Canonical Helicity under the Collision and Merging of Two Magnetic Flux Ropes

by

Timothy Alexander DeHaas
Doctor of Philosophy in Physics
University of California, Los Angeles, 2017
Professor Walter N Gekelman, Chair

Magnetic helicity, a measure of the linkage of magnetic field lines, has long been used in the contexts of astrophysical and experimental plasmas because, for highly conductive plasmas, it is a conserved quantity. In this experimental study, the dynamics of two magnetic flux ropes and the magnetic reconnection that occurs between them is used as a proving ground for helicity conservation theory. A magnetic flux rope is a twisted bundle of magnetic field lines that is ubiquitous in space and solar plasmas. Two magnetic flux ropes are created in the Large Plasma Device (LAPD) using a lanthanum hexaboride (LaB_6) cathode that injects current along a background, magnetic field. The flux ropes are kink unstable, causing them to collide. As they collide, the field lines diverge, and a quasi-separatrix layer (QSL) forms. The QSL is an indicator of magnetic field line reconnection. Helicity conservation is examined inside the QSL. Two types of helicity are considered: relative magnetic helicity, which is a standard formulation, and relative canonical helicity, an extension. Three-dimensional measurements of plasma density (n_e), electron temperature (T_e), plasma potential (ϕ_p), the magnetic field ($\mathbf{B}$), and ion flow ($\mathbf{v}_{\mathrm{flow}}$) are required to evaluate each terms that appear in the extended formulation of helicity. In the magnetohydrodynamic (MHD) limit, the transport of relative magnetic helicity and the dissipation of relative magnetic helicity do not balance. Using relative canonical helicity, the dissipation of relative canonical helicity is balanced by the transport of relative canonical helicity into the QSL – such that the temporal derivative of the quantity is zero. The electrostatic field is the key term that balances helicity. It is ignored in the standard model of helicity. In this experiment, the electrostatic component of the electric field is large compared to the induced electric field produced by reconnection; and therefore, it should not be ignored in other circumstances.

The dissertation of Timothy Alexander DeHaas is approved.

Richard E Wirz

George J Morales

Troy A Carter

Walter N Gekelman, Committee Chair

University of California, Los Angeles

2017

To my daughter, Reagan Alexandrine DeHaas

TABLE OF CONTENTS

1 Introduction 1

1.1 Introductory Remarks 1

1.2 Astrophysical Flux Ropes 2

1.3 Experimental Flux ropes 6

1.4 Kink-Driven Dynamics 7

1.5 Incoherent Behavior 11

1.6 Canonical Helicity 12

1.7 Dissertation Objective and Outline 14

2 Experimental Method 16

2.1 The Large Plasma Device 16

2.2 Flux Rope Generation 19

2.3 Diagnostics 22

  2.3.1 Langmuir Probes 23

  2.3.2 Magnetic Probes 27

  2.3.3 Emissive Probes 28

  2.3.4 Mach Probes 29

2.4 Three-Dimensional Reconstruction 31

3 Structure of the Magnetic Flux Rope 35

3.1 Introductory Remarks 35
3.2 Magnetic Field and Current Density 36
3.3 Temperature and Density 38
3.4 MHD Equilibrium 40
3.5 Electric Field 42
3.6 Ion Flow 45
3.7 Concluding Remarks 47

4 Orbital Rotation of the Flux Rope 48

4.1 The Kink Instability 48
4.2 Transition into Unstable Mode 51
4.3 Model of Coherent Rotation 55
4.4 Absolute Displacement 58
4.5 Application to the Two Flux Rope System 61

5 Characteristic Pulses and Chaotic Motion 63

5.1 Transition in Signals 63
5.2 Fluctuation Power Spectrum 66
5.2 Incoherent Signals 71
5.4 Complexity-Entropy Mapping 74

6 Canonical Helicity 79

6.1 Introduction. 79

6.2 Two Flux Rope Interaction 80

6.3 Identification of Magnetic Reconnection 81

6.4 Measurement of Relative Magnetic Helicity 84

6.5 Canonical Helicity 89

6.6 Summary. 96

7 Conclusion 98

7.1 Summary of Results 98

Appendix A: Frequency Scaling of Coherent Rotation 102

A.1 Introductory Remarks 102

A.2 Scaling with Magnetic Field 102

A.3 Scaling with Length. 103

A.4 Scaling with Mass Density 104

A.5 Testing of Coherent Frequencies 106

A.5.1 Electrostatically Driven Kink Rotation. 106

A.5.2 Ion Flow 109

A.5.3 Modified Boundary Conditions 110

A.5.4 Bulk Resistivity. 113

A.6 Summary of Appendix. 115

References 117

LIST OF FIGURES

Fig 1.1 An experimental, magnetic flux rope. A magnetic flux ropes is a bundle of twisted magnetic field lines, shown here as tubes of blue. The flux rope is linear with a radius of 3.75 cm and a length of 11 m. In experimental devices, flux ropes are generated by injected electron current along an external, background magnetic field. In this dissertation, the flux ropes are generated in the same way. The tubes in purple signify the path of the spiraling currents around the background magnetic field 2

Fig 2.1 A schematic of the Large Plasma Device (LAPD). Four turbo pumps evacuate the chamber to a base pressure of $<10^{-6}$ Torr. A single working gas of He is introduced into the system at 3×10^{-5} Torr, which is then ionized using a cathode-anode discharge. This BaO cathode is shown to the left. The discharge creates a ambient plasma medium 20 m in length and 60 cm in diameter. A secondary cathode-anode pair is placed on the far end of the device (to the right). A mask is placed between the LaB_6 source and its anode (located several meters away) such that electrons are only emitted from what hole is cut into the mask. This can be used to create one or more flux ropes. The flux ropes are typically 11 m long and 5 cm in diameter 17

Fig 2.2 Current discharges associated with the two cathode-anode sources. The BaO source is pulsed with 40 V, producing a current discharge that peaks at approximately 4 kA. The LaB_6 trace is the discharge for two flux ropes ($a = 3.5$ cm, $L = 1100$ cm each), which peaks at 750 A. The LaB_6 cathode is triggered at $t = 0$ ms and operates for 6 ms during the BaO discharge . . 18

Fig 2.3 A comparison between the two flux rope sources used in the series of experiments presented here. **(a)** A smaller LaB_6 cathode that is directly masked to produce a flux rope that is 5 cm in diameter. The mask is not shown in the figure. **(b)** A larger LaB_6 that is not directly masked. Instead a mask is placed 64 cm away from the cathode. Multiple flux rope configurations have been designed using this cathode 20

Fig 2.4 A cross-sectional sketch of the LAPD. The figure demonstrates the probe motion and data acquisition method in the device. An automated probe drive changes the angle θ and insertion distance into the LAPD vacuum chamber. The probe shaft slides on a double O-ring seal to prevent breaking vacuum. The probe moves in a grid between successive discharges to assemble volumetric dataset point for point 23

Fig 2.5 A collection of the probe diagnostics used in the Large Plasma Device: The Langmuir probe, a small metallic collector variably biased to collect or repel free-floating charged particles. A magnetic pickup loop used to measure the magnetic field by Faraday's law. An Emissive probe, which floats at the plasma potential when the tip is sufficiently emissive. A Mach Probe, a set of particularly oriented collectors to infer ion flow in the plasma 25

Fig 2.6 **(a)** Time resolved measurement of plasma density at (x,y,z = 5, 0, 160 cm). As the kink unstable flux rope passes this location, a spike in the density is observed. From such time traces, the density of the core of the flux rope and the ambient medium can be inferred. **(b)** Time resolved measurement of plasma temperature at (x,y,z = 5, 0, 160 cm). As the kink unstable flux rope passes this location, a spike in the temperature is observed. From such time traces, the density of the core of the flux rope and the ambient medium can be inferred 26

Fig 2.7 Ten consecutive time traces of magnetic signals from the fixed probe. **(a)** is the representation of the un-aligned signals using a standard trigger. **(b)** is the representation of aligned signals using conditional triggering. The conditional trigger is valid for a certain length of time before the signal becomes decorellated 32

Fig 3.1 The **(a)** magnetic field and **(b)** current density profile for a flux rope (a = 3.75 cm, L=1100 cm, B_z = 330 G, I_{FR} = 300 A) at z = 64 cm and t = 4.75 ms. **(c)** A x-y cross section of the two flux rope current densities at z = 64 cm. The dashed line indicates the lineout used in (a) and (b) 36

Fig 3.2 Parallel current density (J_z) at various axial location (z_{start} = 64 cm, z_{end} = 768 cm, dz = 64 cm) for t = 5.86 ms. The two current channels merge as they approach the anode at z = 1100 cm 37

Fig 3.3 **(a)** The density profile (red) of a single flux rope at z = 64 cm. The values of spatially correlated with J_z (purple). **(b)** The core density of the flux rope scales with the discharge power of the LaB_6 cathode. **(c)** The temperature profile (blue) of a single flux rope at z = 64 cm. The values are spatially correlated with J_z (purple). **(d)** The core temperature of the flux rope scaled with the discharge power of the LaB_6 cathode. 39

Fig 3.4 **(a)** A line profile across one of the flux ropes to demonstration the pressure forces are balanced by the $\mathbf{J}\times\mathbf{B}$ forces at z = 64 cm. **(b)** A cross-section of the flux rope at z = 64 cm. The color table scales with $|\mathbf{J}\times\mathbf{B}|$ while the contours correspond to $|-\nabla P_e|$. The two show good agreement. **(c)** A line profile across one of the flux ropes to demonstration the pressure forces are balanced by the $\mathbf{J}\times\mathbf{B}$ forces at z = 510 cm. **(d)** A cross-section of the flux rope at z = 510 cm. The color table scales with $|\mathbf{J}\times\mathbf{B}|$ while the contours correspond to $|-\nabla P_e|$. The two show good agreement 41

Fig 3.5 **(a)** The plasma potential inside the two flux ropes at z = 64 cm and t = 5.45 ms. The electric field vectors point toward the center of each rope. **(b)** The plasma potential inside the two flux ropes at z = 510 cm and t = 5.45 ms. The electric field vectors point toward the center of each rope 43

Fig 3.6 **(a)** The plasma potential measured by the emissive probe at (x,y,z) = (5,0,160) cm for a single LAPD discharge (I = 95 A, V = 100 V). As the flux rope passes by the probe, a drop in the plasma potential is observed. **(b)** The scaling of the core plasma potential as a function of discharge current 44

Fig 3.7 An x-y cross-section of a single flux rope at z = 332 cm. The figure shows the axial Mach flow. A lineout is presented above the figure and peaks at 0.25, corresponding to approximately 3.7×10^5 cm/s 46

Fig 3.8 **(a)** The perpendicular ion flow at z = 510 cm and t = 5.45 ms. The ions spiral around the two flux rope in the $\mathbf{E}\times\mathbf{B}$ direction and reach a maximum of approximately $\mathrm{v}_\perp/c_s$ ~ 0.5. **(b)** The vorticity associated with (a). The values are normalized to the background magnetic field to show that the contribution of vorticity to ion canonical vorticity is up to 40% 47

Fig 4.1 A cartoon demonstrating the "gentle wiggle" which Eq. 4.1 describes. The dashed circle represents the equilibrium position of the flux rope in the x-y plane while the solid curve shows the cross-section of the flux rope as it is displaced $|\eta|$, from the equilibrium position 49

Fig 4.2 **(a)** A magnetic time trace at (x, y, z) = (3, 0, 850) cm for a flux rope I = 20 A, L = 1100 cm, and B_0 = 660 G. The current in the rope is below the threshold needed to trigger the kink instability. The oscillations (15 kHz) correspond to standing Alfvén waves. **(b)** A magnetic time trace at (x, y, z) = (3, 0, 850) cm for a flux rope I = 75 A, L = 1100 cm and B_0 = 660 G. The current in the rope is above the threshold needed to trigger the kink instability. The oscillations correspond to the "rotation helical equilibrium." 52

Fig 4.3 The transition of the flux rope into coherent rotation. This mode is associated with the kink instability, which is triggered at $I_{KS}/2$. Once the mode is initiated, its frequency scales with the current in the rope – then saturates . 53

Fig 4.4 **(**The frequency spectrum for a flux rope (a = 2.5 cm, L = 1100 cm, B_0 = 330 G). The flux rope is kink unstable and undergoes coherent rotation of the plasma column in the x-y plane. The coherent mode is the lower peak in the spectrum while its harmonics are produced by displacement on the order of the radius of the rope. **(b)** The instantaneous central position of the flux rope over several rotations about the axis. **(c)** The filtered frequencies seen in the spectrum. The spatial feature show m=1,2,3… oscillations in the plane such that $\tilde{B} = B(r)e^{i(m\theta-\omega_m t)}$ 54

Fig 4.5 Using simple circular motion of the plasma column as a model to explain the observed harmonics, the predicted (the solid curves) and observed amplitudes (the square points) are plotted 57

Fig 4.6 **(a)** A magnetic time trace at (x, y, z) = (3, 0, 850) cm for a flux rope of 75 A and 60 V. The small oscillations in the signal are a function of the displacement of the flux rope from its axis. **(b)** A magnetic time trace at (x, y, z) = (3, 0, 850) cm for a flux rope of 75 A and 175 V. The large oscillations in the signal are a function of the displacement of the flux rope from its axis, demonstrating the displacement of the column varies with the discharge voltage independent of current 59

Fig 4.7 The amplitude of oscillations observed from a fixed magnetic probe: (x, y, z) = (3, 0, 850) cm. This amplitude is a placeholder for the displacement of the flux rope from its axis. The displacement scales with discharge power, which is demonstrated by plotting two sets of data: 1) where current is fixed and the discharge voltage is varied and 2) where the discharge voltage is fixed and the current is varied. When the displacement of the flux rope becomes greater than the radial position of the probe, the amplitude of oscillations saturates. . . 61

Fig 5.1 A comparisons between of the types of magnetic signal seen in this dissertation: **(a)** Coherent oscillations (f_{FR} = 4 kHz) which signify a rotating helical equilibrium. **(b)** The same phenomena; however, the has increased frequency (f_{FR} = 6 kHz) due to its scaling with the current in the flux ropes. **(c)** A transition of the signals in a more incoherent, intermitted mode 64

Fig 5.2 The power spectrum associated with the three magnetic time traces shown in

Figure 5.1. The spectrum is presented on a log-linear plot to show the rise in the underlying background as the current in the flux rope increases 66

Fig 5.3 **(a)** The time derivative of Figure 5.1a. The sharp spikes in the signal excite a broad range of frequencies. **(b)** A small portion of the magnetic signal from Figure 5.1a. **(c)** The wavelet transformation of Figure 5.1a. A flux rope exhibited a strong coherent mode at 4 kHz. As the flux rope passes the probe, there is the regular excitation of higher frequencies 68

Fig 5.4 A comparison between the I_{isat} and $\dot{\mathbf{B}}$ at the same location (x,y,z = 5,0,870 cm) for a flux rope I_{FR} = 55 A, B_z = 330 G, and L = 1100 cm. The signals are well correlated in time and space. In this way, $\dot{\mathbf{B}}$ reveal information about the position of the flux rope 69

Fig 5.5 **(a)** The spectrum of magnetic b-dot signals associated with the three time trace in Figure 5.1. The temporal derivate may be interpreted as a spatially varying electric field inside the flux rope. The data is fit to Eq. 5.1. The shape of the background is produced by the shape of characteristic pulses in the data. **(b)** The pulse shape was derived using the fit in (a) and is overlaid on the data for a flux rope of 75 A. **(c)** Using the fit in (a), the derived pulse from the spectrum is overlaid on the data for a flux rope of 130 A. The “skewness “ of the data is not preserved in the spectrum 70

Fig 5.6 The time derivative of Figure 5.1c (I_{FR} =130 A). The sharp spikes in the signal excite a board range of frequencies. These pulses are not evenly space; however, they do have a preferential direction 72

Fig 5.7 The average number of pulses in $\dot{B}_x$ and $\dot{B}_y$ at $z =$ 1060 cm. The figure is presented as a vector field with the number of pulses in $\dot{B}_x$ being the x-component of the vectore and the number of pulses in $\dot{B}_y$ being the y-component of the vector. Negative values in reflect negative pulses on average while positive values indicate positive pulses on average 73

Fig 5.8 The Complex-Entropy Plane for a single flux rope at varying currents. Each dot represents the reduction of a single magnetic time trace onto the plane. Between 50A and 100A, the flux rope are kink unstable for a background magnetic field of both **(a)** 330 G and **(b)** 660 G. For this range of currents, the flux rope exhibits strong coherent rotation, indicated by low entropy signals. The points for this range of current is indistinguishable on the plane. For 130 A, the signals transition toward chaos. This is indicated by their position above Fractional Brownian Motion (fBm) 77

Fig 6.1 **(a)** A plot of the squashing factor q at t = 5.6 ms, during a reconnection event. A collection of field lines exhibit large q-values compared to its surroundings. These collection of field lines are called a quasi-separatrix layer. (QSL **(b)** A three-dimensional representation of the QSL. During a reconnection event, a QSL forms between the flux ropes. Magnetic helicity will be considered inside this volume 83

Fig 6.2 *D*, the dissipation of magnetic helicity, as defined in Eq. 6.5, plotted for one period of flux rope rotation (t=5.47-5.87 ms and dt = 50 us). The center frame indicates the time at which the flux ropes collide and a QSL forms. Spatially correlated with the QSL is a tendril of magnetic helicity dissipation, which snakes between the flux ropes 86

Fig 6.3 **(a)** The dissipation and influx of magnetic helicity (Eq. 6.4) into the QSL (q=100). The addition of the two traces yields the time derivative of magnetic helicity, $\frac{\partial K_M}{\partial t}$, during a collision between the two flux ropes. **(b)** The color map represents *D* (Eq. 6.5) calculated at t=5.67 ms. The arrows represent *T* (Eq. 6.8) calculated at t=5.67 ms 88

Fig 6.4 A three-dimensional representation of (electron canonical vorticity, blue) and (ion canonical vorticity, red) at t=5.67. The two fluid approach to helicity, canonical helicity is defined as the self-linkage of these quantities 90

Fig 6.5 A comparison between the amount of electron canonical helicity dissipation inside the QSL due to the terms in $\mathbb{E}_e$: **(a)** from the induced electric field, **(b)** from the electrostatic field, **(c)** from the pressure gradients. The total is plotted in **(d)** 93

Fig 6.6 **(a)** The dissipation and influx of electron canonical helicity (Eq. 6.9) inside the QSL (q=100). The addition of the two traces yields the time derivative of Ke during a collision between the two flux ropes. **(b)** The color map represents the dissipation of electron canonical helicity calculated at t=5.67 ms. The arrows represent the influx of the same quantity inside into the QSL calculated at t=5.67 ms where *T-V* is a Tesla-Volt 94

Fig 6.7 The temporal derivative of ion canonical helicity during the collision of the flux ropes (the peak on the left and their subsequent separation (the peak on the right) **(a)** The dissipation of ion canonical helicity inside the QSL (q=100) according to the volume integral of Eq. 6.11. **(b)** The influx of ion canonical helicity into the QSL calculated using the surface integral of Eq. 6.11. Note: dK_i/dt = a-b~0 95

Fig A.1 The frequency of coherent rotation as a function of the background magnetic field. Two separate flux ropes were generated ($a = 3$ cm, $L = 1100$ cm). The two instances are plotted: 1) for a flux rope of 75 A and 2) a flux rope of 120 A 103

Fig A.2 **(a)** The transition from a stable to and unstable flux rope in an argon background plasma for B_z = 330 G. **(b)** The transition from a stable to and unstable flux rope in an argon background plasma for B_z = 660 G 105

Fig A.3 A presentation of how symmetry in the electric field can be broken and how it can establish a non-zero, volume-averaged, radial electric field. A radial electric field can be created by the deformation of the x-y cross-section. By centripetal forces, a large electric field manifests on the outer edge resulting in a non-zero electric field in the plane 107

Fig A.4 **(a)** The volume-averaged electric field vector over several periods of flux rope rotation from $t = 4$ ms to $t = 5$ ms. The vector rotates with the flux rope and produces $\mathbf{E}\times\mathbf{B}$ estimates of 2 to 10 kHz **(b)** The instantaneous current density profile as it moves in a circle around the equilibrium position. The current profile deformed into a moon shape. 108

Fig A.5 **(a)** Three dispersion relations associated with three boundary conditions: a fixed-free boundary condition (Eq. 4.3), a vibrating rod with a free end (Eq. A.11), and a boundary condition with finite sheath resistance $\kappa \sim 1$ at the anode (Eq. A.9). The data is placed on top of these curves to demonstrate incompatibility 112

Fig A.6 A comparison between the observed rotation of a magnetic flux rope (a=3 cm, L=1100 cm) and the frequencies predicted by Eq. 4.25 as a function of background magnetic field. The frequencies scale with the Alfvén velocity. The two curves cross because of an increase in the density for elevated discharge currents. 114

LIST OF TABLES

Tbl 2.1 A review of the temporal-spatial scale lengths for the experiment 21

ACKNOWLEDGMENT

I would like to first thank my advisor, Professor Walter Gekelman. I met Walter on the day of his invited talk at the APS-DPP conference in Chicago. He may not remember our conversation; but on that day, he encouraged me to apply to the PhD program at UCLA. I never imagined how closely we would work. I am truly appreciative of his daily guidance and of every opportunity he has given me. I am a better physicist because of him.

I want to acknowledge my PhD committee members – Professor George Morales, Professor Troy Carter, and Professor Richard Wirz – for their careful review of this dissertation as well as their direction over the years. In addition, I appreciate Professor Morales for teaching the graduate student course on plasma physics.

I would be remiss if I did not thank the scientists and staff of BAPSF for their invaluable help: Bart Van Compernolle, who taught me how to do a flux rope experiment and who opened values for me in the middle of the night; Steve Vincena, for his discussions of Star Trek (and plasma physics); Shreekrishna Tripathi, who kept me company when I stayed at the lab too late and whose precision and carefulness in the laboratory is an inspiration; Pat Pribyl, whose expertise is so valuable that I was constantly looking for him. I would like to acknowledge Zoltan Lucky, Marvin Drandell, and Tai Le for their skills. I would like to give a warm thanks to Meg Murphy for letting me vent my frustrations even as I stole her a coffee pot.

I was very fortunate to have awesome peers. I would like to thank Chris Cooper, who mentored me in my 0th year and whose desk I stole. I will never forget Yuhou Wang, the best cubicle-mate that ever was and ever will be. She was a model graduate student and physicist. I am ever grateful to Nathan Moore, who host game nights; Jeff Bonde, whose brilliance as a physicist contributed to several pages in this thesis; and Giovanni Rossi, who adds flare to the lab. Additionally, I would like to recognize the long-suffering Michael Martin, who kept me company even when the others had left. Without him, I am only half a scientist. I would finally like to thank b'Shawn Tang for allowing me to pick on him as the younger graduate student and for mentoring the 180E students when I was too busy writing this dissertation. I wish him the best of luck on his PhD. He is now heir to the flux rope.

My family has been incredibly encouraging and supportive during my time as a graduate student. To my beautiful wife, Yanting Chen DeHaas, I wish to convey my love. I look forward to the exciting days ahead of us. To my parents, your love and enormous sacrifices have made me the man I am today. I own a debt of gratitude to Yongxuan Chen and Kaojun Yang. They have made a home for me in Los Angeles by treating me as their own son. I would like to show my pride as a father. My daughter, to whom I dedicate this work, inspires me.

Additionally, I would like to show my heartfelt gratitude toward Brownie Sifain and Dev Khaitan for keeping me connected to my Rochester home. I wish them both the greatest success on their own dissertations. I appreciate Dr. Fred Marshall, who first

introduced me to plasma physics research. Finally, I would like to thank Glenn Eksaa, my middle school science teacher. I still can recall his classes on Newton's Law of Motion. Without his tireless effort as a teacher, I would not be a physicist.

Funding for this research comes from the Department of Energy: Office of Fusion Energy Science, the National Science Foundation, and the University of California.

VITA

2007–2011	B.S. Physics, B.S. Applied Mathematics University of Rochester
2011–2017	Teaching Assistant Department of Physics and Astronomy University of California, Los Angeles
2011–2012	M.S. Physics University of California, Los Angeles
2012–2017	Graduate Student Researcher Department of Physics and Astronomy University of California, Los Angeles

PUBLICATIONS

T. DeHaas, W. Gekelman. “Helicity Transformation under the Collision and Merging of Two Magnetic Flux Ropes.” Phys. Plasma, 24, 072108 (2017).

T. DeHaas, W. Gekelman, B. Van Compernolle, “Experimental Study of a Linear/Non-Linear Flux Rope,” Phys. Plasmas, 22, 082118 (2015).

W. Gekelman, **T. DeHaas**, P. Pribyl, S. Vincena, B. Van Compernolle, R. Sydora. “Non-local Ohm’s Law during Collisions of Magnetic Flux Ropes.” Phys. Plasmas, 24, 070701 (2017).

W. Gekelman, **T. DeHaas**, W. Daughton, B. Van Compernolle, T. Intrator, and S. Vincena, “Pulsating Magnetic Reconnection Driven by Three-Dimensional Flux-Rope Interactions,” Phys. Rev. Lett. 116, 235101 (2016).

W. Gekelman, **T. DeHaas**, B. Van Compernolle, W. Daughton, P. Pribyl, S. Vincena and D. Hong, “Experimental Study of the Dynamics of a Thin Current Sheet,” Phys. Scr. 91 054002 (2016).

W. Gekelman, P. Pribyl, Z. Lucky, M. Drandell, D. Leneman, J. Maggs, S. Vincena, B. Van Compernolle, S. K. P. Tripathi, G. Morales, T. A. Carter, Y. Wang, and **T. DeHaas**, “The Upgraded Large Plasma Device, a Machine for Studying Frontier Basic Plasma Physics,” Rev. Sci. Instrum., 87, 025105 (2016).

W. Gekelman, B. Van Compernolle, **T. DeHaas** and S. Vincena, “Chaos in Magnetic Flux Ropes,” Plasma Phys. Control. Fusion 56 (2014).

F.J. Marshall, **T. DeHaas**, V. Yu Glebov. “Charge-Injection Device Performance in the High-Energy-Neutron Environment of Laser-Fusion Experiments,” Rev. Sci. Instrum. 81 10E503 (2010).

CHAPTER 1 – *INTRODUCTION*

1.1 – INTRODUCTORY REMARKS

The magnetic flux rope is a fundamental building block of astrophysical and experimental plasmas. Simple in concept and structure, the magnetic flux rope consists of a bundle of twisted magnetic field lines. To generate such a structure, plasma current is injected along an existing magnetic field. The superposition of the external field and the azimuthal field generated by the current creates a collection of helical, magnetic field lines. This bundle of field lines resembles a rope.

An example of the type of experimental flux rope explored in this work is presented in Figure 1.1. The flux rope is linear – long and thin in form – produced by an electron current embedded in a straight, magnetic field. The figure shows its twisted field lines, which radially vary in pitch, and the path of the spiraling currents used to generate them.

In this dissertation, the conservation of canonical helicity is examined during the collision and reconnection of two magnetic flux ropes. Two side-by-side flux ropes generated by parallel currents in a background magnetic field. The two flux ropes are driven kink unstable and are free to interact in complex ways. As the two flux ropes collide, a small amount of the magnetic field in annihilated and magnetic field line reconnection is triggered. During the process, canonical helicity is examined inside the reconnection region; and conservation of canonical helicity is observed.

Because magnetic flux ropes are so pervasive in solar and astrophysical plasmas, their general structure and evolution has been the subject of scientific research for many decades. In this light, a brief review of the topic will be presented, and the contribution from this research will be summarized.

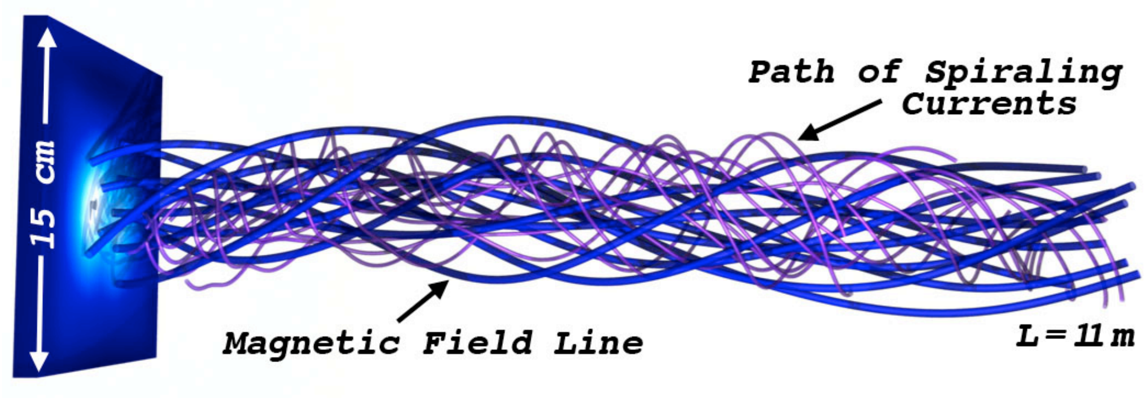

Figure 1.1 – An experimental, magnetic flux rope. A magnetic flux ropes is a bundle of twisted magnetic field lines, shown here as tubes of blue. The flux rope is linear with a radius of 3.75 cm and a length of 11 m. In experimental devices, flux ropes are generated by injected electron current along an external, background magnetic field. In this dissertation, the flux ropes are generated in the same way. The tubes in purple signify the path of the spiraling currents around the background magnetic field.

1.2 – ASTROPHYSICAL FLUX ROPES

Magnetic flux ropes are most commonly associated with astrophysical plasmas. Magnetic flux ropes are ubiquitous and therefore a matter of general interest to space science. A broad review of astrophysical flux ropes in their many space and solar contexts can be found in [Russell 1990].

The first usage of the term “flux rope” appeared as a description of loop-like magnetic structures that were seen extending from the solar surface [Babcock 1961, Alfvén 1963]. Upon closer inspection of UV and X-ray images of the solar atmosphere, these loops were shown to be full of smaller, filamentary structures. The smaller structures retained the name “flux rope” while the larger, loop-like structures became aptly named coronal loops. Observations of coronal loops and magnetic flux ropes continue to be seen by satellites, including the Solar Terrestrial Relations Observatory (STEREO) [Aschwanden 2008], the Transition Region and Coronal Explorer (TRACE) [Golub 1999], and the Atmospheric Imaging Assembly (AIA) [Cirtain 2013]. The scope of these filamentary structures are not isolated to coronal loops; they are also found in solar prominences [Schmieder 1985] and the penumbra of sunspots [Spruit 2006]. These filaments, a fundamental building block of solar structures, are now what is referred to as magnetic flux ropes.

The ubiquity of magnetic flux ropes extends beyond the solar atmosphere. Flux ropes manifest on multiple spatial scales – from the planetary to the interplanetary. For instance, the Cluster mission has confirmed the existence of magnetic flux ropes in the earth’s magnetotail [Slavin 2003]. As the solar wind bends the magnetosphere around the earth, a current sheet forms in Earth’s shadow. This current sheet is believed to tear apart to establish an interwoven fabric of magnetic flux ropes [Øieroset 2011].

Flux ropes have been seen near both Mars and Venus, planetary bodies (unlike Earth) without an intrinsic magnetosphere. An induced magnetic field temporarily forms as the solar wind wraps around the surface or atmosphere of these unmagnetized planets.

Within this temporary magnetosphere, magnetic flux ropes materialize. The Pioneer Venus Orbiter was the first to observe magnetic flux ropes near Venus in the late 1970s [Russel 1979]. In this instance, the flux ropes were and tightly wound, located the only 200 km above the planetary surface. In contrast to these smaller filamentary structures, the Mars Global Surveyor has observed planetary sized flux ropes in Mars' southern hemisphere [Cloutier 1999]. In terms of magnetic field strength, these sizable, stationary flux ropes are the largest measured by *in situ* spacecraft [Beharrell 2012].

On more immense scales, magnetic flux ropes are the brick and mortar of interplanetary magnetic clouds. The term "magnetic cloud" was first coined by [Klein 1982] to describe regions within the solar wind where the magnetic vector field smoothly changed polarity. Analysis determined that the smoothly rotating field of magnetic clouds was the result of the spiraling currents associated with a flux rope [Goldstein 1983, Marubashi 1984, Burlaga 1988]. Interplanetary magnetic flux ropes can be created from a coronal mass ejection (CME), a large release of plasma and magnetic energy from the sun. As a solar prominence erupts and plasma is expelled from the sun, flux ropes anchored to the photosphere are dragged from the solar corona and expand to interplanetary sizes [Marubashi 1997, Chen 1997].

The global behavior of magnetic flux ropes is also of interest because the collision, merging, and tearing of multiple flux ropes can produce bursts of magnetic field line reconnection [Lawrence 2009, Intrator 2009]. During the reconnection process, field line topology rapidly changes as magnetic energy is converted to kinetic energy, thermal energy, and particle acceleration. This process has important consequences for a system of flux ropes and the ambient medium in which they reside. For instance, the solar corona is several orders of magnitude hotter than the surface of the sun [Grotian 1939]. Uncertain as to the cause, theory suggests that the collision and unraveling of multiple flux ropes on the sun contributes to coronal heating above 2 MK [Priest 1976, Akasofu 1979, Parker 1983, Schijver 2007]. The theory is not without basis: The High-resolution Coronal Imager (Hi-C) has observed the release of magnetic energy in the form of strong outflows during the unbraiding of multiple flux ropes [Cirtain 2013]. Observations from the Solar Dynamic Observatory (SDO) – among others – have shown localized regions of coronal heating as multiple flux ropes collide and reconnect [Parnell 1994, Zhang 2012]. These concentrated areas of intense, X-ray emission are known as X-ray bright points.

Often, the manifestation of an X-ray bright point is followed by a coronal mass ejection. The exact nature of the instability which drives a flux rope CME is unknown. The transition from stable to an impulsive disruption depends on the parameters of the flux ropes (total electric current, twist) as well as the properties of the ambient medium and coronal magnetic fields. Possible causes of flux rope CMEs have been proposed and include the loss of flux rope equilibrium [Forbes 1991] and the initiation of the ideal kink instability [Török 2004].

Whatever the cause, if the instability occurs and a flux rope breaks off from the sun, the strength of the magnetic field from the flux rope can generate storms in space. These fields are an important source of large, sporadic, geomagnetic storms that affect the near-earth environment [Gosling 1997, Webb 1995]. They are responsible for disruptions in satellite functionality and can cause communication blackouts. Similar reconnection events in the earth's magnetosphere generate aural substorms that can have the same effect [Potemra 1988]. In the magnetosphere, a reconnection event between multiple flux ropes triggers short-lived jets of energetic particles that penetrate deep into the magnetic poles of the Earth [Elphic 1979].

1.3 – EXPERIMENTAL FLUX ROPES

A number of experiments have been designed explicitly to study the properties and dynamics of magnetic flux ropes. For instance, [Bostick 1956] was the first to simulate an arched, solar, magnetic flux rope by driving an electric current along an arched magnetic field. In later years, this technique was perfected to produce both single and multiple prominence-like structures of various configurations [Bellan 1998, Hansen 2004, Tripathi 2007]. If the twist of two adjacent magnetic loops was co-helical (or in the same direction), then configuration would trigger a disruption of the structure. If the twist of two adjacent magnetic loops was counter-helical (or in the opposite direction), then the two would merged to produce a highly energetic current sheet. Experiments at UCLA showed a similar disruption of an arched magnetic flux rope [Tripathi 2013]. However, in these instances, the impulsive disruption was driven by strong ion flow along the field.

Instead of generating arched magnetic flux ropes in the laboratory, one can study the simpler configuration of a linear flux ropes. As long as the dimensions of flux rope are the long and thin, this experimental system is a valid approximation of a solar filament. A number of linear magnetic flux rope experiments have been performed on the Large Plasma Device (LAPD) at UCLA. The first instance of these experiments was performed in 1991, investigating the interaction between two current channels in a high beta plasma [Pfister 1991]. Initially parallel, the flux ropes relaxed into a Taylor state [Taylor 1974] (where $\mathbf{J}\times\mathbf{B} = 0$). In later experiments, a third flux rope was added and the morphology of the three structures was studied as they merged [Van Compernolle 2012]. Other experiments investigated three-dimensional reconnection initiated by the collision of multiple flux ropes [Gekelman 2016], the first confirmation of a quasi-separatrix layer (QSL) in the system [Lawrence 2009], and the investigation of chaotic behavior embedded in the system [Gekelman 2014].

Similar to the LAPD, the Reconnection Scaling Experiment (RSX) at the Los Alamos National Laboratory was constructed to study magnetic reconnection physics as well as flux ropes dynamics [Sun 2010]. The device (4 m length × 0.2 m radius) uses a pair of plasma guns to create two current-carrying plasma columns. The two columns were shown to twist like a corkscrew and coalesce during collisional reconnection. In addition to the spatial structure, the flux ropes were shown to rotated in time. This rotation was attributed to the kink instability.

1.4 – KINK-DRIVEN DYNAMICS

This experimental work considers the global dynamics associated with a kink-unstable flux rope. The kink instability is an MHD instability which causes a current-carrying, tube-like, plasma column to tilt and deform– or kink [Shafranov 1956, Kruskal

1958]. The instability is triggered by a rise in plasma current above the Kruskal-Shafranov limit (I_{KS}). Above this threshold the $\mathbf{J}\times\mathbf{B}$ forces overcome the tension in the field lines. Quantitatively, I_{KS} is expressed as

$$I_{KS} = \frac{\pi a^2 B_z c}{L} \tag{1.1}$$

Here, B_z is the magnitude of the external magnetic field in which the current is embedded, a is the radius of the flux rope, L is its length, and c is the speed of light.

Magnetic flux ropes generated in linear devices – such as the system explored in this work – are subject to the kink instability. Once the instability is triggered, the flux rope is displaced from its equilibrium position until the instability saturates. Upon saturation, the dynamics of the magnetic flux rope settle into a rotating, helical equilibrium [Paz-Soldan 2011]. The rotating, helical equilibrium is characterized by long-lived, coherent fluctuation in the magnetic signals that dominate the entire experimental volume.

The first observance of the phenomena occurred during an investigation of magneto-plasma-dynamic thrusters [Zuin 2004]. To improve efficiency, an external magnetic field was applied to the thruster. However, this made the current discharge in the device susceptible to the external kink instability. Above the Kruskal-Shrafanov limit, a coherent $m = 1$ oscillation was observed. The mode grew for a few microseconds; then, the oscillations plateaued. The frequency of the mode was shown to scale with current, and the propagation of the mode was attributed to $\mathbf{E}\times\mathbf{B}$ rotation.

In 2006, the same phenomenon was seen in an experiment preformed at the University of Wisconsin in the Rotating Wall Machine (RWM) [Bergerson 2006]. In this experiment, a line-tied screw pinch, or flux rope (6 cm radius × 1 m length), was generated between a cathode and anode. After the kink instability was initiated, a rotating, stationary state formed. The mode was observed globally but was largest near to the anode. The magnitude of the oscillations was attributed to imperfect line-tying, due to a finite sheath resistance – close to the anode – that allowed the flux rope to displace from its axis by 1 cm. While the frequency of the mode scaled linearly with current, the overall scaling was simply called "complex;" and the authors acknowledged that the process was unexplored analytically and computationally. Despite the ambiguity, the rotating helical equilibrium was explained as the manifestation of volume-averaged $\mathbf{E}\times\mathbf{B}$ rotation, caused by the biasing of the plasma source.

[Intrator 2007] disagreed. Generating a single flux rope in the Reconnect Scaling Experiment, the work demonstrated that the kink instability could be initiated at thresholds lower than I_{KS} (depending on the experimental boundary conditions, plasma resistance, and axial flow). A rotating, stationary state formed and scaled with current, but the estimates of $\mathbf{E}\times\mathbf{B}$ rotation produced frequencies inconsistent with the ones observed. Instead, the rotation was attributed to axial flow, which – in the context of kink theory – transformed the purely growing mode into one with real frequencies [Ryutov 2006]. The same explanation was later used in experiments performed on the Magnetic Reconnection Experiment after a line-tied (but partially toroidal) flux rope exhibited rigid body rotation upon the kink instability [Oz 2011].

Despite the mode being seen in linear devices of similar size, with similar sources, and comparable flow profiles, there were discrepancies between the experiments. These discrepancies led [Paz-Soldan 2011] to deny that the phenomena seen in RWM was the same physics as the one seen in RSX. The most notable difference was the direction of rotation. While in RWM, the mode traveled in the $\mathbf{E}\times\mathbf{B}$ direction, the rotation observed in RSX traveled in the diamagnetic direction. Furthermore, the theory which was used to justify this external kink mode via axial flows predicts decreasing frequency with B_z. Increased scaling was observed in RWM. The differences were attributed to a weaker role of sheath resistance.

The experimental work performed for this dissertation was carried out on the LAPD. The flux ropes generated in the LAPD differ from the flux ropes mentioned above in that flux ropes in the LAPD are embedded in an ambient plasma rather than in a vacuum. However, all previous flux rope experiments on the LAPD have been subject the rotating, helical equilibrium. In fact, the pervasiveness and repeatability of the mode allows for the spatially reconstruction of the flux rope system. Typically, in a flux rope experiment, the experimental conditions are held constant while multiple probes take measurements at tens of thousands of locations inside the device. This results in a well-diagnosed experiment – volumetric measurements of plasma density, n_e; electron temperature, T_e; plasma potential, ϕ_p; magnetic field, **B**; current density, **J**; electric field, **E**, ion flow, $\mathbf{v}_{\text{flow}}$ – and places the LAPD in a unique position to solve some of the contradictions associated kink-driven dynamics. A discussion of the rotating, stationary state is the subject of Chapter 4.

1.5 – INCOHERENT BEHAVIOR

The flux ropes generated in the LAPD are an order of magnitude longer than the experiments discussed previously. They satisfy to a greater degree the long-thin approximation ($a/L \sim 10^{-3}$). As a result, the external kink mode manifests at lower currents; and, as the current in the flux rope increases to many times I_{KS}, the flux rope transitions away from its coherent state toward incoherent behavior. What is meant here by "incoherent" is that the magnetic oscillations produced in the experiment are disordered – neither repeatable nor predictable.

Finding an explanation for this behavior is difficult because the unpredictability of the signals prevents spatial reconstruction. While the physics behind the phenomena is more opaque, there may still be indicators of the physics: Experiments performed at the University of Wisconsin observed abrupt spikes in the magnetic signals even after the rotating helical equilibrium was initiated [Bergerson 2006]. These spikes were explained as internal reconnection events, which – much like a tokamak – relaxed the plasma and occurred despite no resonant magnetic surfaces. The occurrence of these spikes was observed in the spectrum at 10 kHz.

Similarly, recent work on the Line-tied Reconnection Experiment observed magnetic fluctuations that were intermittent, broadband, and chaotic [Brookhart 2015]. These observations were seen both in a hollow screw pinch system and a system of three merging flux ropes. The oscillations, however, where not connected to the kink instability, as the current in the flux ropes were below I_{KS}. Instead the oscillations were explained as turbulent fluctuations, which facilitated the reorganization of the structures into a simpler form.

The intermittent behavior observed in the LAPD manifests as a broad spectrum. The broad spectrum is produced by random pulses which occurs in the magnetic signals. Among the possible explanation, this dissertation will focus on one in particular (discussed in Chapter 5): this dissertation tests the hypothesis that the transition into incoherence is an indicator of a transition between a rotating helical equilibrium and a mode with an unstable, chaotic orbit.

1.6 – CANONICAL HELICITY

Helicity is a measure of the linkage, knottedness, and twist of a topological configuration [Moffat 1978, Pfister and Gekelman 1991, Berger 1999, Bellan 2000]. A fundamental quantity, the conservation of helicity has been used in the development of physical models – including models of tornadoes [Rasmussen 1998], DNA [Ernst 1999], and polymers [Lehn 1995]. In plasma physics, concepts of helicity have been the foundation for models of cosmic magnetic fields [Kulsrud 2008], astrophysical jets [Li 2006], and solar coronal loops [Mahanjan 2001] – among others. When helicity describes the linkage of a magnetic vector field, the quantity is called magnetic helicity. Magnetic helicity H_M is given by:

$$H_M = \int \boldsymbol{A} \cdot \boldsymbol{B} \, dV \qquad (1.2)$$

where $\boldsymbol{A}$ is the magnetic vector potential and $\boldsymbol{B}$ is the magnetic field ($\boldsymbol{B} = \boldsymbol{\nabla} \times \boldsymbol{A}$). Equivalently, H_M describes the amount of twist and kink of magnetic field lines [Blackman 2015].

Magnetic helicity is a useful tool in the analysis of astrophysical plasmas because in the magnetohydrodynamic limit it is a conserved quantity. The conservation of magnetic helicity was first proposed by [Taylor 1974]. Searching for the theoretical relaxation state of a toroidal plasma into a reversed-field pinch, Taylor minimized the magnetic energy under the constraint of a perfectly conducting fluid. He concluded that the system would relax in such a way as to preserve magnetic helicity within magnetic flux surfaces. He conjectured that it was resistive physics that allowed internal access to the relaxed state. As long as the departures from perfect conductivity were rapid compared to the resistive diffusion time, the breaking and coalescing of the field lines would still preserve the total magnetic helicity.

Twisted magnetic flux ropes have been thought to be the source of coronal helicity [Low 1994, Amari 1999]. As the flux ropes in the solar atmosphere reconnect, magnetic helicity is preserved during the process. This has been observed indirectly: as magnetic flux ropes break off from the sun during a CME, the resulting interplanetary magnetic cloud retains the helical chirality (sign of helicity) that it had in its coronal bound state [Rust 1994, Bothmer 1994]. Similarly, under an eruption of a helical prominence, the twist of the field has been shown to transfer from one part of the prominence to another [House 1987].

When the ideal fluid picture breaks down, magnetic helicity is not conserved. However, attempts have been made to generalize the principle within a two-fluid framework. These include generalized vorticity [Turner 1986], self-helicity [Steinhauer 1997], generalized helicity [Oliveira 1995], and fluid helicity [Avinash 1995]. An additional generalization of helicity is called canonical helicity [You 2012, You 2016]. Canonical helicity differs from the other concepts in that it was derived using a Lagrangian-Hamiltonian framework. It takes into account dissipation, collisionless situations, collective behavior, particle reactions, and electromagnetic interactions.

In Chapter 6, we present the first experimental measurements of global canonical helicity. Two interacting flux ropes are considered. The two flux ropes are driven kink unstable. They collide, merge, then break apart regularly. As the two collide, a small component of the magnetic field from each rope is anti-parallel, and magnetic reconnection is triggered. In this chapter, canonical helicity is observed and shown to be conserved during a reconnection event.

1.7 – DISSERTATION OBJECTIVE AND OUTLINE

The objective of this dissertation is to investigate the conservation of canonical helicity during a magnetic reconnection event, which occurs when two magnetic flux ropes collide. To initiate the reconnection event, the flux ropes are driven kink unstable. This causes the flux ropes to periodically crash into one another. To better understand this kink dynamic, the behavior of a single, kink-unstable flux rope is considered, first, before the two, flux-rope system is examined. The analysis is based on detailed, volumetric measurements of the magnetic field as well as measurements of temperature, density, plasma potential, and flows.

A review of astrophysical and experimental flux ropes was given. Chapter 2 contains a description of the experimental device, probes, and analysis techniques. In

Chapter 3, the structure of the flux ropes is discussed - including the scaling of internal, plasma parameters with external, experimental conditions. Turning toward the kink-driven dynamics of a single magnetic flux rope, Chapter 4 explores the rotating helical equilibrium. This mode is characterized by the orbital rotation of the flux rope about its equilibrium axis. The maximum displacement of the flux rope from equilibrium increases with discharge power. In Chapter 5, the intermittent behavior is examined and tested against measures of chaotic systems. Intermittent pulses in the temporal derivative of the magnetic field characterize this behavior and can be used to locate the position of the flux rope in space. As the current in the rope increases, the motion of the flux rope transitions to a chaotic orbit. Finally, in Chapter 6, canonical helicity is presented for a system of two magnetic flux ropes. In particular, changes in canonical helicity are examined for field lines in the process of reconnecting (identified by a quasi-separatrix layer). The dissipation of relative canonical helicity is balanced by the transport of relative canonical helicity inside the QSL through electrostatic fields generated during reconnection.

CHAPTER 2 – *EXPERIMENTAL METHOD*

2.1 – THE LARGE PLASMA DEVICE

A series of flux rope experiments were performed on the Large Plasma Device (LAPD) at UCLA's Basic Plasma Science Facility (BaPSF). A detailed discussion of the LAPD is given in [Gekelman *et al.* 2016]. However, a brief review of the device will be given here: The LAPD is a twenty-four-meter long, one-meter diameter, cylindrical vacuum vessel. A sketch of the device is found in Figure 2.1. Vacuum is established through four turbo-molecular pumps, which evacuate the chamber to a base pressure less than 5×10^{-7} Torr. Once base pressure is achieved, a single (or multiple) working gas (H_2, He, Ne, or Ar) is released into the system, regulated by mass flow controllers (MFCs). The rate of release of this gas is brought into equilibrium with the rate of its removal such that a fill pressure is established of approximately 3×10^{-5} Torr.

The vacuum vessel is surrounded by ten sets of solenoidal electromagnets, which are made from heavy gauged, extruded copper bars - water cooled so that they may be driven with large current (~kA). Each set of electromagnets is independently driven by a programmable power supply. The independent nature of each set allows for a flexible field profile along the axis of the device. For the series of experiments presented in this work, a simple, straight field (usually $B_z = 330$ G) is formed. The orientation of the

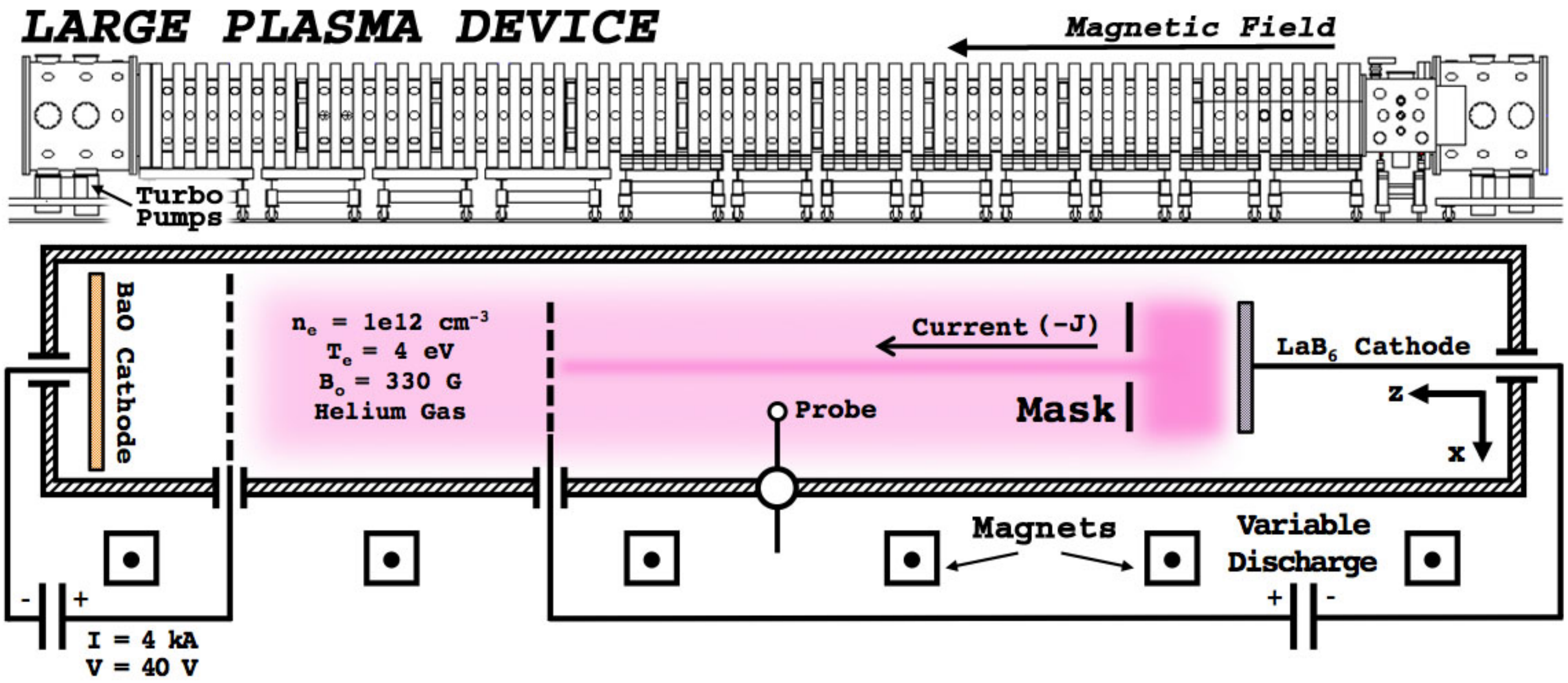

Figure 2.1 – A schematic of the Large Plasma Device (LAPD). Four turbo pumps evacuate the chamber to a base pressure of $<10^{-6}$ Torr. A single working gas of He is introduced into the system at 3×10^{-5} Torr, which is then ionized using a cathode-anode discharge. This BaO cathode is shown to the left. The discharge creates a ambient plasma medium 20 m in length and 60 cm in diameter. A secondary cathode-anode pair is placed on the far end of the device (to the right). A mask is placed between the LaB$_6$ source and its anode (located several meters away) such that electrons are only emitted from what hole is cut into the mask. This can be used to create one or more flux ropes. The flux ropes are typically 11 m long and 5 cm in diameter.

magnetic field points in the $+\hat{\mathbf{z}}$ direction.

At one end of the device is positioned a cathode-anode pair that is electrically isolated from the chamber walls. The cathode is a 60 cm, nickel plate, coated with a thin layer of barium oxide (BaO) [Leneman 2006]. The cathode is indirectly heated to 800 °C by an array of resistive tungsten filaments. At this temperature, the cathode becomes a thermionic emitter. The corresponding anode is a semi-transparent (50%), molybdenum wire mesh, located 50 cm in front of the cathode. When the anode is pulsed between 30 to 50 V with respect to cathode, electrons pass between the two [Pribyl 2004]. The 4 kA direct-current discharge lasts for 12 ms (starting from the current threshold of 1 kA). A typical discharge from the BaO cathode is plotted in Figure 2.2.

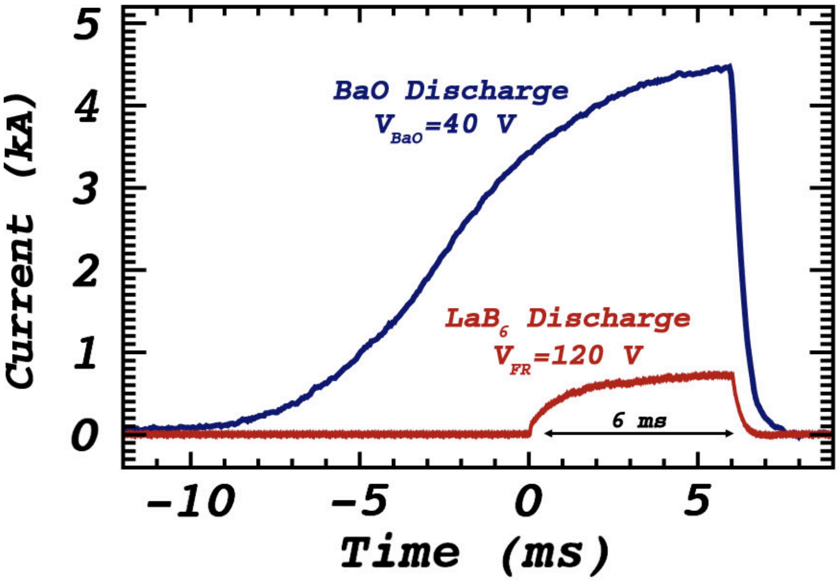

Figure 2.2 – Current discharges associated with the two cathode-anode sources. The BaO source is pulsed with 40 V, producing a current discharge that peaks at approximately 4 kA. The LaB$_6$ trace is the discharge for two flux ropes ($a = 3.5$ cm, $L = 1100$ cm each), which peaks at 750 A. The LaB$_6$ cathode is triggered at $t = 0$ ms and operates for 6 ms during the BaO discharge.

If an electron from the discharge collides with a neutral gas particle, there is a finite probability that the collision results in an ionized neutral and free electron. When numerous electron-neutral collisions occur during the discharge, a plasma is generated. Because the anode is semi-transparent, any plasma production between the cathode-anode pair can pass through anode into the main chamber, forming a current-neutral, quiescent, plasma column ($\delta n/n \approx 3\%$, $0.05\ \mathrm{eV} \leq T_e \leq 5\ \mathrm{eV}$, $10^{10}\ \mathrm{cm}^{-3} \leq n \leq 2\times10^{12}\ \mathrm{cm}^{-3}$, $T_i < 1\ \mathrm{eV}$) 20 m long and 60 cm wide. The flux rope is embedded into this ambient medium. An illustration of the device and the various elements are presented in Figure 2.1.

2.2 – FLUX ROPE GENERATION

An additional plasma source is used to generate the flux rope. This lanthanum hexaboride (LaB_6) source is inserted radially into the LAPD at an axial position opposite to but facing the main source. There are two separate flux rope sources used in the series of experiments presented here. The sources are qualitatively the same, except for their size. The first source (Figure 2.3a) is a small, circular cathode (d = 10 cm) [Van Compernolle 2011]. A portion of the LaB_6 material is masked with a carbon plate, such that the cathode only emits from a circular hole. The second source (Figure 2.3b) is a larger 20 cm x 20 cm cathode [Cooper 2010]. This larger source is not directly masked. Instead, a floating carbon mask is place 64 cm in front of the cathode.

At sufficient temperatures ($T \sim 1800\ ^{o}C$), the LaB_6 material becomes a thermionic emitter– up to 10 $A\text{-}cm^{-2}$ [Goebel 1985]. In order to reach those temperatures, an s-shaped carbon flat, heated through resistive dissipations of circulated

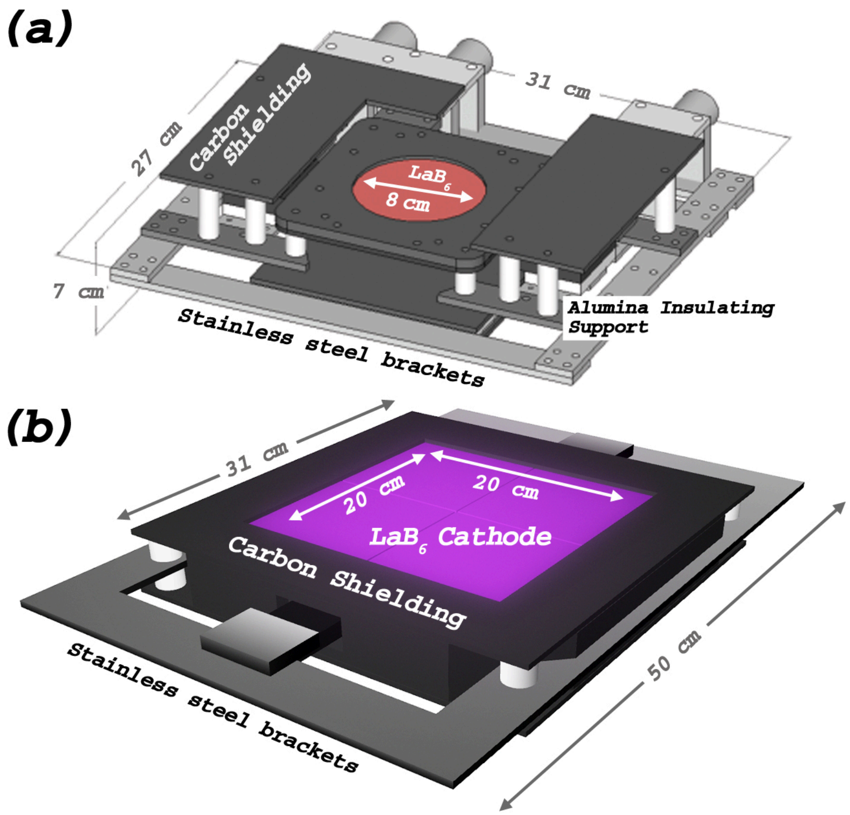

Figure 2.3 – A comparison between the two flux rope sources used in the series of experiments presented here. **(a)** A smaller LaB$_6$ cathode that is directly masked to produce a flux rope that is 5 cm in diameter. The mask is not shown in the figure. **(b)** A larger LaB$_6$ that is not directly masked. Instead a mask is placed 64 cm away from the cathode. Multiple flux rope configurations have been designed using this cathode.

current, is placed close to (but electrically isolated from) the LaB$_6$ crystal. Once heated, the source will emit electrons when biased positively with respect to an anode. A typical discharge for the larger LaB$_6$ cathode is plotted in Figure 2.2.

The anode is a square (30 cm x 30 cm), molybdenum wire mesh which is radially inserted into the LAPD. The distance between the mask and this anode determines the length of the flux rope. With an independent capacitor bank and transistor switch, a voltage is applied between the LaB_6 cathode and its anode. This generates a current channel, or flux rope, aligned with the axis of the LAPD for 6 ms. The current channel is fixed at the mask (defined to be $z = 0$ cm) but free to move about the anode (typically placed at $z = 11$ m).

The voltage between the cathode and its anode is set by the charge on the capacitor bank. On the other hand, the corresponding discharge current depends on the discharge voltage, the gas pressure, the magnetic field, and the state of the cathode. In order to have greater control over this current (the current in the flux rope), the temperature of the LaB_6 was fine-tuned until its emissivity resulted in the desired current.

	Electron	***Ion (He$^+$)***
Spatial	$10 < \lambda_D < 30\ \mu m$	
	$20 < \rho_e < 500\ \mu m$	$1 < \rho_i < 30$ mm
	$1 < \omega_e/c < 5$ mm	$10 < \omega_i/c < 150$ cm
Temporal	$0.5 < f_{ce} < 5$ GHz	$10 < f_{ci} < 750$ kHz
	$0.5 < \upsilon_e < 10$ MHz	$0.05 < \upsilon_i < 2$ MHz
	$5 < f_{pe} < 30$ GHz	$30 < f_{pi} < 300$ MHz

Table 2.1 – A review of the temporal-spatial scale lengths for the experiment.

The flux ropes that are produced are on the order of the size of the machine. The cross-sectional ($d_{FR} = 5 - 7$ cm) and axial lengths ($L_{FR} = 11$ m) of the flux rope are on order of, or greater than, the relevant lengths of the ion and electron gyroradii (ρ_e), the ion and election inertial length (ω_i/c and ω_e/c respectively), and the Debye length (λ_D).

The time scales of experiments performed on the LAPD are on the order of tens of milliseconds. This is greater than the periods associated with the ion and electron gyrofrequency (f_{ci} and f_{ce} respectively), the ion and electron plasma frequency (f_{pi} and f_{pe} respectively), and the ion and electron collision frequency (υ_i and υ_e respectively). A table of these quantities is presented in Table 2.1.

2.3 – DIAGNOSTICS

Over four hundred diagnostic ports (located approximately every thirty-two centimeters axially and every forty-five degrees poloidally) line the walls of the vacuum vessel. The LAPD operates continuously, generating a pulsed plasma every second. In such a way, experiments are repeated over a million times in the course of a few week period. The combination of numerous diagnostic ports and reliable repetition results in a well-diagnosed plasma, accumulated volumetric datasets of *in situ* measurements.

The majority of measures were taken by small probes (< 1 cm) – small enough such that they do not disturb the flux rope. These probes protrude from the end of a long, aluminum shaft and are inserted radially into the LAPD through one of its many ports. The shafts are free to slide in and out of the machine without breaking vacuum. Fifty diagnostic ports on the LAPD are fitted with vacuum ball-joints, which allow the probes to move anywhere within a cone of 35 degrees [Leneman 2001]. An automated computer-controlled probe drive system utilizes these ball-joints to move the probes in either the **x-z** plane or the **x-y** plane. The automated probe drive system moves the probes to user-specified positions, collecting data from these location between successive plasma discharges. During these discharges, probe signals are connected to an analog-to-digital converter that stores the information for later analysis. After multiple **x-y** data planes are collected, the planes are combined to create volumetric datasets of density, temperature, plasma potential, magnetic field, and flows. The following is a discussion into the types of probes that were used in these experiments.

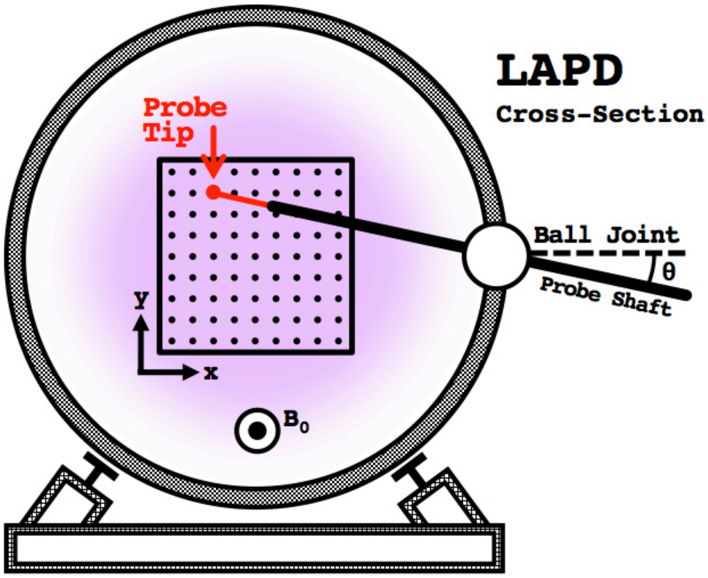

Figure 2.4 – A cross-sectional sketch of the LAPD. The figure demonstrates the probe motion and data acquisition method in the device. An automated probe drive changes the angle θ and insertion distance into the LAPD vacuum chamber. The probe shaft slides on a double O-ring seal to prevent breaking vacuum. The probe moves in a grid between successive discharges to assemble volumetric dataset point for point.

2.3.1 – Langmuir Probes

A staple of plasma measurement, Langmuir probes were used to estimate the temperature and density of the plasma. Constructed from a small, metallic collector, the probe is variably biased (a “sweep”). As a result, free-floating charges in the plasma are either attracted to or repelled from the tip of the probe. Any charges collected by the probe are then measured as current. When the current is measured over a range of biases, a characteristic I-V curve [Chen 1954, Hershkowizt 1989] is constructed from which the temperature and density can be estimated.

To verify that the estimates of plasma density are close to the experimental values, the results from the Langmuir Probe are compared with data taken from several interferometers. These interferometers are located every few meters axially along the LAPD. While the results from the interferometers cannot be interpreted under the experimental conditions of a moving flux rope, a comparison between the background plasma and the Langmuir and the interferometer yields values within 10%.

For the experiments presented in this work, the probe was “swept” two different ways. First, the Langmuir probe was fixed in space; a constant voltage was applied to the probe over the course of a discharge, and the current collected by the probe was recorded as a function of time. The voltage applied to the probe was slowly stepped up each time the experiment was preformed. This allows for a time resolved temperature measurements at a fixed point.

The second method applied a voltage ramp (slowly increasing in time) to the probe a few times during an experiment. The current was collected and recorded over each sweep. Therefore, each time the experiment was performed, a few temperature measurements were taken from a fixed location. By moving the probe each time the experiment is performed, the temperature was measured with good spatial resolution but at the expense of temporal resolution.

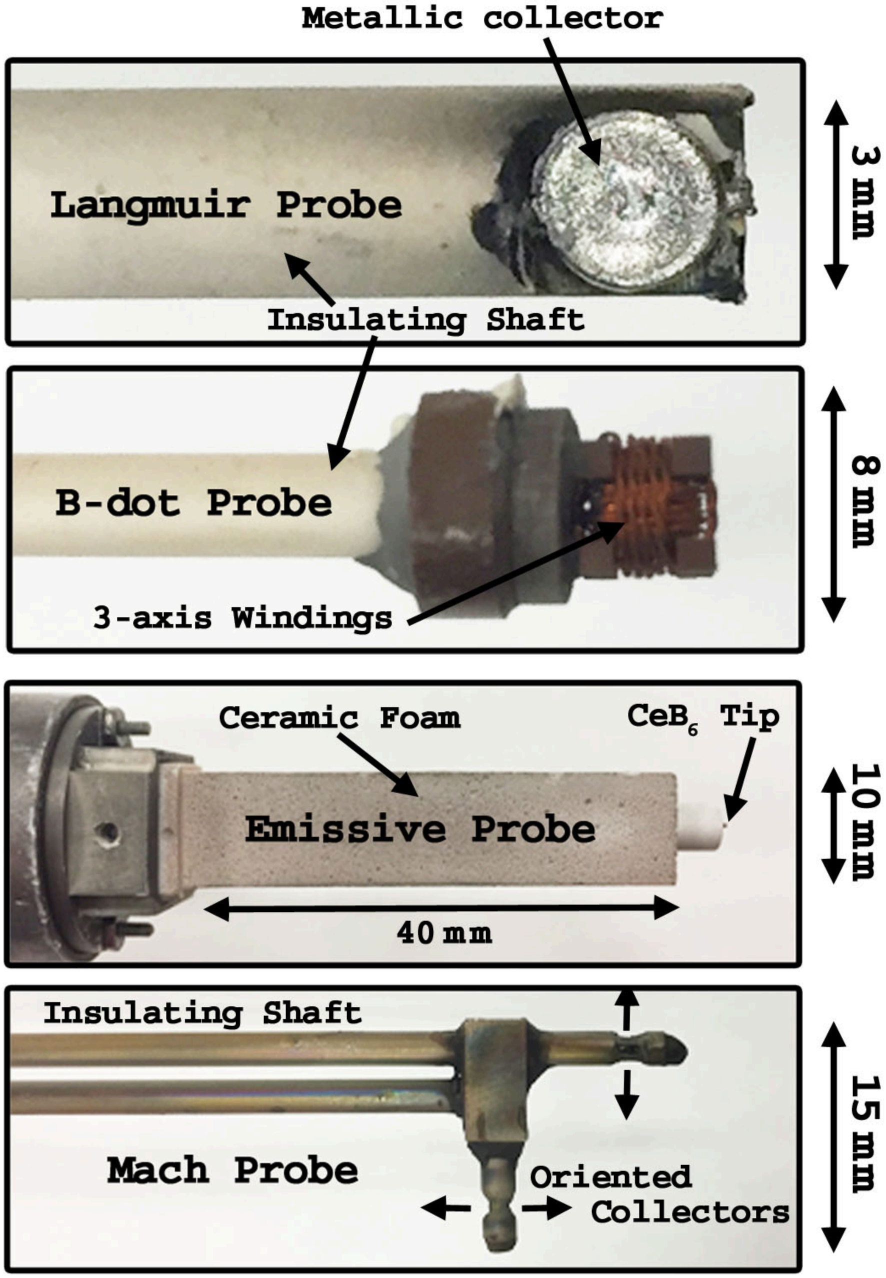

Figure 2.5 – A collection of the probe diagnostics used in the Large Plasma Device: The Langmuir probe, a small metallic collector variably biased to collect or repel free-floating charged particles. A magnetic pickup loop used to measure the magnetic field by Faraday's law. An Emissive probe, which floats at the plasma potential when the tip is sufficiently emissive. A Mach Probe, a set of particularly oriented collectors to infer ion flow in the plasma.

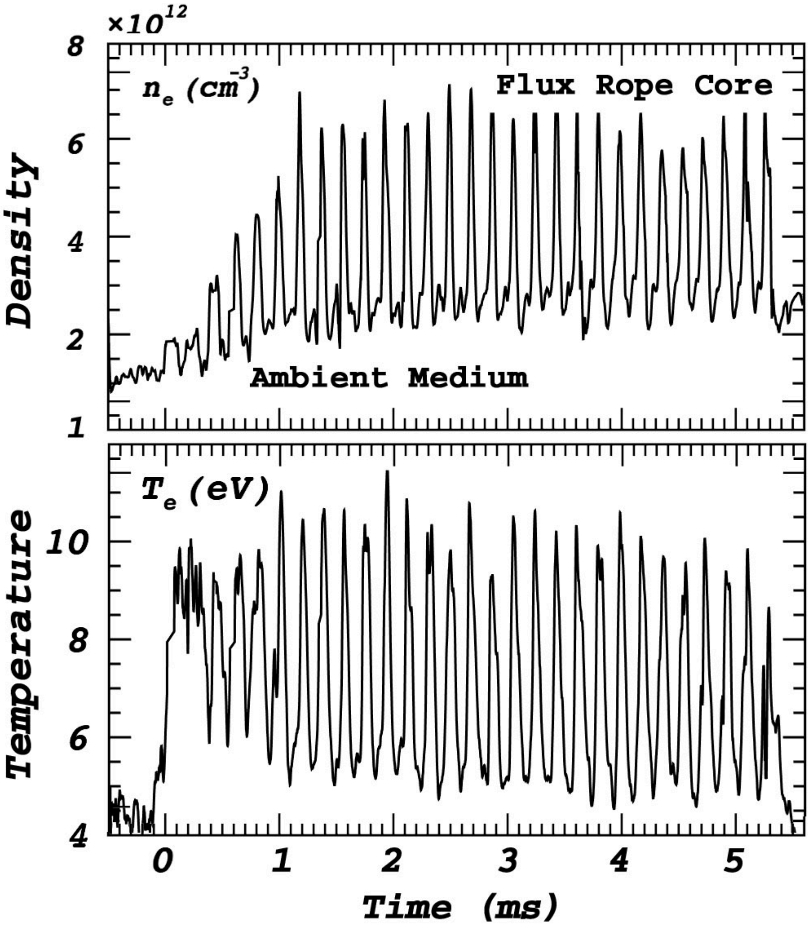

Figure 2.6 – **(a)** Time resolved measurement of plasma density at (x,y,z = 5, 0, 160 cm). As the kink unstable flux rope passes this location, a spike in the density is observed. From such time traces, the density of the core of the flux rope and the ambient medium can be inferred. **(b)** Time resolved measurement of plasma temperature at (x,y,z = 5, 0, 160 cm). As the kink unstable flux rope passes this location, a spike in the temperature is observed. From such time traces, the density of the core of the flux rope and the ambient medium can be inferred.

Using the former method, the temporally resolved temperature and density was calculated at particular point in space (x,y,z = 5, 0, 160 cm). The results are plotted in Figure 2.6. Large-scale oscillations ($\frac{\delta n_e}{n_e}, \frac{\delta T_e}{T_e} \sim 0.5$) are observed in the time trace. These oscillations are the result of the motion of a kink unstable flux rope. The probe samples a distribution of temperature and density as the kink-unstable flux rope passes by the probe. If the flux rope is treated as a rigid object, exhibiting orbital motion about some equilibrium, then minimums in the figure indicate characteristics of the background medium (or close to it) while peaks in the figure indicate the plasma parameters of the flux rope core. In Chapter 3, these measurements of temperature and density are used to explore scaling of these quantities with discharge power.

2.3.2 – Magnetic Probes

Temporal changes in the magnetic field ($\dot{\mathbf{B}}$) were measured by magnetic pickup loops. Typically, these magnetic diagnostics consists of six magnetic pickup loops, a three-axis configuration, two loops oppositely wound per orthogonal dimension [Everson 2009]. Each loop of wire is wrapped around a face of a cube so that the surface area each loop is similar ($A \sim 9$ mm^2) and encased in a ceramic dome. If changing magnetic flux traverses normal to the surface of these coils, a potential difference is measured across each loop according to Faraday's law: $V_{Induced} = -A_{Eff}\dot{\mathbf{B}}$. If two differentially wound coils are aligned along the same dimension, their voltages are subtracted to suppress electrical noise; and from the resulting potential, the magnetic field is inferred accordingly. The error in these probe measurements are nominal. When the magnetic field is measured as a function of space, other important electrical parameters can be derived. In particular, the vector potential (**A**) can be estimated as well as the current density (**J**) through Ampere's law.

2.3.3 – Emissive Probes

An emissive probe was used to measure the plasma potential V_p. An emissive probe in substance is a hot, emitting surface placed in contact with the plasma. The probe was first suggested by Irving Langmuir in 1923 [Langmuir 1923] and operates in the following manner: If a cold, metallic collector is in contact with a plasma, then the potential difference between the plasma (V_p) and the potential at which the probe "floats" (V_f) is governed by:

$$V_f - V_p = \frac{kT_e}{e} \ln\left(\frac{I_{isat}}{I_{esat}}\right) \tag{2.1}$$

where I_{isat} is the ion saturation current and I_{esat} is the electron saturation current collected by the probe. However, when the conducting surface become emissive, the probe floats closer to the plasma potential by the addition of another term:

$$V_f - V_p = \frac{kT_e}{e} \ln\left(\frac{I_{isat} + I_{emit}}{I_{esat}}\right) \tag{2.2}$$

As $I_{isat} + I_{emit}$ approaches I_{esat}, the logarithm approaches zero; and therefore, the probe will be at the plasma potential [Kemp 1966]. This is highly advantageous as – in contrast to a swept Langmuir probe – good temporal and spatial resolution of the plasma potential can simultaneously be measured; and with volumetric measurements, the electric field can be estimated.

A special emissive probe was developed at the Basic Plasma Science Facility (BaPSF) [Martin 2015]. It is constructed with a cerium hexaboride (CeB_6) tip, resistively heated by current passed through a carbon load. The CeB_6 emits electrons from its surface up to 10 A-cm^{-2}. To ensure that the probe is hot enough, I_{emit} is measured by variably biasing the probe in the same manner as described in Section 2.3.1 on Langmuir probes. As a ‘sweep’ is performed, the current collected from the probe is measured. When the probe is biased well below the plasma potential, the probe will emit electrons, measured as “collected” ions. When the absolute value of this current reaches I_{esat}, the probe is considered emissive enough to float at the plasma potential.

The emission from the probe is space-charge limited. A correction is needed, which is added to Eq. 2.2, in order to estimate the plasma potential:

$$V_f - V_p + \alpha T_e = \frac{kT_e}{e}\ln\left(\frac{I_{isat} + I_{emit}}{I_{esat}}\right) \tag{2.3}$$

where α is approximately unity. The value α was derived analytically using fluid theory and estimated to be 1.02 for a helium plasma [Hobbs 1967]. Similarly, [Ye 2000] estimated the value to be 0.99, while [Schwager 1993] developed a kinetic PIC model to confirm unity as well. Using the temperature measurements from the Langmuir probe, this correction was imposed for all measurements taken with the emissive probe. In the core of the flux ropes, the error in the measurement are approximately $\delta V_p/V_p \sim 0.1$.

2.3.4 – *Mach Probe*s

Mach probes are metallic collectors, variably biased to collect free-floating, charged particles. Mach probes differ from the typical Langmuir probe in that they are constructed from a series of particularly oriented collectors: each surfaces faces the plasma in a different direction. The faces of the probe are biased negatively with respect to the plasma potential, collecting only ions. Each face will collect a varying amount of ions. Ions flowing toward a face of the probe will collect more current than faces oppositely directed. Therefore, the flow may be inferred by examining the differences in current collected by each face.

Theoretical models have been developed to provide the relationship between the ion flow and two oppositely directed collectors. These models are typically separated into the magnetized [Stangeby 1984, Hutchinson 1988] and unmagnetized regimes [Huddis 1970, Hutchinson 2003, Oksuz 2004]. When the ion larmor radius ρ_i is much greater than the probe dimension d (i.e. $\rho_i \gg d$), the ions are treated as unmagnetized while the opposite is treated as magnetized. In either case, Mach probe models take the form

$$\frac{I_{isat+}}{I_{isat-}} = e^{KM} \tag{2.4}$$

In Eq. 2.4, I_{isat+}/I_{isat-} is the ratio of ion saturation current collected from surfaces facing upstream (+) and downstream (-); M is referred to as the Mach number, the mean ion flow expressed as a fraction of the sound speed ($M = \langle \mathrm{v} \rangle / c_s$); and K a model-dependent constant when $M < 1$.

The Mach probe used in the experiment was constructed from a series of six tantalum collectors (Figure 2.5). The faces of each were oriented orthogonally (two per dimension); and, to accommodate flows in the $\hat{\mathbf{x}}$-direction, an "elbow" was constructed so that a portion of the probe extrudes at a right angle. Each face of the probe has an area of < 1 mm^2. Assuming $T_i \sim 0.1$ eV and $B_0 \sim 330$ G, then the ion gyroradius ρ_i of a helium ion is 2 mm. This is on the order of the size of the probe; and therefore, Mach probe analysis will be considered using the unmagnetized regime.

[Hudis 1970] developed a one-dimensional, free-fall model for a collisionless, fluid-like plasma with the criteria that $\rho_i > d \gg \lambda_D$ and $T_e > T_i$ where λ_D is the Debye length. Under this model, K was estimated to be

$$K = \frac{2\sqrt{2(T_e T_i + T_i^2)}}{T_e} \tag{2.5}$$

For the LAPD background plasma, $K \sim 0.5$. This is the constant used in the reconstruction of Mach flow associated with the flux rope.

Mach probes suffer from differences in collection area between tips. This can remedied to an extent by calibration: first taking measurements with the probe oriented in one direction, then repeating the measurements with the probe rotated $180°$. A calibration factor is then calculated from the ratio of the measured saturated current of each tip in normal and flipped configurations.

2.4 – THREE-DIMENSIONAL RECONSTRUCTION

Spatial reconstruction of the flux rope requires repeatability of any measured signal. In order to test repeatability and reconstruct the three-dimensional system, a fixed, magnetic probe is employed. Upon the initiation of the kink instability, the flux rope enters into a rotating helical equilibrium [Paz-Soldan 2011]. The magnetic signals associated with this type of behavior are global, repeatable, and highly coherent – even for a system of multiple flux ropes [Gekelman, 2012]. The signals observed by the fixed probe are characterized by this mode.

The frequency of the mode, however, is not phase locked. For example, Figure

2.7a plots ten successive magnetic signals from a fixed probe. Each time trace is triggered at the same moment, the initiation of the LaB_6 source. While a pattern is identifiable for each individual time trace, the average to these ten time traces will exhibit small oscillation with large error. In order to correct for the phase difference between successive discharges, each shot is triggered independently. This is known as conditional triggering [Van Compernolle 2012].

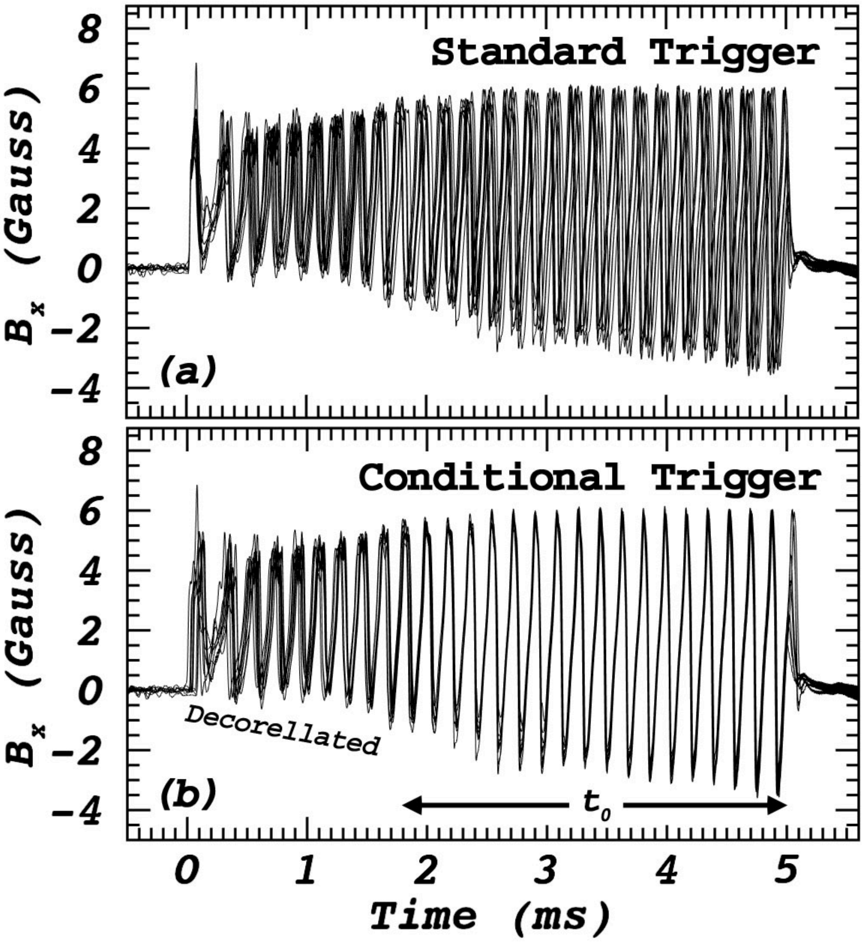

Figure 2.7 – Ten consecutive time traces of magnetic signals from the fixed probe. **(a)** is the representation of the un-aligned signals using a standard trigger. **(b)** is the representation of aligned signals using conditional triggering. The conditional trigger is valid for a certain length of time before the signal becomes decorellated.

The effective length of time over which reconstruction is possible is approximated by an autocorrelation of a single time trace from the fixed probe. The envelope of the autocorrelation takes the functional form $\left(1 + (t'/t_0)^{3/2}\right)^{-1}$. This form is consistent throughout the varying external conditions imposed on the experiment. The width t_0 is determined and taken to be the amount of time for which spatial reconstruction is possible. Outside this time range, the signals become decorrelated.

The fixed probe collects data from the same location over the course of several weeks. A temporal range of t_0 is isolated from the end of each time trace collected from the fixed probe. Spatial reconstruction is done for this period of time (where the discharge current has reached a steady state). A random time trace from the fixed probe is selected from and made “master reference.” A cross-correlation is performed between the “master reference” and all other data collected from the fixed probe. In this way, the phase difference between the two is revealed. The cross-correlation between the “master reference” $\mathbf{B}_{MR}(t)$ and any other magnetic time trace from the fixed probe $\mathbf{B}_i(t)$ can be written as

$$C(t') = \frac{\int_{t_{end}-t_0}^{t_{end}} \mathbf{B}_{\boldsymbol{MR}}(t)\, \mathbf{B}_{\boldsymbol{i}}(t-t')dt}{\int_{t_{end}-t_0}^{t_{end}} \mathbf{B}_{\boldsymbol{MR}}(t)^2 dt\, \int_{t_{end}-t_0}^{t_{end}} \mathbf{B}_{\boldsymbol{i}}(\mathrm{t})^2 dt} \tag{2.10}$$

where t_{end} is the time at the end of the experiment and t_0 is the width of time over which reconstruction is possible. Maximum correlation $C(t')|_{max}$ yields the temporal shift t'_{max} between discharges. When shifting $\mathbf{B}_i(t)$ such that $\mathbf{B}_i(t) \rightarrow \mathbf{B}_i(t - t'_{max})$, the signal demonstrates good alignment with the “master reference.” Figure 2.6b shifts the time traces in Figure 2.7a to demonstrate the effectiveness of the technique.

The shift t'_{max} is applied to all other data collected during a single discharge of the BaO and LaB_6 sources, regardless of the position of any other probe. This can be done because the correlation length between two probes in a LAPD flux rope experiments is greater than 5 meters. Several probe diagnostics (mentioned in Section 2.3) were used to generate fully three-dimensional datasets of relevant quantities: a Mach probe measured the ion flow; magnetic pickup loops measured the magnetic field; an emissive probe measured the plasma potential; and a Langmuir probe measured the temperature and density of the plasma. Each probe was moved to forty-three thousand locations within the plasma; and at each location, repeatable time traces were recorded. When the conditional trigger is applied to each time trace, the data can be reconstructed three-dimensionally point-for-point. The characteristics of these quantities are the subject of the next chapter.

CHAPTER 3 – *STRUCTURE OF THE MAGNETIC FLUX ROPE*

3.1 – INTRODUCTORY REMARKS

When generating magnetic flux ropes in the LAPD, there are typically three parameters that can be varied. They are the external, background magnetic field; the gas to be ionized (along with the gas pressure); and the input power associated with the plasma sources: two cathode-anode pairs, which generate the background plasma and the flux rope. The characteristics of the flux ropes (and therefore their dynamics) are changed by manipulating a combination of these three quantities.

The key flux rope quantities were measured: the magnetic field (**B**), temperature (T_e), density (n_e), plasma potential (ϕ_p), and ion flow (**v**). These quantities develop in space, both in the perpendicular direction and the parallel direction. The characteristics of each measured quantity are considered in turn. These quantities will lay the basis for the discussion of kink-driven dynamic in Chapter 4 and canonical helicity in Chapter 6. In this chapter, measurements are presented for both a single flux rope and multiple flux rope system. The single flux rope system will be used to understand the scaling of key quantities at fixed locations. The two flux rope system will be used to understand the spatial structure of the flux ropes.

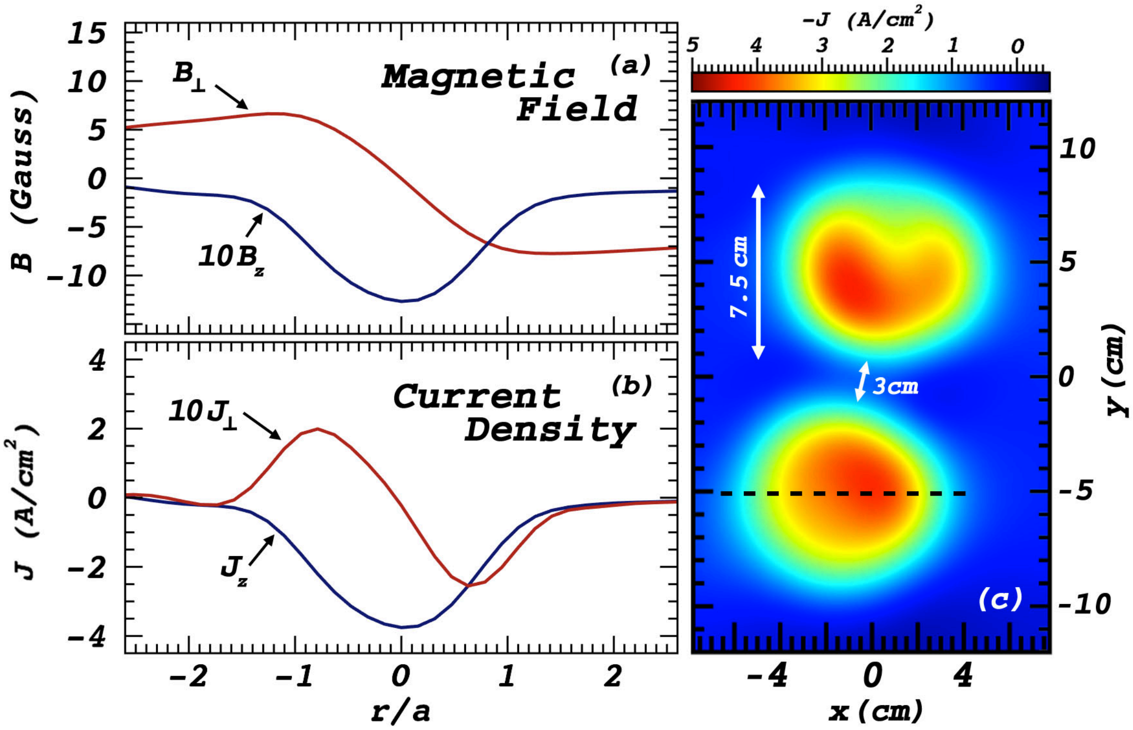

Figure 3.1 – The **(a)** magnetic field and **(b)** current density profile for a flux rope (a = 3.75 cm, L=1100 cm, B_z = 330 G, I_{FR} = 300 A) at z = 64 cm and t = 4.75 ms. **(c)** A x-y cross section of the two flux rope current densities at z = 64 cm. The dashed line indicates the lineout used in (a) and (b).

3.2 – MAGNETIC FIELD AND CURRENT DENSITY

The first thing to consider is the rope magnetic field and its associated current. In Chapter 1, Figure 1.1 demonstrated the three-dimensional nature of the magnetic fields. It showed a flux rope that is long and thin ($a/L \sim 10^{-3}$) – a twisted bundle of magnetic field lines. In Figure 3.1, a 2D cross-section of the current density is shown for the two flux rope system (a = 3.75 cm, L=1100 cm, B_z = 330 G, V_D = 120 V, I_{FR} = 300 A each) that will be used to evaluate canonical helicity. The flux ropes are 7.5 cm in diameter, and their inner edges are separated by 3 cm. A lineout across one of the flux ropes is presented in Figure 3.1a and Figure 3.1b – the magnetic probe inserted into the LAPD from the **+x** direction. The sign of the axial current suggests that the current points towards the LaB_6 source. The superposition of the background magnetic field ($B_0 = 330\ G$ and not plotted in the figure) and the poloidal field from this current results in a structure that is left-handed.

The perpendicular current points in the same direction as the perpendicular magnetic field. The direction of the current is responsible for a reduction of the background magnetic field in the core of the flux rope (~1 G). The reduction can be estimated by imagining the spiraling currents as a solenoid of length L and current I – wound around the axis a number of times proportional to J_θ/J_z.

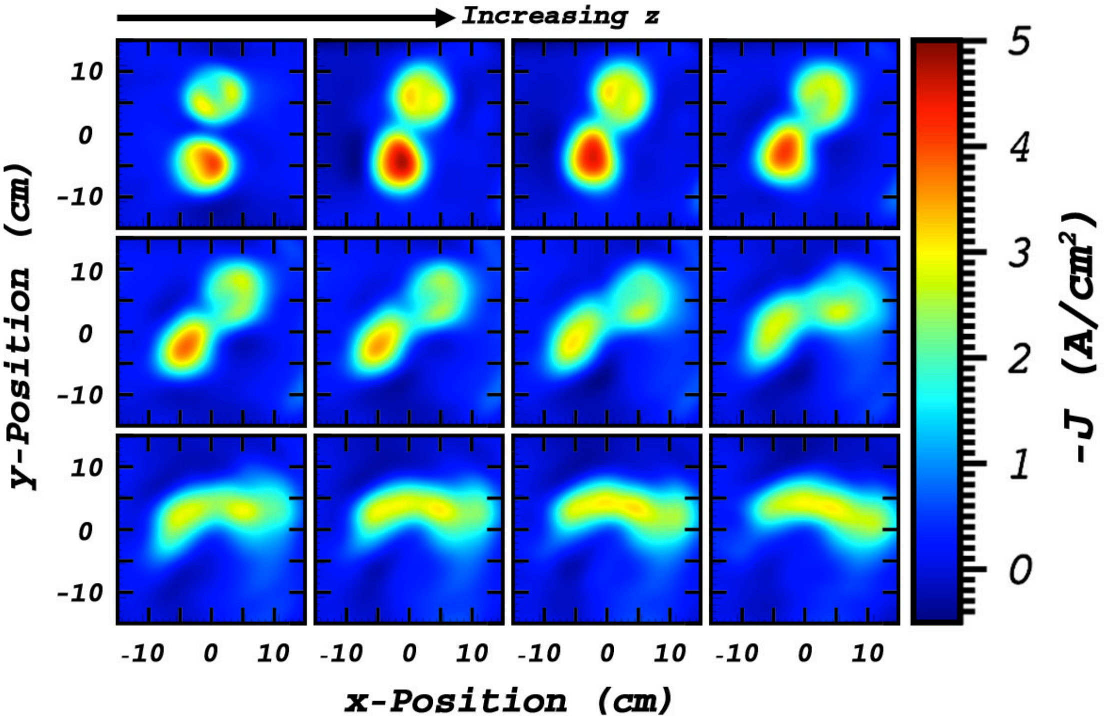

Figure 3.2 – Parallel current density (J_z) at various axial location (z_{start} = 64 cm, z_{end} = 768 cm, dz = 64 cm) for t = 5.86 ms. The two current channels merge as they approach the anode at z = 1100 cm.

The data presented in Figure 3.1 is taken at an axial position close to the source (z = 64 cm). At this location, the flux ropes are the most symmetric, and its structure is clear. Farther from the source, the magnetic field relaxes to form a more stable state. In previous LAPD experiments, the currents of multiple flux merge [Pfister 1991, Van Compernolle 2011]. This can occur by magnetic reconnection or by magnetic field line diffusion in a resistive plasma. Using classical resistivity for 10 eV electrons ($\eta_{\|} = 1.9 \times 10^{-3}$ Ω-cm) and a radius of a = 3.75 cm, the resistive diffusion time ($\tau_\eta = \frac{4\pi a^2}{\eta c^2}$) is 92 μs. For an Alfvén speed of $\mathrm{v}_A = 1.6\times10^7$ cm/s and a flux rope length of L = 1100 cm, the Alfvén transit time ($\tau_A = L/\mathrm{v}_A$) is 68 μs, the same order of magnitude as τ_η. Figure 3.2 shows the axial development of the two flux ropes merging into one.

3.3 – TEMPERATURE AND DENSITY

Electrons emitted from the LaB_6 source generate additional heating and ionization that is spatially correlated with J_z. As a result of this addition heating and ionization, the core of the flux ropes will be hotter and denser than the surrounding medium. In the experiments presented here, core densities in the ropes rise to five times greater than the background plasma; and temperatures in the core may be twice as hot. Figure 3.3a and Figure 3.3c show a line profile of temperature and density across one of the flux ropes (a = 3.75 cm, L = 1100 cm, B_z = 330 G, I_{FR} = 300 A) – close to the line-tied position (z = 64 cm). The profile corresponds to the same position and time as the one in Figure 3.1c. At this axial location, $\delta\mathbf{J}\sim 0$ and $\delta\mathbf{B}\sim 0$; and therefore, good spatial reconstruction of the temperature and density is available from Langmuir probe analysis.

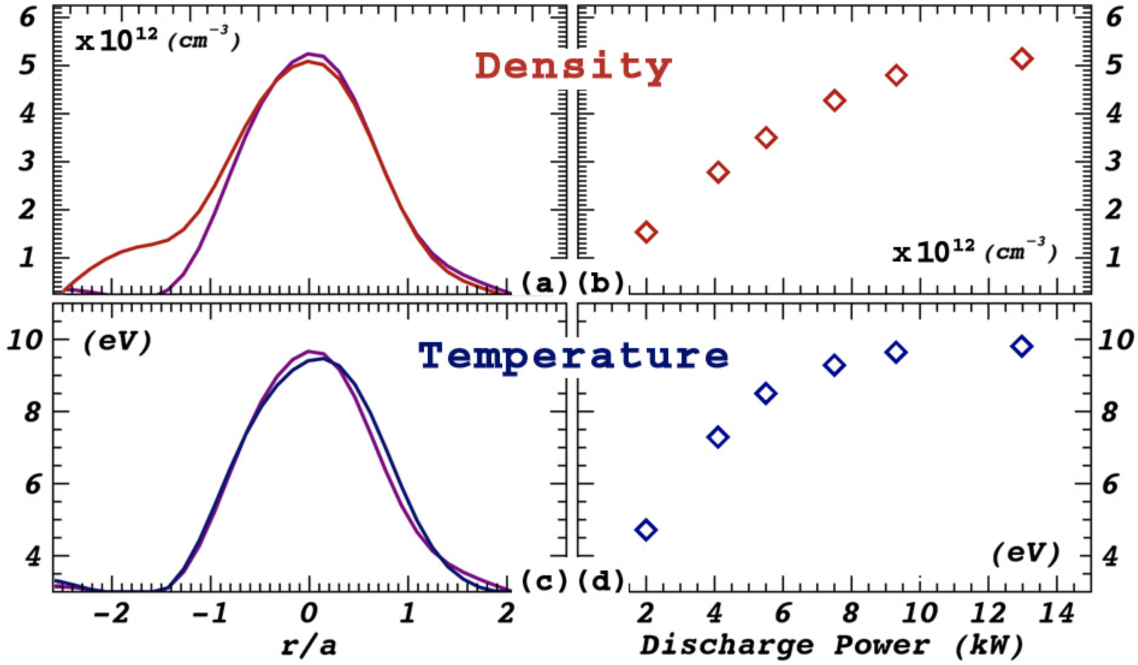

Figure 3.3 – **(a)** The density profile (red) of a single flux rope at z = 64 cm. The values of spatially correlated with J_z (purple). **(b)** The core density of the flux rope depends with the discharge power of the LaB_6 cathode. **(c)** The temperature profile (blue) of a single flux rope at z = 64 cm. The values are spatially correlated with J_z (purple). **(d)** The core temperature of the flux rope depends with the discharge power of the LaB_6 cathode.

The temperature and density are shown to depend on discharge power rather than the discharge current or voltage independently. To test this, a series of localized temperature and density measurements was taken for varying discharge currents and discharge voltages for a single flux rope (a = 2.5 cm, L = 1100 cm, B_z = 330 G). The process by which these measurements were made was described in Section 2.3.1. As the flux rope passes by a fixed probe, a spike in the temperature and density is observed; thereby, the core plasma parameters are determined. The results are plotted in Figure 3.3b and Figure 3.3d. The measurements begin to plateau at 10 kW of power, where the energy no long goes into heating and ionization. The temperature limit comes from a balance between the input power and factors, such as the thermal flux of electrons, recombination at the walls, radiation from electron-neutral and electron-ion collisions, inelastic collisions of electrons and ions with neutrals, and charge exchange.

3.4 – MHD EQUILIBRIUM

The elevated temperature and density inside the current channel leads to the poloidal current seen in Figure 3.1b. These currents, which are responsible for the drop in the magnetic field inside the flux rope, result from a balance between the $\mathbf{J}\times\mathbf{B}$ force and the strong radial pressure gradients. This is given according to MHD equilibrium:

$$\frac{1}{c}\mathbf{J}\times\mathbf{B} = \boldsymbol{\nabla}P_{\mathrm{e}} \tag{3.1}$$

where the ions are assumed to be cold and P_{e} is approximated by $P_{\mathrm{e}} = n_e T_e$. From the measurements presented in the previous sections, Eq. 3.1 was directly calculated from the data. The perpendicular force balance is plotted in Figure 3.4 for two axial locations (z = 64 cm, z = 510 cm, t = 5.45 ms). In Figure 3.4b and Figure 3.4d, the color table scales with $|\mathbf{J}\times\mathbf{B}|$ while the contours correspond to $|-\boldsymbol{\nabla}\mathrm{P}_e|$. A line profile is taken across one of the flux ropes at each axial location. The RHS and the LHS of Eq. 3.1 show good agreement in the data. In absence of the fully volumetric temperature measurements from a swept Langmuir probe, temperature may be estimated from $\mathbf{J}\times\mathbf{B}$.

Because of the force balance, magnetic flux ropes have traditionally been considered paramagnetic. The paramagnetic nature of a gas discharge in an external magnetic field is a well-known phenomenon – first explored in the 1950s [Bickerton

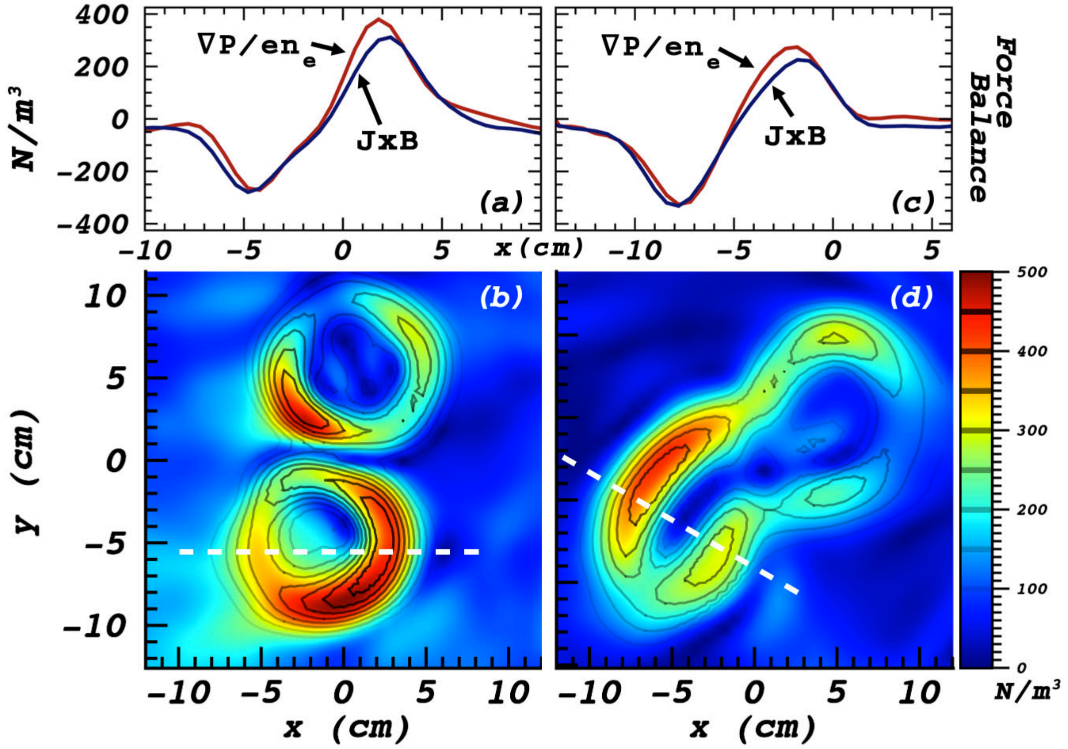

Figure 3.4 – **(a)** A line profile across one of the flux ropes to demonstration the pressure forces are balanced by the **J**×**B** forces at z = 64 cm. **(b)** A cross-section of the flux rope at z = 64 cm. The color table scales with $|\mathbf{J}\times\mathbf{B}|$ while the contours correspond to $|-\nabla P_e|$. The two show good agreement. **(c)** A line profile across one of the flux ropes to demonstration the pressure forces are balanced by the **J**×**B** forces at z = 510 cm. **(d)** A cross-section of the flux rope at z = 510 cm. The color table scales with $|\mathbf{J}\times\mathbf{B}|$ while the contours correspond to $|-\nabla P_e|$. The two show good agreement.

1958]. As long as the external, magnetic field (or "seed" field) is above a certain threshold, the gas discharge has the possibility of amplifying that field. This occurs when highly conductive plasma traps and compresses the axial field under the influence of the self-generated magnetic field from the discharge. Previous flux rope experiments fielded by [Hsu 2003] have observed amplification of the background magnetic field. [Paz-Soldan 2011], in addition, observed a transition from diamagnetism to paramagnetism as the flux rope transitioned to high currents.

The diamagnetism of the magnetic flux ropes generated in the LAPD is in contrast to these experiments. The current necessary to trigger the transition from a diamagnetic flux rope to a paramagnetic one can be estimated. For a flux rope of current I with a uniform current density and a radius of a = 3.75 cm, Eq. 3.1 can be rewritten to obtain the threshold:

$$-\nabla P_e < \frac{2I^2}{\pi a^3} \tag{3.2}$$

Under the conditions in the LAPD, the flux rope current would have to exceed 500 Amps, larger than the emission capabilities of the LaB_6 source (~10 A/cm^2).

3.5 ELECTRIC FIELD

In the LAPD, magnetic flux ropes are electrostatically negative with respect to the ambient medium in which they reside. The plasma potential inside the ropes depends on the discharge voltage the current in the rope. This has important consequences for the development of magnetic helicity associated with the two, interacting magnetic flux ropes. An electric field inside the experimental volume acts as a source or sink of magnetic helicity ($\int \mathbf{E} \cdot \mathbf{B}\, dV$); and a potential difference across a magnetic flux surface is a source of helicity injection $\left(\int \phi_p \mathbf{B}\, dS\right)$.

Figure 3.5 shows two x-y cross-sections associated with the two magnetic flux ropes at z = 64 cm and z = 510 cm. The color bar represents the plasma potential inside the flux ropes while the vectors represent the perpendicular electric field. The radial component of the electric field is the primary component – on the order of 10^2 V/m. The axial electrostatic field, on the other hand, is on the order of 1 V/m (not shown in the figure). On average, the plasma potential drops 4 V/m along the flux rope. This is consistent with estimates of $\mathbf{E} = \eta\mathbf{J}$, using classical resistivity and 6 eV electrons.

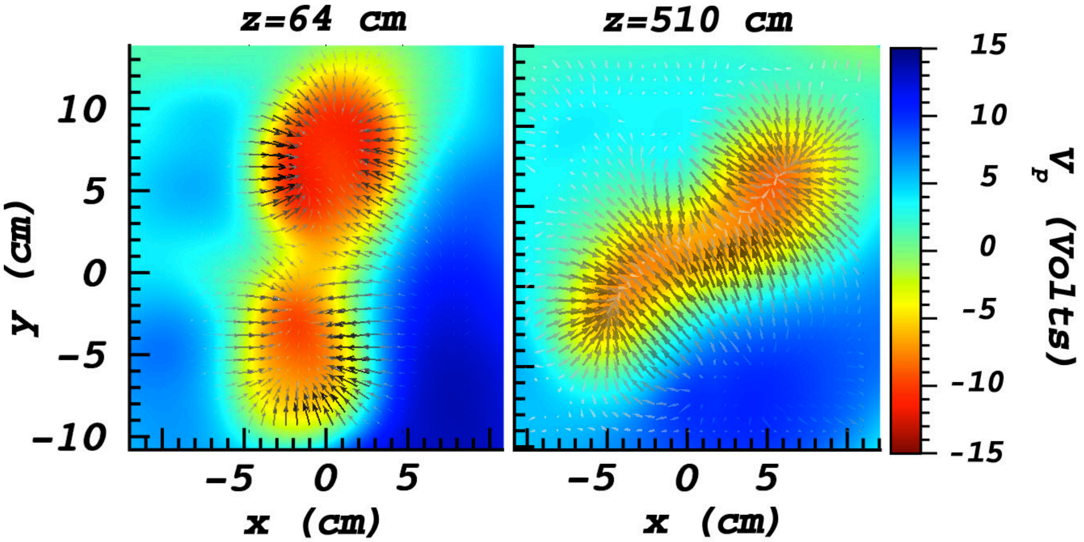

Figure 3.5 – **(a)** The plasma potential inside the two flux ropes at z = 64 cm and t = 5.45 ms. The electric field vectors point toward the center of each rope. **(b)** The plasma potential inside the two flux ropes at z = 510 cm and t = 5.45 ms. The electric field vectors point toward the center of each rope.

The current in the single flux rope (a = 2.5 cm, L = 1100 cm, B_z = 330 G) was increased between 20 – 110 A at a fixed discharge voltage (V_D = 100 V). The emissive probe was fixed in space (x,y,z) = (5,0,160) cm. As the flux rope moved passed the probe, a drop in the signal was observed. Using electron temperature measurements at the same location, the plasma potential was calculated as a function of time for this location. An example time trace of the plasma potential is plotted in Figure 3.6a. The plasma potential of the background medium and the core of the flux rope are label in the figure. These measurements are taken with respect to the walls of the device.

The scaling of the plasma potential with discharge current at a fixed discharge voltage (V_D = 100 V) is plotted in Figure 3.6b. Here, the plasma potential is referenced with respect to an electrode in the ambient plasma. The drop in the potential is on the order of a few volts; however, over the scale of a few centimeters, the force $-en_e\nabla\phi_p$ is greater than the pressure gradients or the **J**×**B** term in Section 3.5.

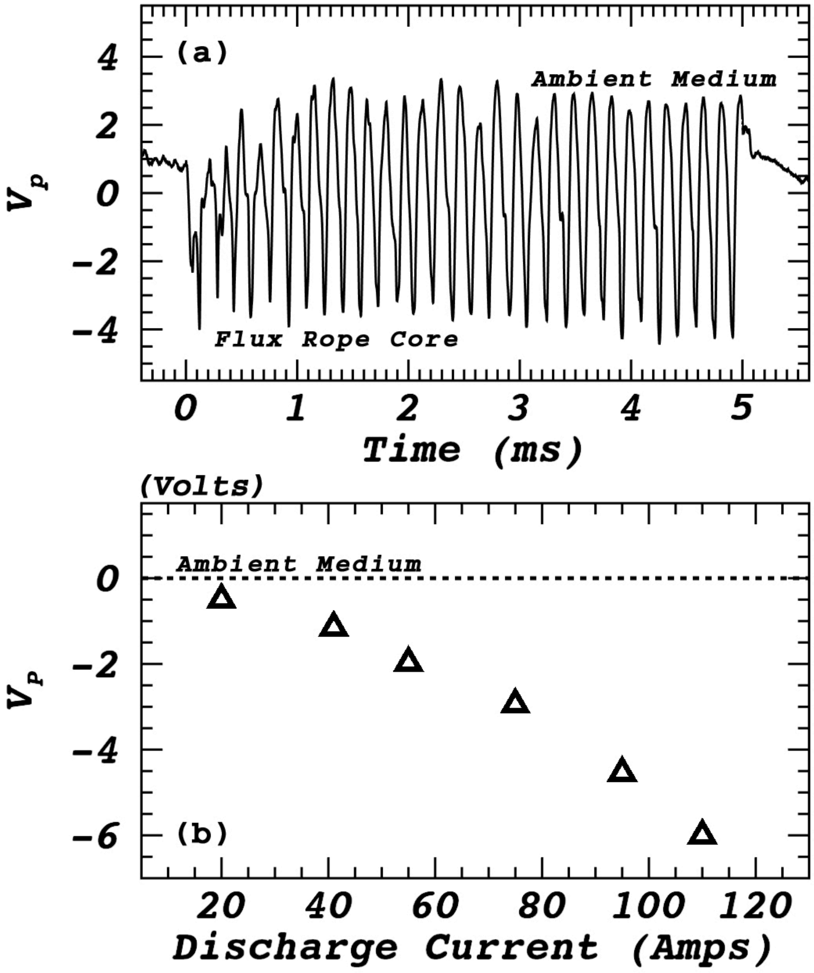

Figure 3.6 – **(a)** The plasma potential measured by the emissive probe at (x,y,z) = (5,0,160) cm for a single LAPD discharge (I = 95 A, V = 100 V). As the flux rope passes by the probe, a drop in the plasma potential is observed. **(b)** The scaling of the core plasma potential as a function of discharge current.

3.6 ION FLOWS

Because the ion flow is a factor in the kink mode dispersion relation and to calculations of canonical helicity, a brief discussion of the ion flow is presented here. In the presence of axial ion flow, the threshold at which the flux rope becomes unstable is lowered. The frequency of the kink mode changes with the magnitude and direction of the flow [Ruytov 2006]. Figure 3.7 shows a typical radial profile of axial flow for a single flux rope. The flow is not localized to the flux rope but broadened around it. The axial flow peaks at a Mach number of M_z = 0.25 and points toward the anode. With an electron temperature of 10 eV, it is approximately equal to v_z = 3.7×10^5 cm/s. Because the Alfvén speed in these experiments is over ten times the sound speed, the peak ion flow v_z expressed as a fraction of the Alfven speed is $\mathrm{v}_z/\mathrm{v}_A$ = 0.02.

In Chapter 6, ion canonical helicity is calculated during the collision and reconnection of two magnetic flux ropes. Ion canonical helicity describes the linkage of flux surfaces associated with canonical vorticity ($\Omega_i = e\mathbf{B} + m_i\nabla\times\mathbf{v}$), the linear combination of the magnetic field and vorticity (see Chapter 6 for further discussion). The primary component of vorticity is comes from perpendicular plasma flows, which spiral around the flux ropes in the $\mathbf{E}\times\mathbf{B}$ direction. Figure 3.8a shows the perpendicular flow associated with two magnetic flux rope at z = 510 cm. The magnitude of the flow reach a maximum at approximately $\mathrm{v}_\perp/c_s \sim$ 0.5. The perpendicular flow does not contribute appreciably to the force balance ($\rho\frac{\mathrm{v}_\perp^2}{r} \sim$ 1 N/m^3) – a hundred times less than the contribution from $\mathbf{J}\times\mathbf{B}$.

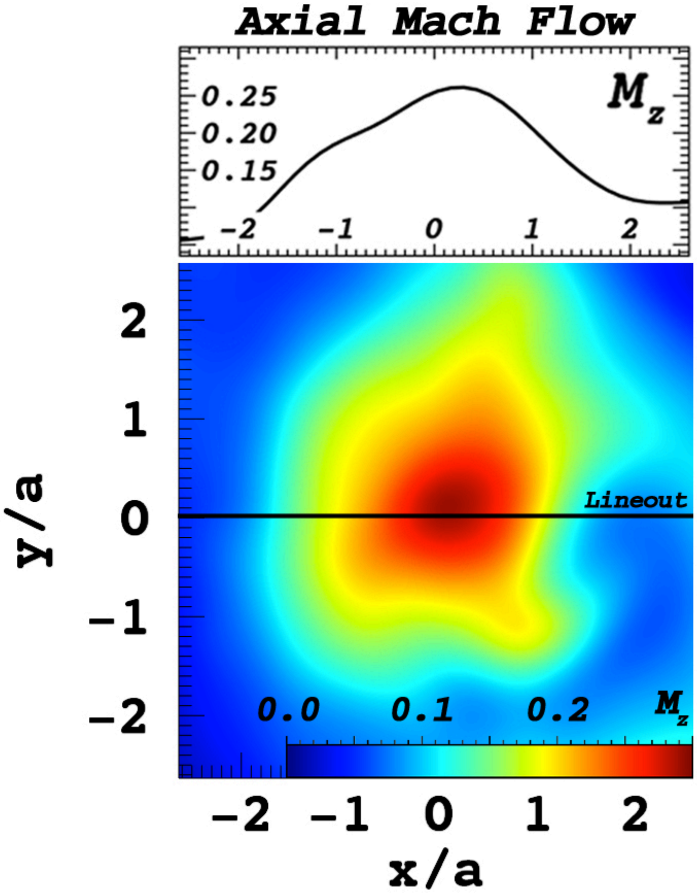

Figure 3.7 – An x-y cross-section of a single flux rope at z = 332 cm. The figure shows the axial Mach flow. A lineout is presented above the figure and peaks at 0.25, corresponding to approximately 3.7×10^5 cm/s.

The perpendicular flow, however, has a significant effect on ion canonical vorticity. Figure 3.8b shows the vorticity ($m_i\nabla\times\mathbf{v}$) associated with two magnetic flux ropes at z = 510 cm. The plot is normalized to the background magnetic field (eB_z) to illustrate the contribution of vorticity to canonical vorticity. Positive vorticity is associated with the core of the flux ropes. This leads to calculations of canonical helicity which differ up to 40% percent from traditional calculations of magnetic helicity.

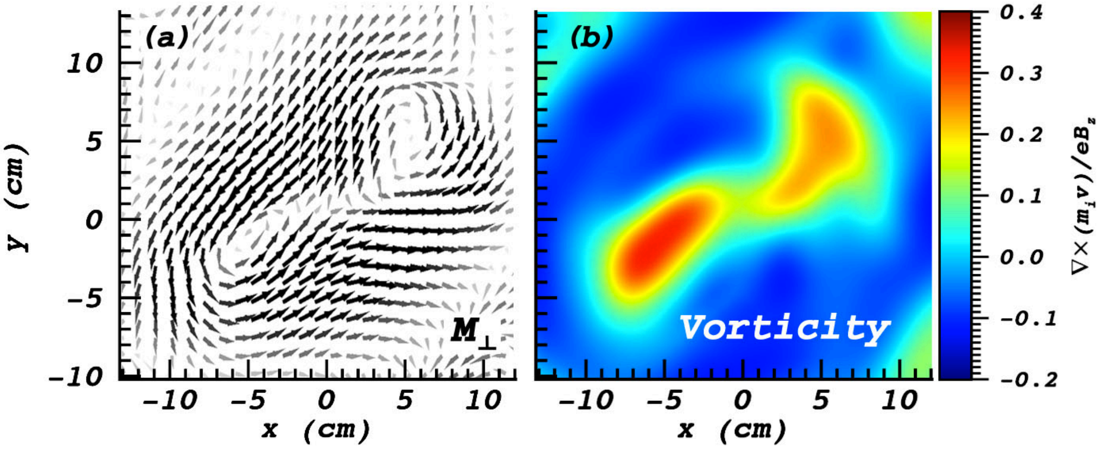

Figure 3.8 – **(a)** The perpendicular ion flow at $z = 510$ cm and $t = 5.45$ ms. The ions spiral around the two flux rope in the **E**×**B** direction and reach a maximum of approximately $v_\perp/c_s \sim 0.5$. **(b)** The vorticity associated with (a). The values are normalized to the background magnetic field to show that the contribution of vorticity to ion canonical vorticity is up to 40%.

3.7 CONCLUDING REMARKS

In summary, the flux ropes are three times hotter ($T_e = 12$ eV) and five times denser ($n_{rope} = 5\times10^{12}$ cm^{-3}) than the background plasma with a current density as high as 5 A/cm^2. The perpendicular pressure forces point radially outward from the center of each flux rope and are balanced by the inward forces of **J**x**B**. The electrostatic field points inward toward the center of each flux rope as the ropes are electrostatically negative with respect to the plasma background. The electrostatic field generates **E**x**B** flows that spiral around the two flux ropes, and this accounts for magnetic helicity. The vortical flow plays a major role in calculations of canonical helicity.

CHAPTER 4 – *ORBITAL ROTATION OF THE FLUX ROPE*

4.1 – THE KINK INSTABLITY

The external magnetic field provides the stabilizing restoring force that gives the flux rope its shape and form. If the flux rope becomes displaced from its axis, the restoring force results in oscillations about the equilibrium position. These oscillations take the form of a standing Alfvén wave between the mask and the anode. However, if the current flowing along the background field exceeds a certain threshold, the flux rope will become unstable. Its displacement from equilibrium will grow exponentially on the order of an Alfvén transit time. This instability is the kink instability, a well-studied MHD instability [Shafranov 1956, Kruskal 1958].

The kink instability is the main driver of flux rope dynamics in the LAPD. Upon initiation of the instability, the flux ropes are displacement from their equilibrium position. The growth of the instability eventually saturates, and the kinked flux ropes move in coherent fashion about the z-axis. The coherent nature of this motion provides the repeatability needed for three-dimensional reconstruction of magnetic fields and other physical quantities from which canonical helicity may be calculated. This chapter will focus on an experiment performed on a single flux rope. The flux rope was driven kink unstable under varying conditions, and the coherent behavior of the flux rope was observed. This chapter presents the results and will seek to explain the behavior of the flux rope under this coherent mode.

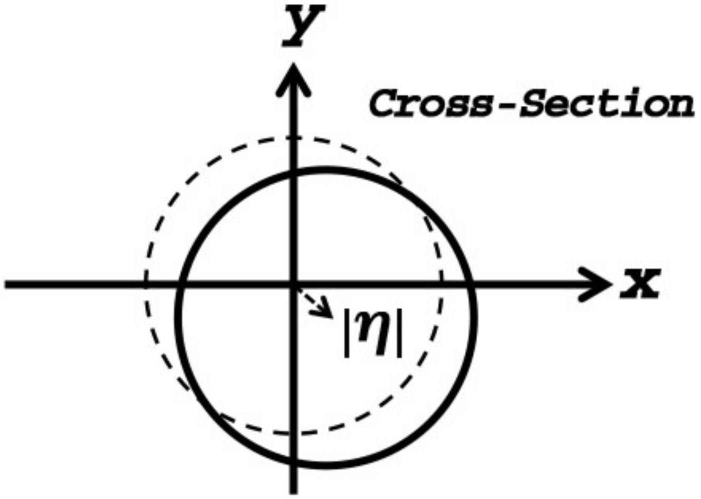

Figure 4.1 – A cartoon demonstrating the “gentle wiggle” which Eq. 4.1 describes. The dashed circle represents the equilibrium position of the flux rope in the x-y plane while the solid curve shows the cross-section of the flux rope as it is displaced $|\eta|$, from the equilibrium position.

For the geometry of a single, flux rope, embedded in a vacuum with fix-free boundary conditions an analytic theory has been constructed [Ruytov 2006]. This analytic theory will be referenced many times in this throughout chapter. The displacement of a slender plasma column can be described by the follow equation:

$$\frac{\partial^2 \eta}{\partial t^2} = 2\mathrm{v}_A^2 \left(\frac{\partial^2 \eta}{\partial z^2} + i k_0 \frac{\partial \eta}{\partial z} \right). \tag{4.1}$$

Here, v_A is the average Alfvén velocity inside the flux rope, $k_0 = \frac{B_\theta}{aB_z}$ (with the poloidal magnetic field B_θ taken at the edge of the flux rope), and is $\eta(z;t)$ is a complex variable that describes the position of the flux rope with respect to its equilibrium. In cylindrical coordinates, the central position of the flux rope can be expressed as (r,θ,z) = $(|\eta|, \tan^{-1}\left(\frac{Im(\eta)}{Re(\eta)}\right), z)$. Figure 4.1 helps visualize the “gentle wiggle” the equation describes. When $k_0 \rightarrow 0$ (i.e. the current in the flux rope goes to 0 A), Eq. 4.1 describes a shear Alfvén wave.

To solve Eq. 4.1, a set of boundary conditions must be imposed. The theoretical threshold at which the flux rope goes unstable depends on this set of boundary conditions. For a flux rope fixed at the mask and free to slide about the anode, [Ruytov 2006] uses the following boundary conditions:

$$\eta|_{z=0} = 0 \tag{4.2}$$

$$\left(\frac{\partial\eta}{\partial z} + \frac{ik_0}{2}\eta\right)\Big|_{z=L} = 0 \tag{4.3}$$

This set of boundary conditions has been used by [Intrator 2007] and [Furno 2006] to explain the kink threshold observed in the Reconnection Scaling Experiment. A discussion into the validity of this boundary condition is performed in Appendix A. For a cylindrical flux rope fixed at the mask and free to slide about the anode, the structure will go unstable when

$$I_{FR} > I_{kink} = \frac{\pi a^2 B_z c}{2L} = \frac{I_{KS}}{2} \tag{4.4}$$

This is half the Kruskal-Shafranov limit (Eq. 1.1). With a flux rope length of $L = 1100$ cm, a radius of $a = 2.5$ cm and a magnetic field of 330 G (the characteristics of the flux rope explored in this chapter), the current threshold is 30 A.

4.2 – TRANSITION INTO UNSTABLE MODE

The flux ropes generated in the series experiments presented here are designed to be driven kink unstable. As the flux ropes transition from stable to unstable, the dynamics of the current system dramatically change. This is shown in Figure 4.2: two magnetic time traces on either side of the kink threshold (one at I = 20 A, one at I = 75 A, with B_0 = 660 G). In the stable case, the perpendicular magnetic oscillations are small compared to the stable magnetic field. These small oscillations correspond to standing Alfvén waves. They appear at 15 kHz, which match the frequency estimates of $f = \mathrm{v}_A/4L$. Above the instability threshold, the magnetic signals observe large-scale oscillations in the perpendicular and parallel direction. This behavior cannot be explained by the set of equations present above – as its solution predicts only imaginary frequencies above $I_{KS}/2$.

As discussed in the Chapter 1, these large oscillations correspond to motion of the flux rope after it has been freed from its axis. It is sometimes called a "rotating helical equilibrium," a quasi steady state in which a helically distorted flux rope rotates about the equilibrium position [Paz-Soldan 2011]. The term "equilibrium" is associated with this motion because in the frame of the flux rope, the plasma appears to be in equilibrium. Magnetic signals resulting from this behavior are highly coherent, repeatable, and well correlated in space. Therefore, any magnetic signals shown in this chapter are characteristic magnetic signals anywhere in the experimental volume. By plotting the observed, real frequencies, associated with this motion, as a function of current in the rope (Figure 4.3), the transition into this coherent behavior is observed.

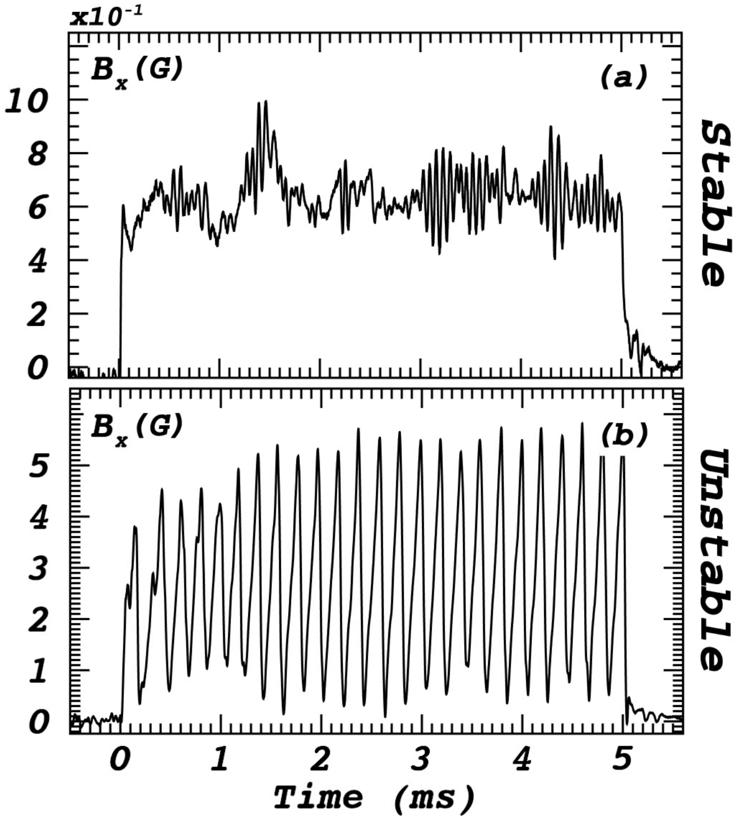

Figure 4.2 – **(a)** A magnetic time trace at (x, y, z) = (3, 0, 850) cm for a flux rope I = 20 A, L = 1100 cm, and B_0 = 660 G. The current in the rope is below the threshold needed to trigger the kink instability. The oscillations (15 kHz) correspond to standing Alfvén waves. **(b)** A magnetic time trace at (x, y, z) = (3, 0, 850) cm for a flux rope I = 75 A, L = 1100 cm and B_0 = 660 G. The current in the rope is above the threshold needed to trigger the kink instability. The oscillations correspond to the "rotation helical equilibrium."

The transition occurs near half the Kruskal-Shafranov limit. The data which recorded the shift was taken from a fixed magnetic probe (x,y,z = 5,0,870 cm). The discharge voltage was held fixed at 100 Volts while the LaB_6 source was cooled over a several hour period. As the source was slowly cooled, magnetic data was collected from successive discharges until the emission current from the source approached 0 A. In this way, the transition between a stable flux rope and unstable on could be observed while simultaneous eliminating any effects from changing electrical boundary conditions. A Fourier transform of the data was taken and averaged. The results are displayed in Figure 4.3. After the instability initiates, the frequency is shown to depend on with the current in the rope. This behavior has been seen in previous experiments [Intrator 2007, Paz-Soldan 2011]. However, at some point, the observed frequency saturates.

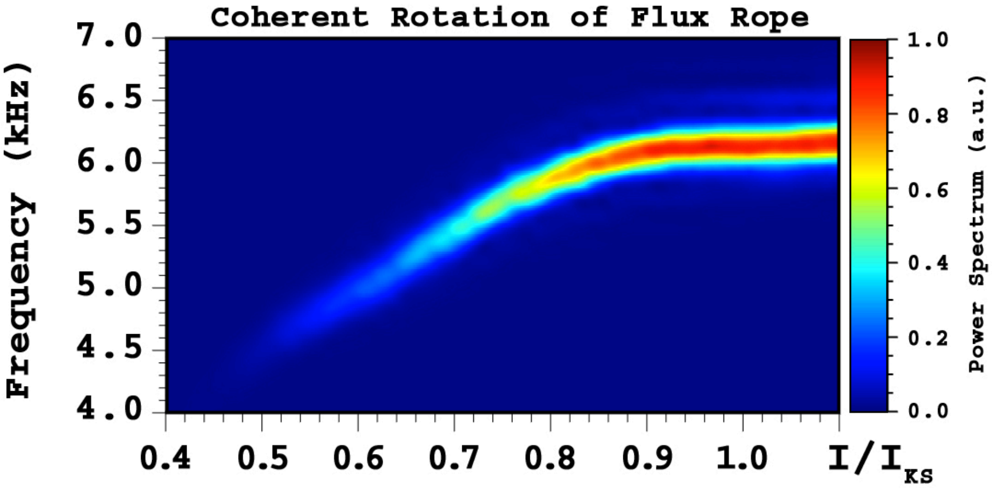

Figure 4.3 – The transition of the flux rope into coherent rotation. This mode is associated with the kink instability, which is triggered at $I_{KS}/2$. Once the mode is initiated, its frequency increase with the current in the rope – then saturates.

A closer investigation of this mode reveals multiple peaks in the Fourier spectrum. This is plotted in Figure 4.4a. The lowest peak is the coherent mode (which was displayed in Figure 4.3) while its harmonics are produced by a displacement that is on the order of the flux rope radius ($\frac{|\eta|}{a} \sim 1$). By isolating and filtering out these peaks, a mode structure can be identified, corresponding to an m=1, m=2, etc. This is shown in the following graph. This gives the anticipation of a flux rope description as a wave phenomenon. However, each mode is in phase with one another, not being excited

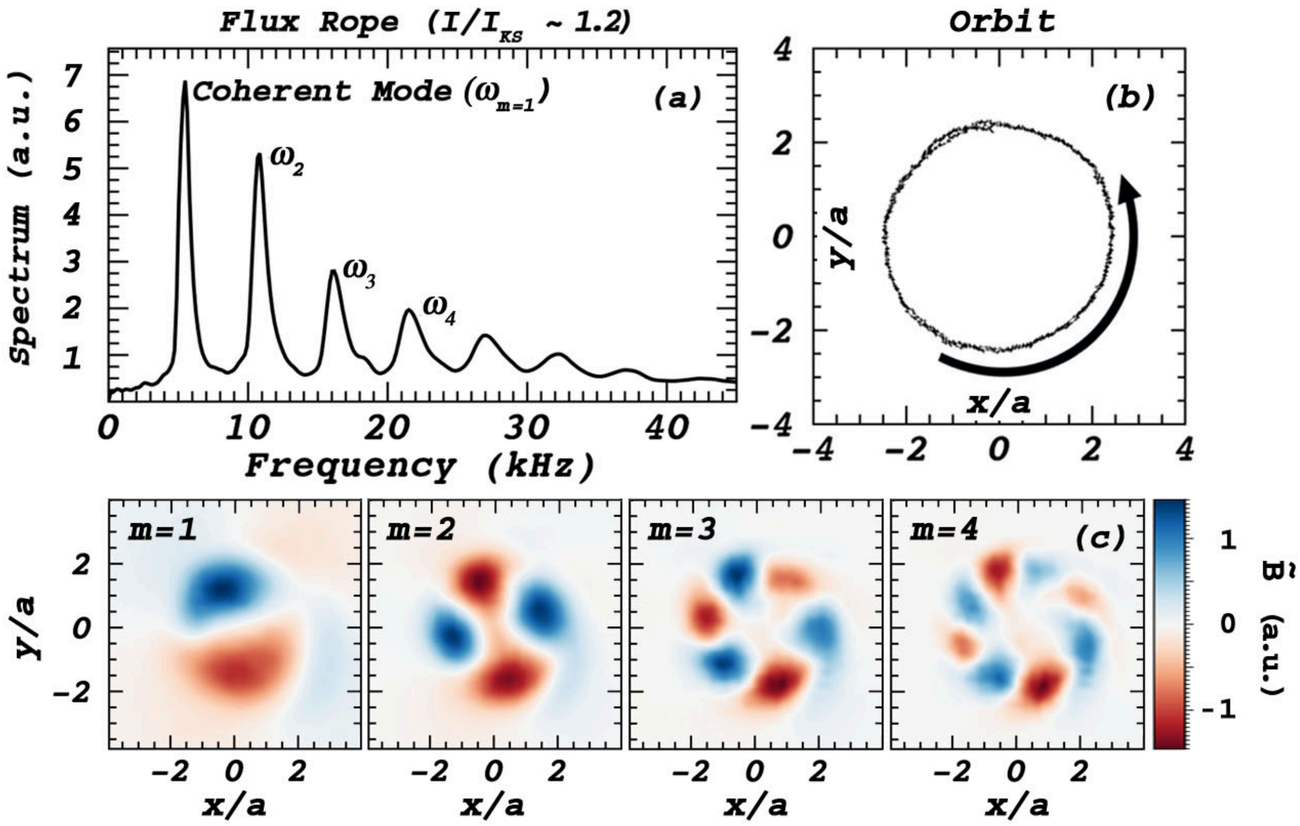

Figure 4.4 – **(a)** The frequency spectrum for a flux rope ($a = 2.5$ cm, $L = 1100$ cm, $B_0 = 330$ G). The flux rope is kink unstable and undergoes coherent rotation of the plasma column in the x-y plane. The coherent mode is the lower peak in the spectrum while its harmonics are produced by displacement on the order of the radius of the rope. **(b)** The instantaneous central position of the flux rope over several rotations about the axis. **(c)** The filtered frequencies seen in the spectrum. The spatial feature show m=1,2,3… oscillations in the plane such that $\tilde{B} = B(r)e^{i(m\theta-\omega_m t)}$.

randomly as the discharge power increases. Similarly, both the real and imaginary frequencies predicted by Eq. 4.1 are not evenly spaced – as is observed here. Instead, the collection of these peaks is the manifestation of approximate circular motion of the flux rope in the transverse plane, whose radius of rotation in a plane is greater than (or on the order of) the size of the flux rope.

To demonstrate the motion of the displaced flux rope, Figure 4.4b shows the instantaneous central position of the flux rope over several rotations about the axis. The central position was calculated by weighting the positions according to the local current density. The rotation is right-handed when the current is anti-parallel to the background magnetic field. In one experiment, the positions of the LaB_6 cathode and its corresponding anode were exchanged. In this case, the current was flipped so it was parallel to the background magnetic field. Keeping the same coordinate system, the coherent rotations remained right-handed with respect to the background magnetic field.

4.3 – MODEL OF COHERENT ROTATION

To explore how the transitory motion manifests itself in the Fourier analysis, a simple model has been created. A virtual, cylindrical flux rope with a Gaussian current density profile was constructed. In the model, the flux rope is moved in the transverse plane in increasing concentric circles (from r_{cirle}/a = 0 – 4). The flux rope is moved around each circle with constant velocity and a constant period of rotation. A virtual probe is placed somewhere along the x-axis between x_{probe}/a = 0 – 4. As the flux rope moves in greater and greater circles, the virtual probe samples more of a magnetic profile that varies as 1/r rather than r. This gives an appearance of waveform steepening on the virtual probe, which, in the case of a Fourier transform, leads to the harmonics of the coherent rotation. These are identical to the ones seen in the experiment.

Mathematically, this model can be expressed as the sum of a series. First, consider a current density profile in the x-y plane that takes the form

$$J_z = J_0 e^{-\frac{r^2}{2a^2}} \tag{4.5}$$

where a is the radius of the flux rope and J_0 is the arbitrary maximum current density. This produces a magnetic profile, calculated by Ampere's law, given by

$$B_\theta = \frac{J_0 a^2}{r}\left(1 - e^{\frac{-r^2}{2a^2}}\right) \tag{4.6}$$

If the flux rope is displaced by $\mathbf{r}_{\boldsymbol{FR}} = R\cos(\omega_0 t)\,\hat{\mathbf{x}} + R\sin(\omega_0 t)\,\hat{\mathbf{y}}$ and a virtual probe is placed along the x-axis at $\mathbf{r}_{\boldsymbol{p}} = x_p\hat{\mathbf{x}}$, then the virtual probe will record a magnetic field that is given by

$$B_{VP} = \frac{J_0 a^2}{\left|\mathbf{r}_{\boldsymbol{FR}} - \mathbf{r}_{\boldsymbol{p}}\right|}\left(1 - e^{\frac{-(\mathbf{r}_{\boldsymbol{FR}} - \mathbf{r}_{\boldsymbol{p}})\cdot(\mathbf{r}_{\boldsymbol{FR}} - \mathbf{r}_{\boldsymbol{p}})}{2a^2}}\right) \tag{4.7}$$

The exponential can be converted into a power series. Letting $\beta = \frac{-2Rx_p}{R^2 + x_p^2}$, Eq 4.8 is converted:

$$B_{VP} = \frac{J_0 a}{\sqrt{2}}\left(\sum_{n=1}^{\infty}\frac{(-1)^{n+1}}{n!}\left(\frac{R^2 + x_p^2}{2a^2}\right)^{n-1/2}(1 - \beta\cos(\omega_0 t))^{n-1/2}\right) \tag{4.8}$$

Finally, $(1 - \beta\cos(\omega_0 t))^{n-1/2}$ can be expanded by the binomial theorem such that

$$B_{VP} = \frac{J_0 a}{\sqrt{2}}\left(\sum_{n=1}^{\infty}\frac{(-1)^{n+1}}{n!}\left(\frac{R^2 + x_p^2}{2a^2}\right)^{n-1/2}\sum_{k=0}^{\infty}\binom{n - \frac{1}{2}}{k}\alpha^k\cos^k(\omega_0 t)\right) \tag{4.9}$$

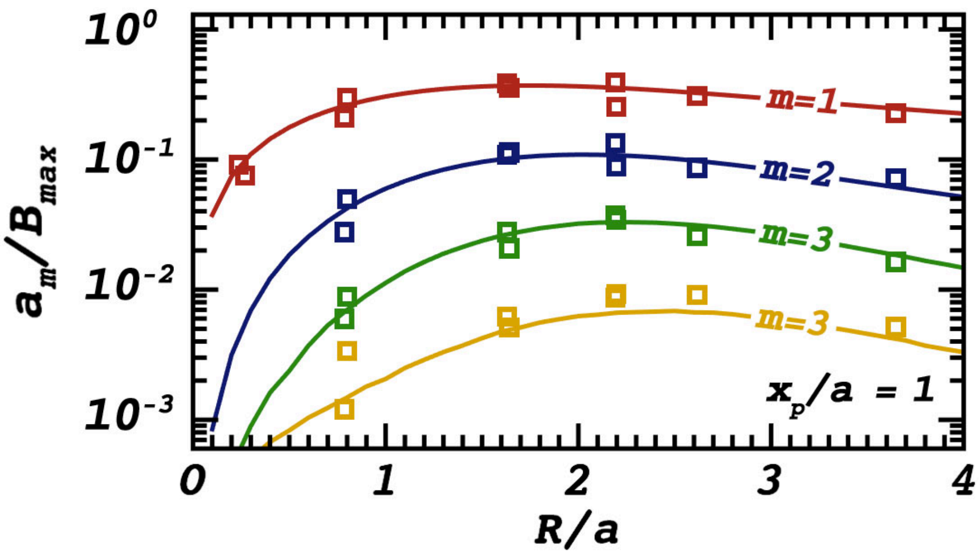

Figure 4.5 – Using simple circular motion of the plasma column as a model to explain the observed harmonics, the predicted (the solid curves) and observed amplitudes (the square points) are plotted.

The preceding mathematical exposition that led to Eq. 4.9 was done to demonstrate that the signals measured by the virtual probe can be expressed as a sum of $\cos^k(\omega_0 t)$. When the Fourier transform is taken of Eq. 4.9, $\cos^k(\omega_0 t) \xrightarrow{\mathcal{F}} \sum_{l=0}^{k} \binom{k}{l} \delta(\omega_0(2l-k)-\omega)$. Therefore, with a single input frequency ω_0 and simple circular motion of a Gaussian, current profile, the Fourier transform of magnetic signals is expressed as harmonics of the coherent, rotation frequency:

$$\mathcal{F}\{B_{VP}\} = \sum_{m=0}^{\infty} \mathrm{a}_m \, \delta(\omega - m\omega_0) \tag{4.10}$$

Figure 4.5 plots the amplitude a_m of the harmonics as predicted by the model as the flux rope moves in greater and greater concentric circles. The virtual probe is placed at

$x_p/a = 1$, the position of the experimental probe. Along side, the data is plotted to show a comparison between the predicted values and the ones observed. The data and the model show good agreement.

4.4 – ABSOLUTE DISPLACEMENT

Establishing that the observed amplitudes in the frequency spectrum are a function of the orbital radius (R_{Orb}) of the flux rope, a discussion of the absolute displacement of the column in the x-y plane is necessary. To do this, the total peak-to-peak variation in $\mathbf{B}(\mathbf{r})$ will be discussed as a placeholder for the numerous amplitudes a_m in the spectrum. When the proper boundary conditions are imposed, Eq. 4.1 yields the displacement of the flux rope. The solution takes the form:

$$\eta = R_{Orb}\left(e^{ik_1 z} - e^{ik_2 z}\right)e^{-i\omega t} \tag{4.11}$$

R_{Orb} is the maximum displacement of the flux rope from its equilibrium position within the whole experimental volume while k_1 and k_2 are calculated to be

$$k_1 = \frac{\pi}{2L} - \frac{k_0}{2} \tag{4.12}$$

$$k_2 = -\frac{\pi}{2L} - \frac{k_0}{2} \tag{4.13}$$

The orbital radius of the flux rope is then a function of axial location and is given by the absolute value of Eq. 4.1:

$$|\eta| = R_{Orb}\sin\left(\frac{\pi z}{2L}\right) \tag{4.14}$$

In other words, the flux rope exhibits no displacement at the mask ($z = 0$ cm) and enjoys maximal displacement where is it free to slide at the anode. A previous experiment performed on the LAPD [Van Compernolle 2011] as well as an experiment performed by [Intrator 2007] measured the displacement of the flux rope and confirmed it takes this form. Similarly, [Intrator 2007] demonstrated that the maximal displacement of the plasma column depends on the current in the ropes. This was also confirmed in this experiment. In addition, the depends on the discharge voltage was studied.

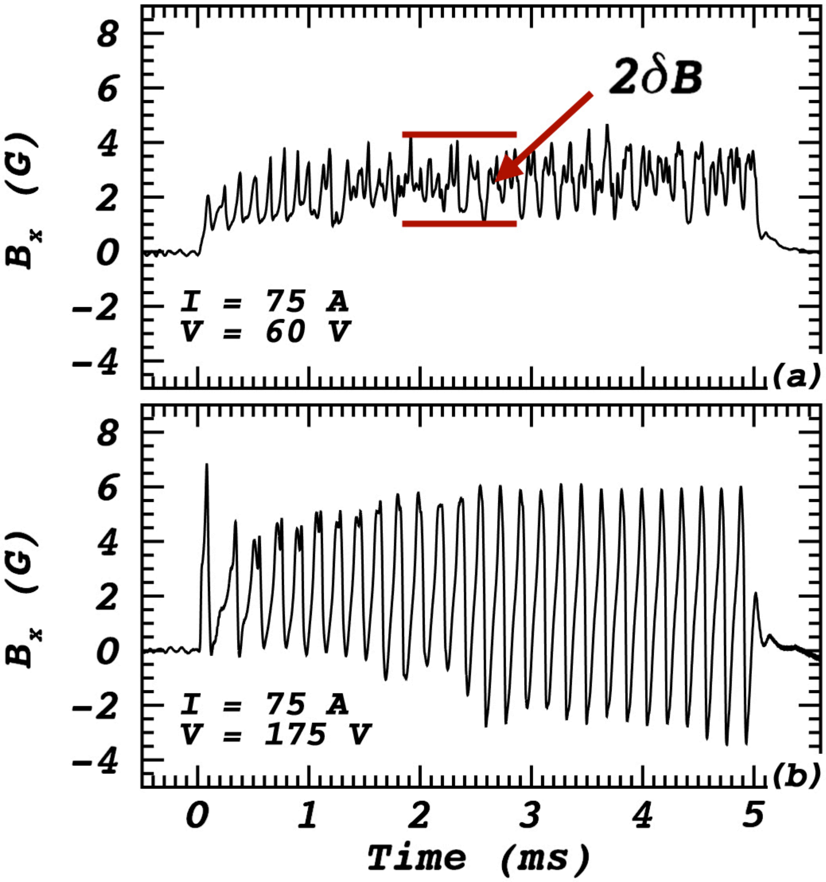

Figure 4.6 – **(a)** A magnetic time trace at (x, y, z) = (3, 0, 850) cm for a flux rope of 75 A and 60 V. The small oscillations in the signal are a function of the displacement of the flux rope from its axis. **(b)** A magnetic time trace at (x, y, z) = (3, 0, 850) cm for a flux rope of 75 A and 175 V. The large oscillations in the signal are a function of the displacement of the flux rope from its axis, demonstrating the displacement of the column varies with the discharge voltage independent of current.

As noted in Section 2.3, a series of experiments were performed on a flux rope ($a = 2.5$ cm, $L = 1100$ cm) in which the discharge current and discharge voltage were varied independently. In the case of fixed current ($I_D = 75$ A), the voltage was varied between 60 to 175 Volts. In the case of fixed voltage ($V_D = 100$ V), the current was varied between 20 to 130 Amps. In each case, the flux rope was kink unstable and the magnetic field was measured at a fixed location (x, y, z) = (3, 0, 850) cm.

The peak-to-peak variation in the magnetic field δB was recorded at this location and may be interpreted as the displacement of the plasma column. This presumption can be proven using the model presented in Section 4.3 for $R/a < 1$. However, [Intrator 2007] has already experimentally demonstrated that R_{Orb} is proportional to $\delta B/B_{max}$ (with $B_{max} = \frac{2I}{ac}$). Figure 4.6 shows two magnetic time traces at the same location. Each corresponds to the same discharge current but differs in discharge voltage ($V_D = 60$ V and $V_D = 175$ V). By increasing the discharge voltage on the LaB_6 source, the peak-to-peak variation in the field increased by a factor of three. The orbital radius of the flux rope scales with the voltage on the boundaries as well as the current in the rope.

To determine if there is a difference between the displacement of the plasma column with discharge current and the displacement of the plasma column with discharge voltage, one must examine plots δB as a function of discharge power as done in Figure 4.7. Instead of varying independently, δB is shown to vary with the discharge power. The displacement increases until the orbital radius exceeds the position of the probe. At this point, the probe has sampled the whole magnetic profile of the flux rope, which – to the probe – looks like an oscillation equal to B_{max}. Similar measurement can be made at different radial and axial location producing the same results.

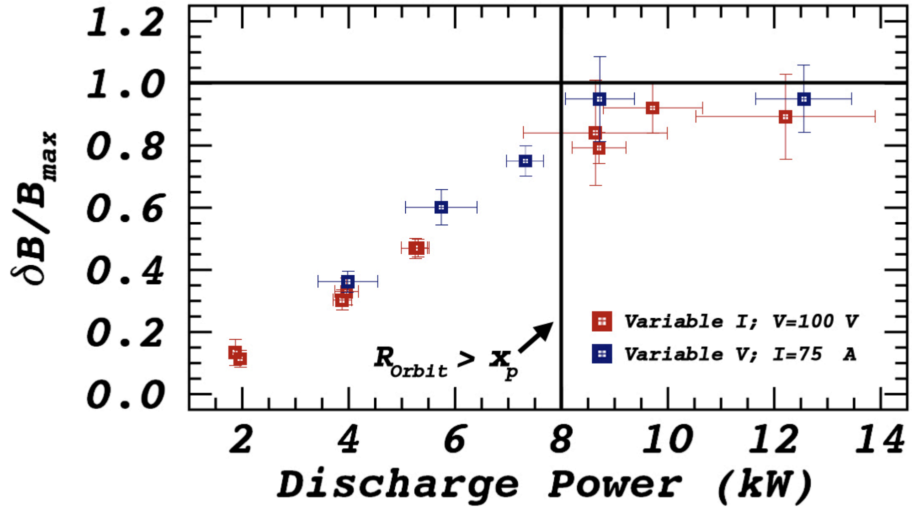

Figure 4.7 – The amplitude of oscillations observed from a fixed magnetic probe: (x, y, z) = (3, 0, 850) cm. This amplitude is a placeholder for the displacement of the flux rope from its axis. The displacement scales with discharge power, which is demonstrated by plotting two sets of data: 1) where current is fixed and the discharge voltage is varied and 2) where the discharge voltage is fixed and the current is varied. When the displacement of the flux rope becomes greater than the radial position of the probe, the amplitude of oscillations saturates.

4.5 – APPLICATION TO THE TWO FLUX ROPE SYSTEM

While this chapter focused on the motion of a single flux rope, the two flux rope system exhibits the same coherent rotation. The two flux rope system is unstable with $2I/I_{KS} \sim 4$. The kink threshold for this system corresponds to the expected fixed-free boundary condition from theory [Ruytov 2006], which was also demonstrated by experiment for a single flux rope in this chapter. Multiple modes arise in the Fourier transform of the two flux rope system just as in the single flux rope system, but the lowest mode is the primary mode of importance. The two flux ropes twist about one another and merge, but the coherent mode drives the pulsating reconnection events between the two flux rope. The flux rope collide and produce magnetic reconnection at regular intervals which correspond to the frequency of the coherent mode. These reconnect events will be identified in Chapter 6.

CHAPTER 5 – *CHARACTERISTIC PULSES AND CHAOTIC MOTION*

5.1 – TRANSITION IN SIGNALS

With an increase in flux rope current, the magnetic signals transition from a highly coherent signal to an incoherent one. Figure 5.1 shows a side-by-side comparison of magnetic signals from a single, kink-unstable flux rope with currents corresponding to 55 A, 75 A, and 130 A. The more random nature of the 130 A case holds significance in that it may represent a system driven into chaos. When the system degrades to this state, three-dimensional reconstruction of the data is not possible as reconstruction can only be done for time scales shorter than the autocorrelation time. Using the examples in Figure 5.1, the autocorrelation time for the 75 A flux rope is 4 ms, which is 20 times the period of the coherent mode and a majority of time over which the experiment was conducted (5 ms). For I_{FR} = 130 A, the auto-correlation time is only 200 μs.

The cause of the transition is not readily apparent. It is not caused by sudden variations in the emission of the LaB_6 source – as the variation in the current is $\delta I \sim 2\ A$. Neither does it appear to be dependent of the kink threshold, manifesting between 100 A and 125 A for both a single flux rope at 330 G and at 660 G. The behavior is connected

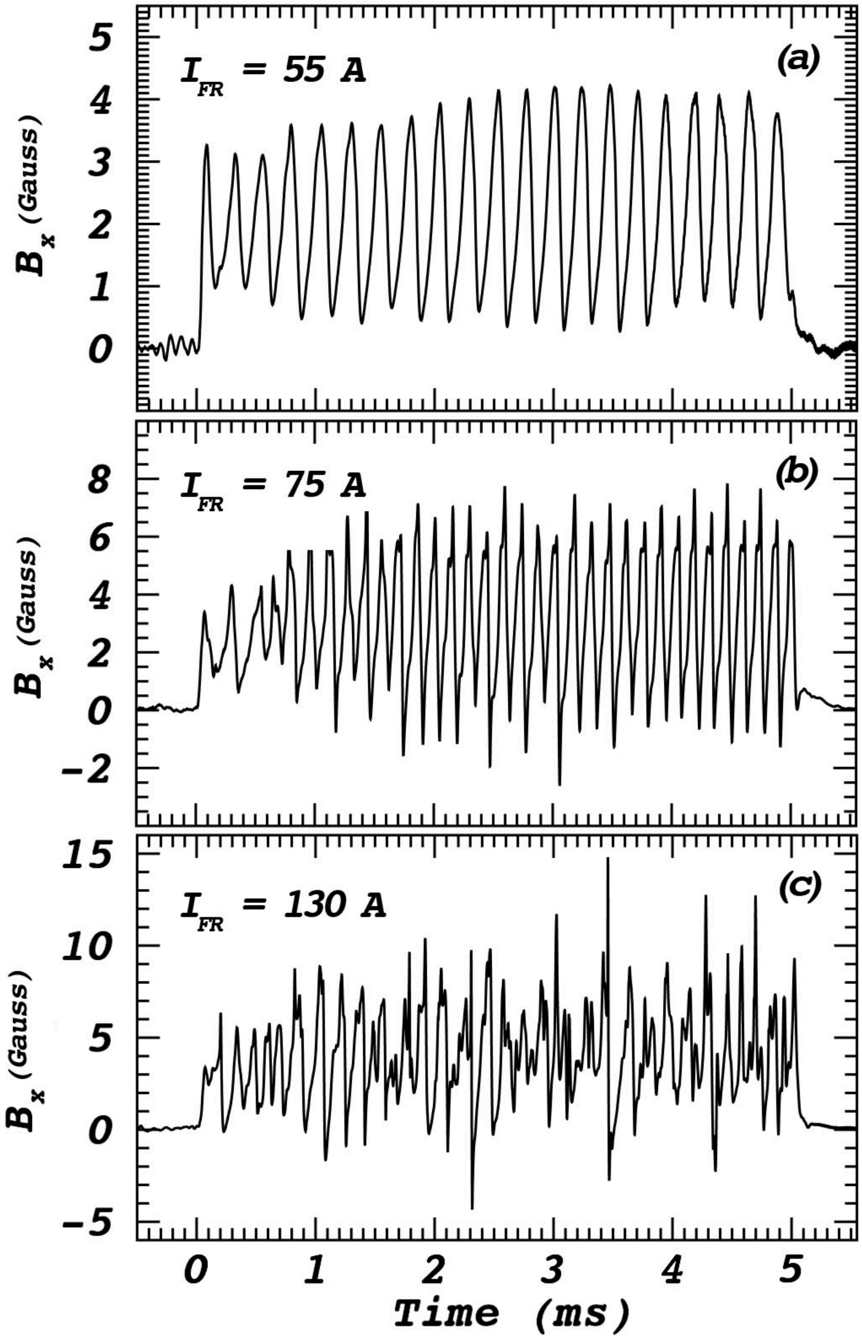

Figure 5.1 – A comparisons between of the types of magnetic signal seen in this dissertation: **(a)** Coherent oscillations (f_{FR} = 4 kHz) which signify a rotating helical equilibrium. **(b)** The same phenomena at higher frequency (f_{FR} = 6 kHz). The frequency increases with current in the flux rope. **(c)** A transition of the signals in a more incoherent, intermittent mode.

with the current in the rope and not connected with the total discharge power. Under the conditions of I_{FR} = 75 A and V_D = 175 V (13 kW; Figure 4.6b), the flux rope is highly coherent and never leaves electric contact with the anode. At the same discharge power for a flux rope I_{FR} = 130 A and V_D = 100 V, the signals are more random.

The incoherent behavior of the flux rope constrains the range of discharge currents over which three-dimensional reconstruction of the system is possible. Without volumetric data, global quantities like magnetic helicity cannot be calculated. Similarly, accompanying this intermittent behavior is the rise of a background spectrum. This background spectrum is not be predicted by simple, circular motion of a flux rope in the plane, yet it is visible even in when the flux rope exhibits coherent rotation. Understanding the link between the motion of the flux rope and this background spectrum is important when separating changes in helicity due to motion and changes in magnetic helicity due to magnetic reconnection.

In this chapter, we evaluate this incoherent, random behavior – identifying some of its defining characteristics. In addition, we will gauge whether or not this behavior is indicative of a chaotic process. The hypothesis is that the signals are indicative of a chaotic orbit rather than another turbulent process such as wave turbulence. To evaluate this hypothesis, the power spectrum will be used to identify characteristic structures, or pulses, in the data. This will lead to the conclusion that the incoherent, magnetic signals are produced by the displacement of the plasma column. Then, the Bandt-Pompe (BP) Probability distribution calculated and complexity-entropy (C-H) analysis performed. This will be used to demonstrate that the displacement is indicative of a chaotic process.

5.2 – FLUCTUATION POWER SPECTRUM

In Figure 5.2, the power spectrum is plotted for three discharge currents – each associated with a time trace in Figure 5.1. The plots are shown on a log-linear scale to call attention to the rise in the underlying background of each signal. Each background spectrum appears similar in form (a feature which will be discussed below). The background is not associated with a spectrum of waves. Instead, it is the product of a common, repeating pattern (or structure) found in the magnetic signals – regardless whether the signal is coherent or random. Because it is a common feature, a coherent flux rope will be considered first.

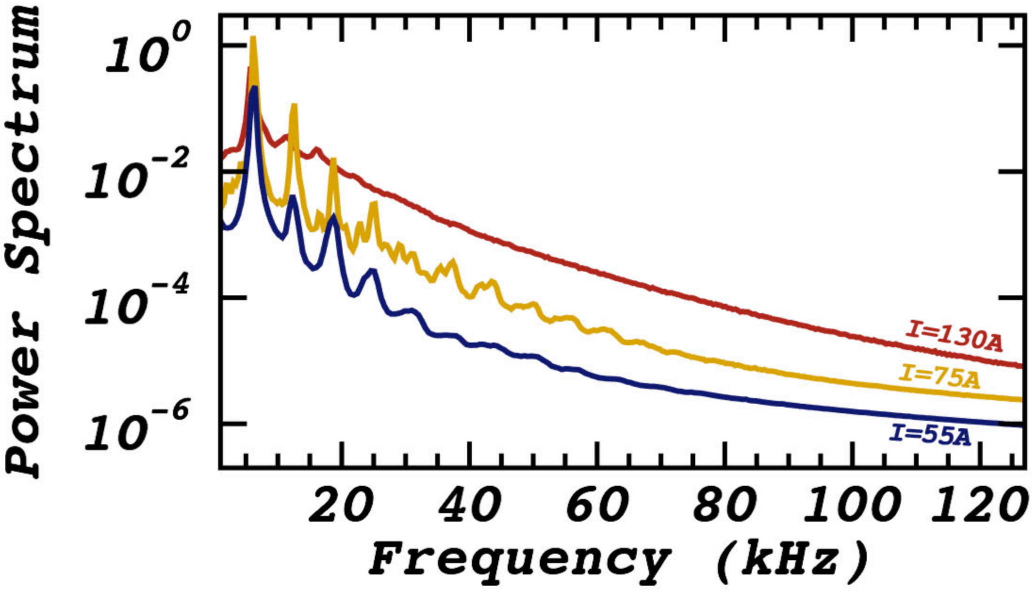

Figure 5.2 – The power spectrum associated with the three magnetic time traces shown in Figure 5.1. The spectrum is presented on a log-linear plot to show the rise in the underlying background as the current in the flux rope increases.

The wavelet transform of Figure 5.1a is plotted in Figure 5.3c. In this example, the signal exhibits strong, coherent rotation at f = 4 kHz. This frequency is shown to pervade the whole experiment. Also seen in the figure is the regular excitation of a broad range of frequencies. The interval between these events corresponds to the orbital rotation of the flux rope. As the flux rope moves in large and large circles around its stable position, the waveform recorded by the magnetic probe in the laboratory frame steepens, appearing either “pulse-like” or “ramp-like.” The sudden change in the magnetic signals from this type of waveform creates a broad range in frequencies. Similar behavior is visible at the turn on of the flux rope, where the sudden jump produces a range of frequencies.

A small portion of the magnetic signal and its corresponding temporal derivative is plotted in Figure 5.3a and Figure 5.3b. Also marked are the times at which there is an excitation of a broad range of frequencies. These times correspond to spikes in the $\dot{\mathbf{B}}$ signals. The shape of these peaks (or minimums) generates the form of the power spectrum in Figure 5.2. In this way, the frequencies observed in the spectrum are not waves but indicative of a single process – a characteristic pulse in $\dot{\mathbf{B}}$.

The temporal derivative of the magnetic field may be seen as a placeholder for a spatially varying electric field that is well correlated with the flux rope cross-section. This electric field can correspond to the electrostatic field associated with an electronegative flux rope (as seen in Chapter 3), or it can correspond to an induced electric field brought about the motion of the rope. The pulses then correspond to times when the flux rope passes the probe. This was evaluated by comparing I_{isat} and $\dot{\mathbf{B}}$ at the same location (x,y,z) = (5,0,870) cm outside the flux rope. A comparison between the two signals is plotted in Figure 5.4. The sign of the magnetic signal is reversed so that

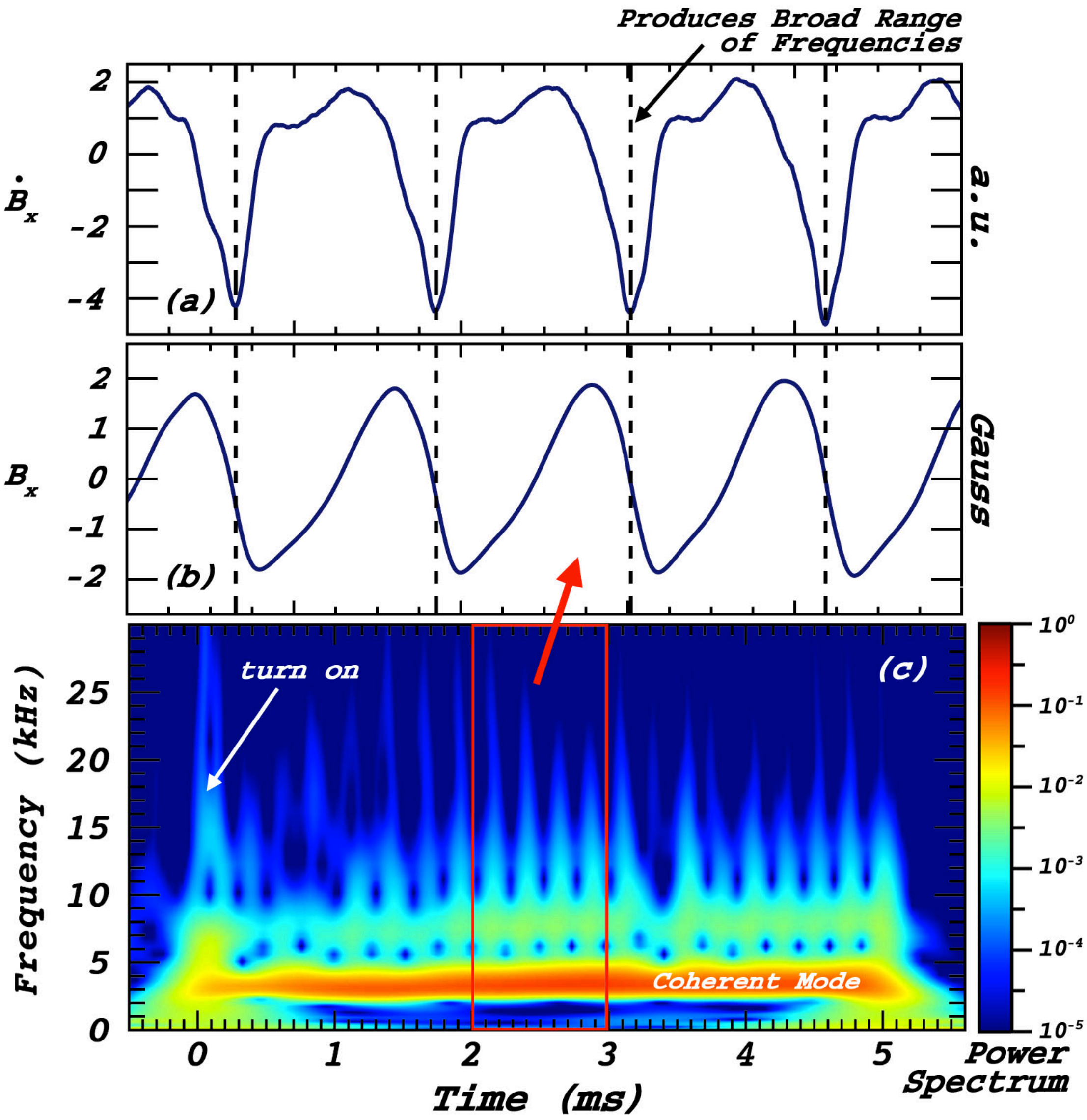

Figure 5.3 – (a) The time derivative of Figure 5.1a. The sharp spikes in the signal excite a broad range of frequencies. **(b)** A small portion of the magnetic signal from Figure 5.1a. **(c)** The wavelet transformation of Figure 5.1a. A flux rope exhibited a strong coherent mode at 4 kHz. As the flux rope passes the probe, there is the regular excitation of higher frequencies.

the signals can be easily compared. With this correction, the two signals are found to be well correlated (> 0.8). This is true at any position within the path of the flux rope. The width of each pulse corresponds to the time it takes for the flux rope to complete its transit passed the probe. This can be or approximated by $\Delta t = \frac{2a}{2\pi f_{FR} R_{Orbit}}$. Using f_{FR} = 4 kHz, a = 2.5 cm, and R_{Orbit} = 4 cm, the width of the pulse is predicted to be 50 μs, the width observed in Figure 5.4.

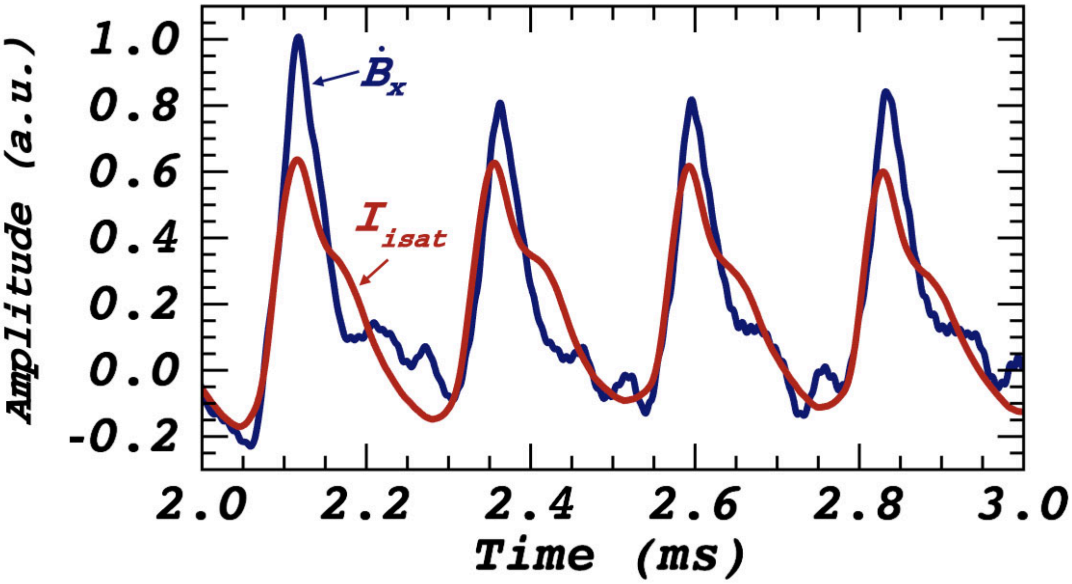

Figure 5.4 – A comparison between the I_{isat} and $\dot{\mathbf{B}}$ at the same location (x,y,z = 5,0,870 cm) for a flux rope I_{FR} = 55 A, B_z = 330 G, and L = 1100 cm. The signals are well correlated in time and space. In this way, $\dot{\mathbf{B}}$ reveal information about the position of the flux rope.

The shape of each pulse will then depend on the position of the probe, the distribution of current density within the flux rope, the orbital radius, and frequency of rotation. While this produces numerous different spectra within the experimental

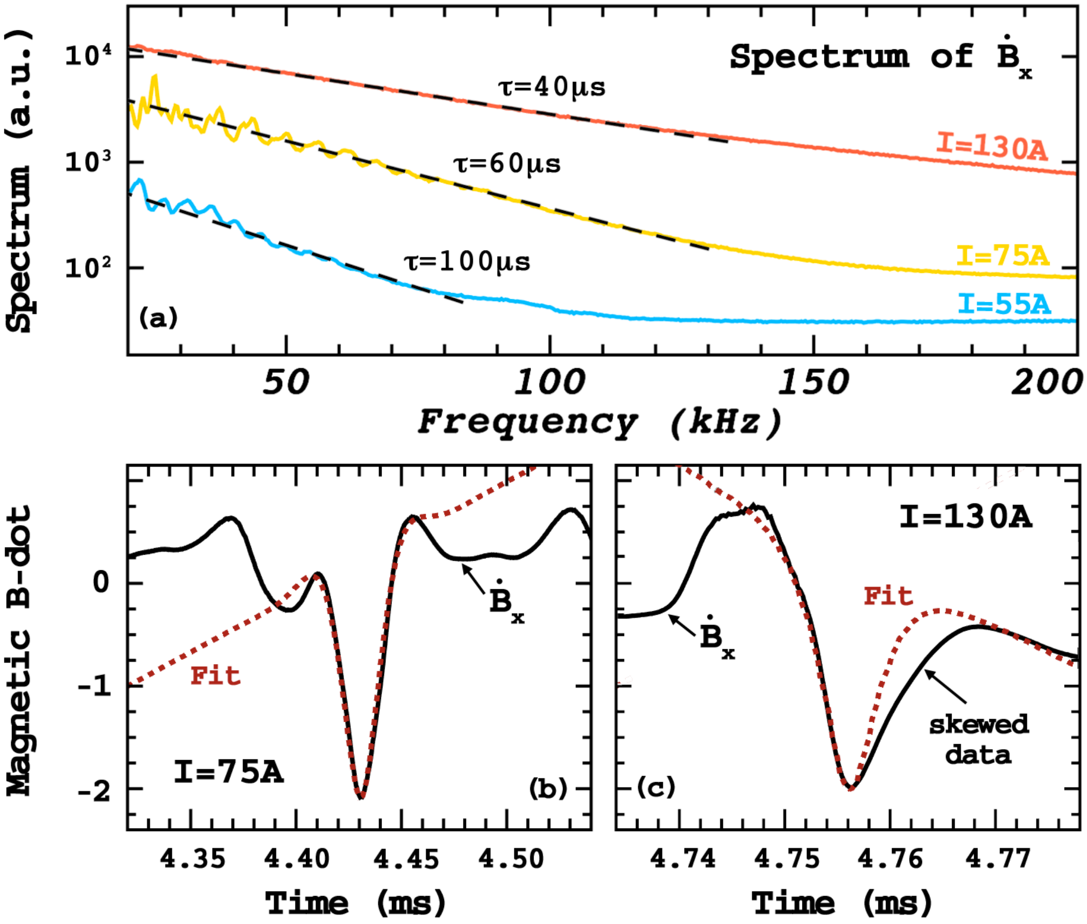

Figure 5.5 – (a) The spectrum of magnetic b-dot signals associated with the three time trace in Figure 5.1. The temporal derivate may be interpreted as a spatially varying electric field inside the flux rope. The data is fit to Eq. 5.1. The shape of the background is produced by the shape of characteristic pulses in the data. **(b)** The pulse shape was derived using the fit in (a) and is overlaid on the data for a flux rope of 75 A. **(c)** Using the fit in (a), the derived pulse from the spectrum is overlaid on the data for a flux rope of 130 A. The “skewness “ of the data is not preserved in the spectrum.

volume, the shape of each can be estimated by to an approximate form. Figure 5.5a plots the spectrum for $\dot{\mathbf{B}}$ signals that correspond to the three cases in Figure 5.2. Again, the results are plotted on a log-linear plot. On top of the data is shown a fit to the distribution:

$$\mathcal{F}\{\dot{\mathbf{B}}\} = \exp\left(-\tau|\omega|\right) \tag{5.1}$$

where A and τ are constants that can be calculated from the data. Eq. 5.1 is the spectrum associated with a pulse shape that is Lorentzian [Maggs 2012]. This characteristic exponential background is not uncommon in the LAPD and other experimental devices [Pace 2008, Hornung 2011] and can be indicative of a chaotic process [Gekelman 2014]. By numerically performing an inverse Fourier transform on the fits, the approximate form of the pulses are gained. Figure 5.5b and Figure 5.5c show the calculated pulse overlaid on the data. The two show good agreement when a line is added to the fit. In the case of 130 A, the pulse in the data is skewed. While the pulse shape will be retained in the Fourier transform, the "skewness" cannot be calculated from the spectrum.

5.3 – INCOHERENT SIGNALS

The preceding analysis was performed for a coherent flux rope – the exploration of a well-understood system before moving on to the incoherent one. As shown using the form of the spectrum (Figure 5.5), the pulses that are found in coherent signals are also found in the incoherent ones. It is reasonable to assume that if the translational motion of the flux rope causes the pulses in the coherent signals, then the same effect may produces the pulses in the incoherent signals. The pulses in the incoherent signals are shorter, more numerous, and occur at random intervals. To demonstrate this, Figure 5.6 shows a time trace of $\dot{\mathbf{B}}$ for a flux rope I_{FR} = 130 A. On the plot is marked the time difference between pulses.

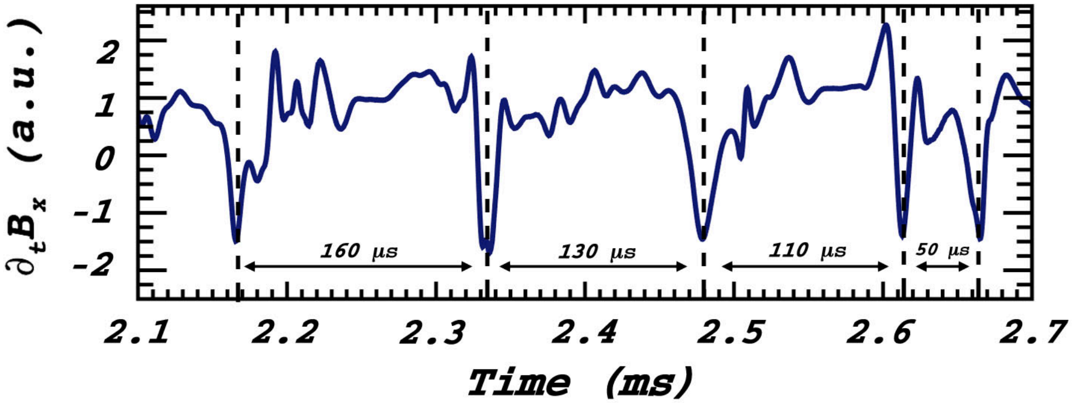

Figure 5.6 – The time derivative of Figure 5.1c (I_{FR} =130 A). The sharp spikes in the signal excite a board range of frequencies. These pulses are not evenly space; however, they do have a preferential direction.

It should be noted that the pulses in Figure 5.6 (just like those in Figure 5.3a) have a preferential (negative) polarity. This data was taken from a fixed probe. At this position (x,y,z = 5,0,870 cm), the preferred polarity of each pulse is negative. The preferred pulse direction, however, will change as a function of position. This can be demonstrated by counting the number and polarity of pulses at several locations in an x-y plane. A movable magnetic probe was moved to 1,600 location in an x-y cross-section at z = 1060 cm.

For a flux rope of I_{FR} = 130 A, the number and polarity of pulses were counted. This was done in the following manner: Using the fit to the background spectrum in Figure 5.5a, the pulse shape was obtained. A cross-correlation was performed between this pulse and each magnetic time trace acquired by the moveable probe. The pulse was slid through the data in time until good correlation (>0.9) was observed. The number, location, and polarity of each pulse were marked with +1 indicating a positive pulse and -1 indicating a negative pulse. This technique was utilized by [Pace 2009] to find Lorentizian pulses associated with a small current filament.

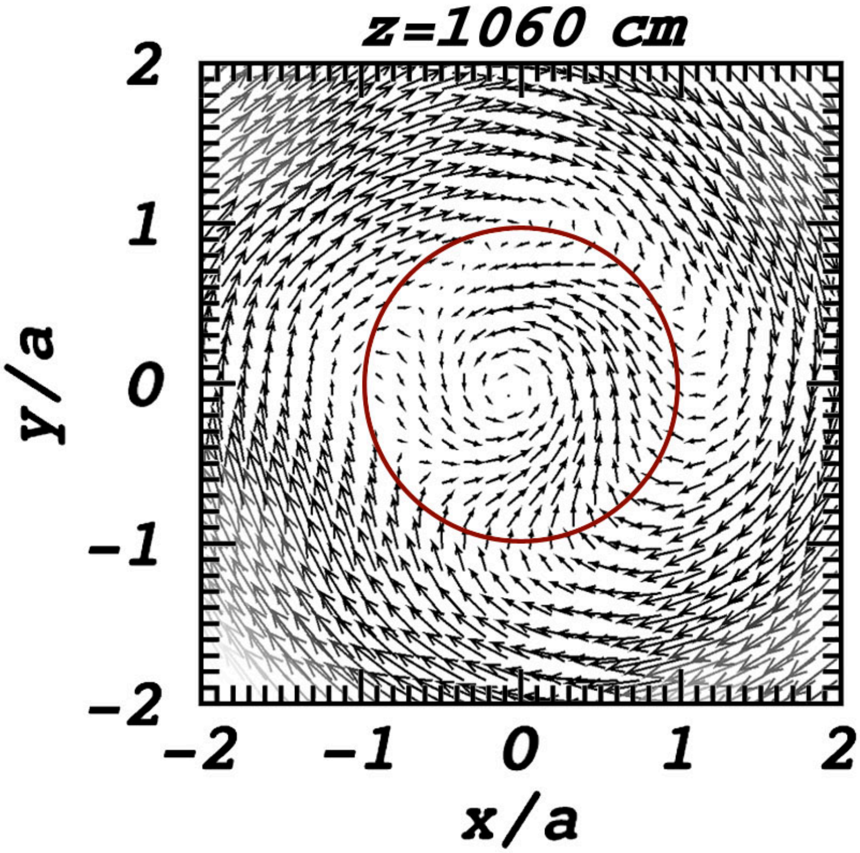

Figure 5.7 – The average number of pulses in $\dot{B}_x$ and $\dot{B}_y$ at z = 1060 cm. The figure is presented as a vector field with the number of pulses in $\dot{B}_x$ being the x-component of the vectore and the number of pulses in $\dot{B}_y$ being the y-component of the vector. Negative values in reflect negative pulses on average while positive values indicate positive pulses on average.

The results are plotted in Figure 5.7. The analysis was performed on both $\dot{\mathrm{B}}_x$ and $\dot{\mathrm{B}}_y$ so that the number and polarity of pulses could be shown as a vector field. On average the polarity of the pulses resembles the structure of a shear Alfvén wave from a narrow current filament [Gekelman 2011]. This is related to the motion of the flux rope whose system of equations is related to that of an Alfvén wave. The perpendicular wave number $k_\perp$ for the structure can be approximated using the radius of the flux rope ($k_\perp = \frac{1}{2a}$ cm^{-1}). A circle is drawn in the figure to show the equilibrium position of the flux rope.

5.4 – COMPLEXITY-ENTROPY MAPPING

Recent advances in statistical analysis have yielded a technique through which experimenters can parse the underlying physical processes of their system. By creating a distribution that quantifies the frequency of occurrence of certain patterns in a digitized time traces, a distinction is made between systems that are smooth and deterministic and others that are stochastic or chaotic [Bandt 2002, Rosso 2007]. In the LAPD, this technique has already been utilized on a system of two magnetic flux ropes embedded in an argon plasma [Gekelman 2014]. In this experiment, the system exhibited chaotic time traces. However, the analysis is sensitive to all sources of fluctuations – including motion of the ropes, interactions between two ropes, drift waves, and maser activity from the BaO source. In this chapter, we repeat the analysis for a single flux rope to eliminate second order effects.

The analysis begins by computing the Bandt-Pompe (BP) probability distribution [Bandt 2002]. To compute the distribution, a collection of digitized time traces is assembled. An "embedding space" of dimension d is created by partitioning each time trace into numerous sets of d consecutive points, or "d-tuples." Each individual set is then ordered according to the amplitude of the elements within the set, and the order by which they occurred in the data is marked.

For example, a tuple of size $d = 4$ is given by A = {9, 6, 3, 12}. These are arbitrary values. Ordering them from largest to smallest, the order by which they occurred originally may be given by t = {4, 1, 2, 3}. In a time series with N points, there is a total of (N-d+1) d-tuples that can be generated. For each embedding dimension d, there are d! possible permutations (or in the example: possible orderings of t). From these orderings, the relative frequency or the probability a particular ordering of type π is given by

$$p_j(\pi) = \frac{\#\left\{t_j \middle| t_j \leq T - n, \left(x_{t_{j+1}}, \dots x_{t_{j+n}}\right) has\ permutation\ type\ \pi\right\}}{T - n + 1} \qquad (5.2)$$

Equation 5.2 is the Bandt-Pompe (BP) probability distribution [Bandt 2002]. Once the BP probability distribution is calculated, the form of the distribution can be mapped onto a plane. This is plane is known as a complexity-entropy diagram (C-H diagram) [Rosso 2007]. In other words, a single time trace of recorded data is reduced to a set of two elements, $\{h_i, c_i\}$. The position of this set on the plane can represents the type of physical process in the system. The diagram can discern between different degrees of periodicity associated with routes to chaos and can distinguish stochastic noise and chaos.

Given a probability distribution $p = \{\pi_1, \pi_2, \dots \pi_d\}$, the entropy element of the diagram, called the Shannon entropy S, is calculated by:

$$S(P) = -\sum_{j}^{N} p_j(\pi)\ln\left(p_j(\pi)\right) \tag{5.3}$$

The normalized Shannon entropy H is computed by dividing S by the maximum entropy according to:

$$h_i = \frac{S(P)}{\ln(d!)} \tag{5.4}$$

Therefore, the values of h_i fall between 0 and 1.

Since BP probabilities with the same entropy do not necessarily have the same physical significance, to distinguish between processes that are chaotic and processes that are more stochastic, the complexity of a signal is defined as:

$$c_i = -2\frac{S\left(\frac{P+P_e}{2}\right) - \frac{1}{2}S(P) - \frac{1}{2}S(P_e)}{\frac{d!+1}{d!}\ln(d!+1) - 2\ln(2d!) + \ln(d!)}h_i \tag{5.5}$$

Where P_e is the maximum entropy state for which every member of the probability distribution have the same value $1/d!$. While c_i and h_i can be used as independent parameters of data analysis, there is a maximum and minimum complexity value for a given value of h_i [Martin 2006].

Because the analysis relies on the partitioning of discretized sets of data, it is sensitive to the digitization rate at which the data was collected [Maggs 2015]. In the series of experiments presented here, the data was collected at a rate of 3 MHz. However, the physics associated with the motion of the flux rope is on the order of 10 kHz. If the analysis was perform on a time whose points are separated by dt = 3.2x10^{-7} s, then the resulting probabilistic distribution would appear either stochastic (only sampling the high frequency noise) or periodic (if a low pass filter was applied to the signals before digitization). Therefore, to better capture the physical process associated with the motion of the rope, the data was subsampled every 10 points in the data.

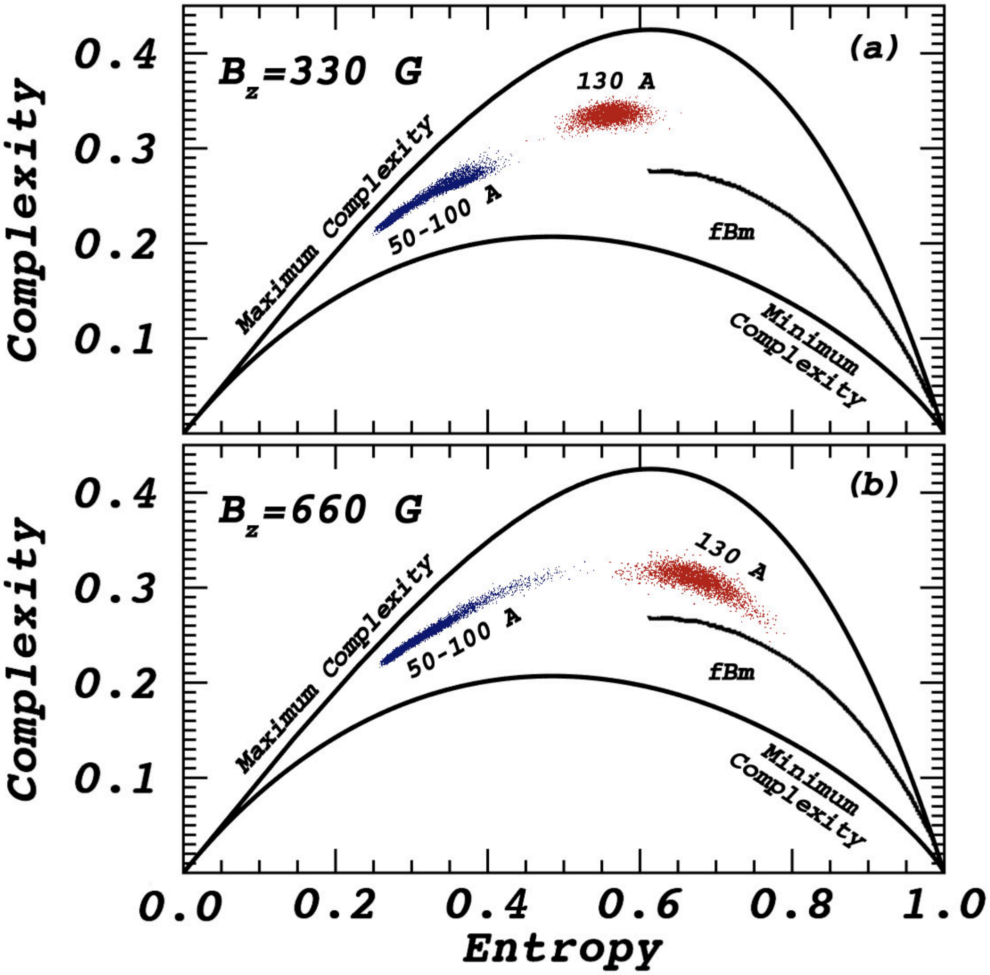

Figure 5.8 – The Complex-Entropy Plane for a single flux rope at varying currents. Each dot represents the reduction of a single magnetic time trace onto the plane. Between 50A and 100A, the flux rope are kink unstable for a background magnetic field of both **(a)** 330 G and **(b)** 660 G. For this range of currents, the flux rope exhibits strong coherent rotation, indicated by low entropy signals. The points for this range of current is indistinguishable on the plane. For 130 A, the signals transition toward chaos. This is indicated by their position above Fractional Brownian Motion (fBm).

Complexity-entropy analysis was performed on data collected from a fixed probe (x,y,z) = (5,0,870) cm for flux rope currents between 50 A and 130 A. Two background magnetic fields were considered: one at 330 G and another at 660 G. Over 35,000 time traces were considered, and an embedding space of $d = 5$ was used. The results are plotted in Figure 5.8 and each dot represents a single analyzed time trace. Between 50 A and 100 A, the flux rope exhibits coherent rotation for both a flux rope at 330 G and another at 660 G. This is reflected in the C-H plane, presented on the plane at low entropy. This is a check on the validity of the analysis.

At 130 A, the collection of points shifts in the C-H plane. This indicates a transition in the behavior of the flux rope. There is an increase in both entropy and complexity. The collection of points for 330 G and 660 G both lie above the line which indicates Fractional Brownian Motion (fbm). This line serves as a separator between chaos at high complexity and stochastitity at low complexity [Mandelbrot 1968]. Both signals at 330 G and 660 G may be considered chaotic. However, the signals at 660 G represent motion with high entropy, appearing more stochastic, than those at 330 G.

CHAPTER 6 – *CANONICAL HELICITY*

6.1 – INTRODUCTION

In astrophysics, magnetic flux ropes are modeled using the assumption of a perfectly conducting fluid. Under this condition, the motion of the fluid is bound by the conservation of the quantity:

$$H_M = \int \boldsymbol{A} \cdot \boldsymbol{B} \, dV \tag{6.1}$$

Here, $\boldsymbol{A}$ is the vector potential; $\boldsymbol{B}$ is the magnetic field ($\boldsymbol{B} = \boldsymbol{\nabla} \times \boldsymbol{A}$); and H_M is the magnetic helicity. Magnetic helicity has geometric significance. Eq. 6.1 is a generalized expression for a topological linking number, describing the linkage of magnetic flux tubes. Equivalently, the expression characterizes magnetic twist and writhe. This has been addressed by [Moffat 1978], [Pfister and Gekelman 1991], [Berger 1999], [Bellan 2000], and [Blackman 2015] – among others.

In this experimental work, however, flux ropes cannot be modeled using the MHD approximation - the field lines are not frozen to the flow, large pressure gradients exist, and the electric field has a dominating electrostatic component. In addition, plasma resistivity on the order of or larger than its classical value can have a great effect on the motion of the flux rope system itself. This limits the use of magnetic helicity as a constant of motion.

While its use is constrained for the experiment as a whole, magnetic helicity is still a valuable quantity during events of magnetic reconnection because its non-conservation can be connected to dissipation in the plasma. In this chapter, we examine magnetic helicity for two-flux ropes. The flux rope are driven kink unstable so that they thrash about and periodically collide, producing magnetic reconnection. Magnetic helicity and its two fluid counterpart, canonical helicity, are evaluated during a reconnection event. We conclude that the dissipation of relative helicity in the flux ropes is balanced by the electric field generated during reconnection.

6.2 – TWO FLUX ROPE INTERACTION

This chapter focuses on a system of two magnetic flux ropes (a = 3.75 cm, L = 1100 cm, B_z = 330 G, V_D = 120 V, I_{FR} = 300 A each). The flux ropes are driven unstable, each going unstable at $I_{KS}/2$. In addition to twisting about each other due to $\mathbf{J}\times\mathbf{B}$ forces, each flux rope exhibits coherent rotation about its equilibrium position. Unlike a single flux rope, the path of each flux rope does not take the form of a perfect circle. Instead, the orbit becomes elongated as the two flux ropes interact, writhe, and merge close to the anode. The merging process of the two flux ropes was demonstrated in Chapter 3.

The consistency of coherent motion (Chapter 4) produces repeatable signals throughout the system. This repeatability is utilized to reconstruct quantities ($\mathbf{B}$, $\mathbf{E}$, $\mathbf{v}$, etc.) point for point over the course of a few weeks of data acquisition. Several probe diagnostics were used to generate fully three-dimensional datasets of relevant quantities

– including the magnetic field (**B**), vector potential (**A)**, current density (**J)**, electric field (**E)**, ion flow (**v**), and plasma pressure (P_e).

The two flux ropes are three times hotter (T_e = 12 eV) and five times denser (n_{rope} = $5x10^{12}$ cm^{-3}) than the background plasma with a current density as high as 5 A/cm^2. The perpendicular pressure force points radially outward from the center of each flux rope and is balanced by the inward forces of **J**x**B**. The electrostatic field points inward toward the center of each flux rope as the ropes are electrostatically negative with respect to the plasma background. This electrostatic field generates **E**x**B** flows that spiral around the two flux ropes. In the parallel direction, an electrostatic field, produced by the discharge voltage, is responsible for electron streaming along the field to form the flux ropes. Similarly, axial pressure gradients lead to ions flows along the field. These quantities are used in the calculation of canonical helicity.

6.3 – IDENTIFICATION OF MAGNETIC RECONNECTION

To identify when and where magnetic reconnection occurs, a squashing factor, or q-value is employed. A q-value is a topological description of magnetic field line divergence [Priest 1995, Titov 2002, Démoulin 2006]. Using the fully three-dimensional magnetic dataset, hundreds of field lines are seeded and fixed at z = 0 m. Then, using spline coefficients calculated from the data, the field lines are followed axially until their x-y locations (denoted here as $\mathbb{X}(x, y, t), \mathbb{Y}(x, y, t)$) are determined at z = 11 m. With the end positions of these field lines, q-values are calculated:

$$q = \frac{\left(\frac{\partial \mathbb{X}}{\partial \mathrm{x}}\right)^2 + \left(\frac{\partial \mathbb{X}}{\partial \mathrm{y}}\right)^2 + \left(\frac{\partial \mathbb{Y}}{\partial \mathrm{x}}\right)^2 + \left(\frac{\partial \mathbb{Y}}{\partial \mathrm{y}}\right)^2}{|\mathrm{B_z}(\mathrm{z} = 0\ \mathrm{m})/\mathrm{B_z}(\mathrm{z} = 11\ \mathrm{m})|} \tag{6.2}$$

Eq. 6.2 is a mathematical projection of the field-line topology onto a plane, having a unitless lower bound of 2.0. When q becomes large on multiple, adjacent field lines, the collection of these field lines is called a Quasi-Separatrix Layer, or QSL.

Figure 6.1 shows a surface of constant q using field line data and Eq. 6.2. A direct calculation of q is shown in Figure 6.1a at a time when q is large (t = 5.67 ms). Each field line is reduced to a single scalar, and q is therefore plotted in a plane by definition. A collection of large q-values snakes between the two ropes, forming a QSL. A three-dimensional representation of the QSL is presented in the Figure 6.1b. The flux ropes are born at the mask then twist around each other as they develop axially. The QSL in the figure represents the collection of field lines whose q values are greater than 200. The structure manifests between the flux ropes over the length of the flux ropes.

Previous flux rope experiments on the LAPD have demonstrated that a QSL forms periodically, snaking in between two flux ropes that at repeatedly collide and merge [Lawrence 2009, Gekelman 2016]. During the periodic formation of the QSL, neighboring field lines diverge as they pass though the layer, suggesting a reconnection event. In this experiment, a QSL forms every 200 μs (or at a rate of 5.1 kHz) as long as the flux rope are driven kink unstable.

To further demonstrate that this topological quantity is linked to magnetic reconnection, the amount of energy dissipation within the QSL was estimated by

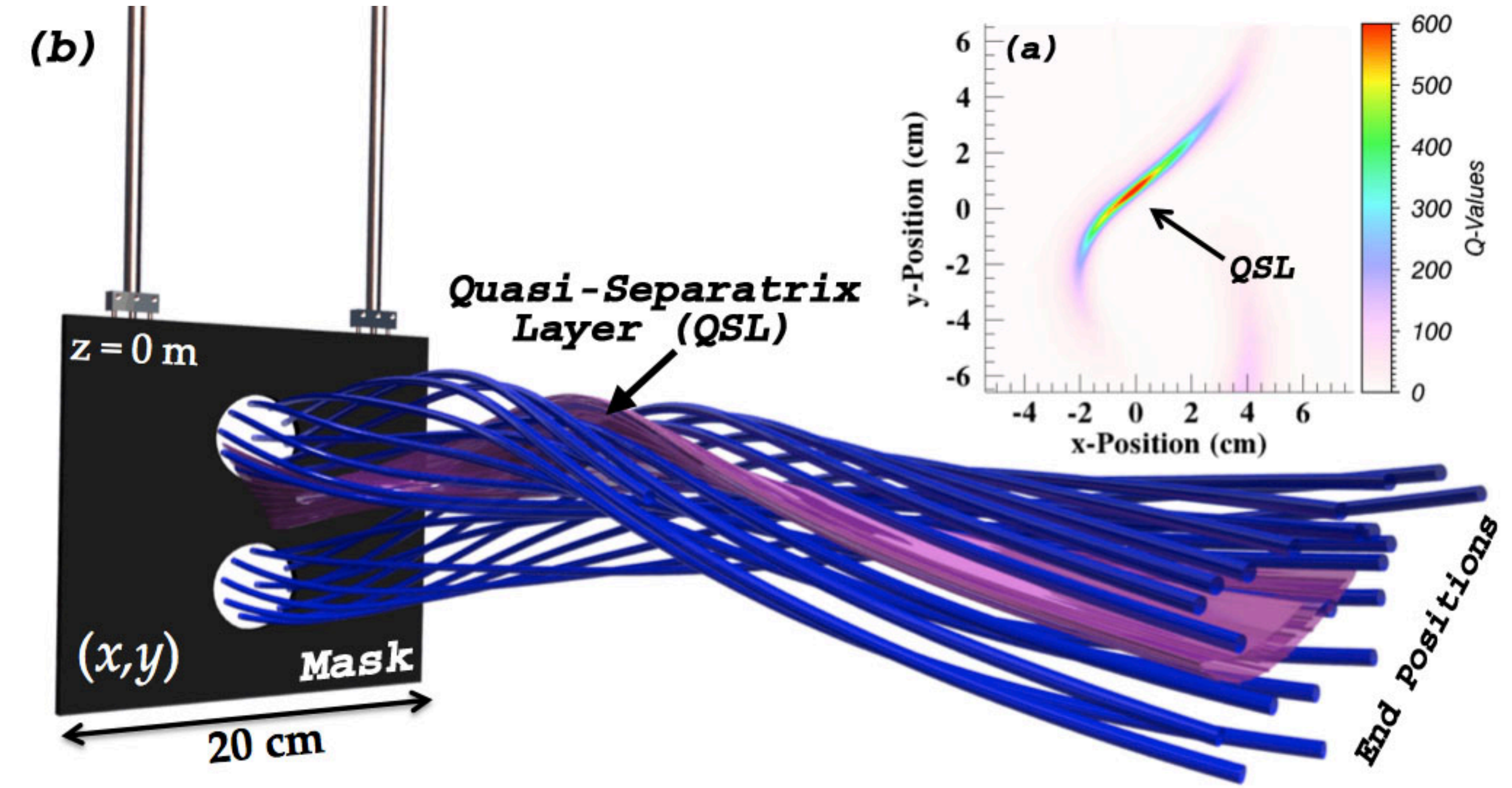

Figure 6.1 – **(a)** A plot of the squashing factor q at t = 5.6 ms, during a reconnection event. A collection of field lines exhibit large q-values compared to its surroundings. These collection of field lines are called a quasi-separatrix layer. (QSL **(b)** A three-dimensional representation of the QSL. During a reconnection event, a QSL forms between the flux ropes. Magnetic helicity will be considered inside this volume.

integrating $\int_{QSL}(\boldsymbol{E}\cdot\boldsymbol{J})dV$. The dissipation of energy inside the QSL peaks at approximately 100 Watts, a small fraction of the 100 kW used in the formation of the ropes. Over the formation and diminution of the QSL, the total change in energy is -2 *mJ*, which corresponds to 0.2 Gauss of annihilated magnetic energy. This number was corroborated with the measurement of magnetic energy density in side the same region.

6.4 – MEASUREMENTS OF RELATIVE MAGNETIC HELICITY

Magnetic helicity is only preserved within magnetic flux surfaces [Taylor 1974]. When the volume integral of $\boldsymbol{A}\cdot\boldsymbol{B}$ is not enclosed by a magnetic flux surface, there is no absolute measure of magnetic helicity. For a straight flux rope enclosed in a cylindrical volume, the magnetic field line do not close inside the experimental volume. Since the magnetic field was not measured past the walls of the experimental device, Eq. 6.1 cannot be used to evaluate H_M. To solve this problem, relative magnetic helicity is utilized instead:

$$K_M = \int_V (\boldsymbol{A}+\boldsymbol{A}')\cdot(\boldsymbol{B}-\boldsymbol{B}')dV \tag{6.3}$$

$\boldsymbol{A}'$ and $\boldsymbol{B}'$ are reference fields such that $\boldsymbol{B}' = \nabla\times \boldsymbol{A}'$. K_M is the relative magnetic helicity, a concept developed by [Berger and Field 1984] , [Jensen and Chu 1984], [Finn and Antonsen 1985], and others. For a cylindrical flux rope, a convenient reference field is $\boldsymbol{B}' = \boldsymbol{B_0}$, the background field which penetrates the ends of the volume and a constant in space and time [Hu and Dasgupta 2005].

We focus on the changes of relative magnetic helicity inside the QSL. Inside this layer, the field lines are undergoing the most rapid change, and therefore helicity is of interest and may be conserved. We focus on the temporal derivative of relative magnetic helicity because it takes a more physical meaning then a direct calculation of K_M inside the volume.

When the flux ropes collide and reconnect, a small amount of magnetic field is annihilated. This produces an electric field, which can be identified in the data and used to locate times and regions of reconnection. This induced electric field is linked to changes in magnetic helicity, and these changes can be broken down into two integrals [Berger and Field 1984]:

$$\frac{\partial K_M}{\partial t} = -2\int_{\mathrm{V}} \left(-\frac{d\boldsymbol{A}}{dt}\cdot\mathbf{B}\right)\mathrm{dV} - \int_{V} \left(-\frac{d\boldsymbol{A}}{dt}\times(\boldsymbol{A}+\boldsymbol{A}')\right)\cdot d\boldsymbol{S} \tag{6.4}$$

In Eq. 6.4, the volume integral is a source (or dissipative) term of magnetic helicity while the surface integral represents its transport. Each term in Eq. 6.4 was evaluated.

To demonstrate the spatial dependence of helicity dissipation, $-d\boldsymbol{A}/dt$ is integrated along the field lines. Mathematically, this is expressed as a dissipation:

$$D = -2\int_{\text{Field Line}} \left(-\frac{d\boldsymbol{A}}{dt}\cdot\mathbf{B}\right)dl \tag{6.5}$$

D, when viewed in a plane, spirals around the two flux ropes (Figure 6.2). This is the result of the flux rope’s elliptical motion in the x-y plane. At the time of formation of the QSL, a tendril of dissipation reaches out and snakes between the two flux ropes. This dissipation is due to reconnection and is temporally and spatially correlated with the

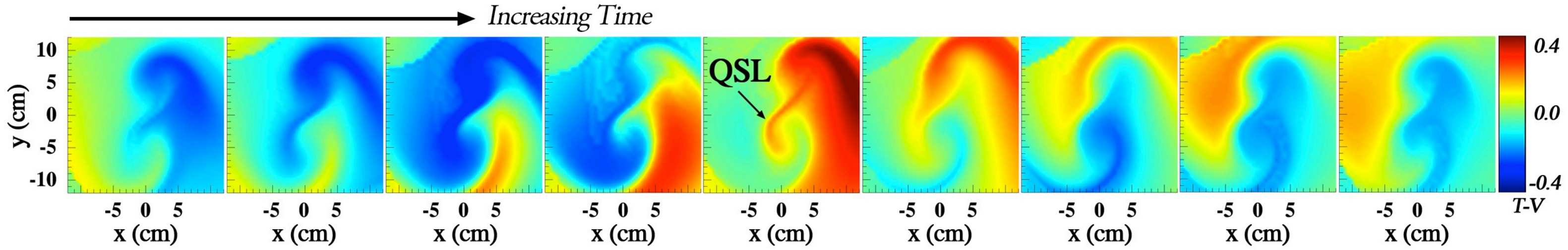

Figure 6.2 - D, the dissipation (red on the color bar) of magnetic helicity, as defined in Eq. 6.5, plotted for one period of flux rope rotation (t=5.47-5.87 ms and dt = 50 us). The center frame indicates the time at which the flux ropes collide and a QSL forms. Spatially correlated with the QSL is a tendril of magnetic helicity dissipation, which snakes between the flux ropes.

QSL. The remaining dissipation is from the resistive currents.

Eq. 6.5 is related to the quasipotential, Ξ. This quantity is computed by integrating along field lines:

$$\Xi = \int_{\text{Field Line}} \mathbf{E} \cdot d\boldsymbol{l} \tag{6.6}$$

While Eq. 6.5 included only the induced electric field, Eq. 6.6 is the total electric field. This term will be added below. In terms of magnetic reconnection, Eq. 6.6 is a direct measurement of the global nonlinear reconnection rate [Hesse 2005]. Recent simulations suggest that magnetic field lines passing through the QSL are associated with non-zero values in Ξ [Wendel 2013]. This is what is observed here. In this chapter, it is used in the context of magnetic helicity.

An additional benefit of presenting D is that it defines regions of interest that can be isolated from the rest of the plasma. Changes in helicity can be used to estimate plasma resistivity [Bellan 2000] according to

$$\langle \eta \rangle_{\text{QSL}} = \int_{\text{QSL}} \left(-\frac{d\boldsymbol{A}}{dt} \cdot \mathbf{B} \right) dV \Big/ \int_{\text{QSL}} (\mathbf{J} \cdot \mathbf{B})\, dV \tag{6.7}$$

Instead of using the dissipation of helicity to estimate resistivity over the entire experimental volume, we isolate the volume of field lines located within the QSL. These are the field lines potentially undergoing the most change. Eq. 6.7 yields a lower bound resistivity of 1.7×10^{-5} Ω-m due only to the annihilated magnetic field. This is a resistivity approximately equal to the classical resistivity for 10 eV electrons.

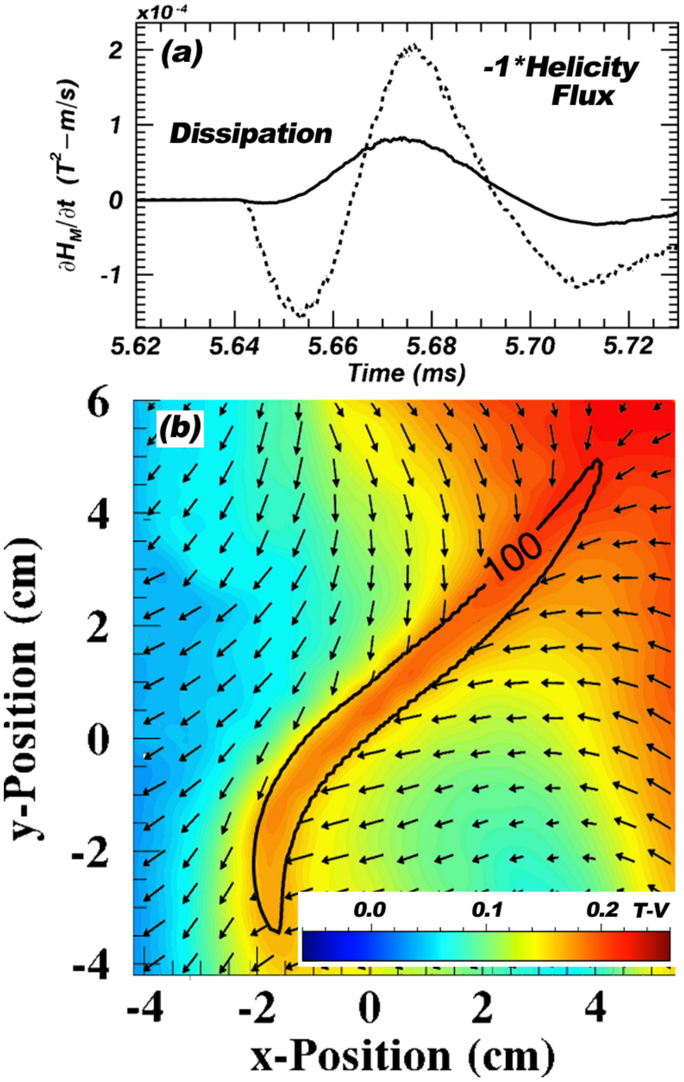

Figure 6.3 – **(a)** The dissipation and influx of magnetic helicity (Eq. 6.4) into the QSL (q=100). The addition of the two traces yields the time derivative of magnetic helicity, $\frac{\partial K_M}{\partial t}$, during a collision between the two flux ropes. **(b)** The color map represents D (Eq. 6.5) calculated at t=5.67 ms. The arrows represent T (Eq. 6.8) calculated at t=5.67 ms.

Equation 6.4 was evaluated using the volume of the QSL as the region of interest. The volume integral and the surface integral of Eq. 6.4 were calculated separately and are plotted in Figure 6.3. The solid curve in Figure 6.3a is the resistive dissipation of magnetic helicity inside the QSL. The dashed curve in Figure 6.3a is the transport of magnetic helicity into or out of the QSL. The terms do not balance. While magnetic helicity is moving into the QSL as the two ropes collide, it is not enough to supplant the magnetic helicity that is dissipated. A 2-D representation of this process is plotted in Figure 6.3b. This figure shows D at the time of peak dissipation. The contour of q = 100 is drawn to show spatial correlation with D. The arrows represent helicity transport into the QSL, calculated using:

$$\boldsymbol{T} = -\int_{Field\ Line}\left(-\frac{d\boldsymbol{A}}{dt}\times(\boldsymbol{A}+\boldsymbol{A}')\right)dl \tag{6.8}$$

Because the dissipation of helicity does not balance helicity flux, this suggests a missing term(s) in Eq. 6.7 or Eq. 6.8.

6.5 – CANONICAL HELICITY

Up to this point, helicity has been viewed in an MHD sense. In this description, the plasma was treated as a single flux with no electrostatic fields or pressure gradients. This is certainly not the case for the experimental system – as shown in Chapter 3. Therefore, the former picture is an insufficient description. Instead, an extended fluid picture involving heretofore ignored quantities is used. This is done by untilizing canonical helicity, as introduced by [You 2012]. Canonical helicity is a fluid counterpart to magnetic helicity, and its conservation has been proposed in lieu of the MHD model. The use of this new model is beneficial because it includes the effect of electrostatic potential, temperature, and flow on magnetic helicity.

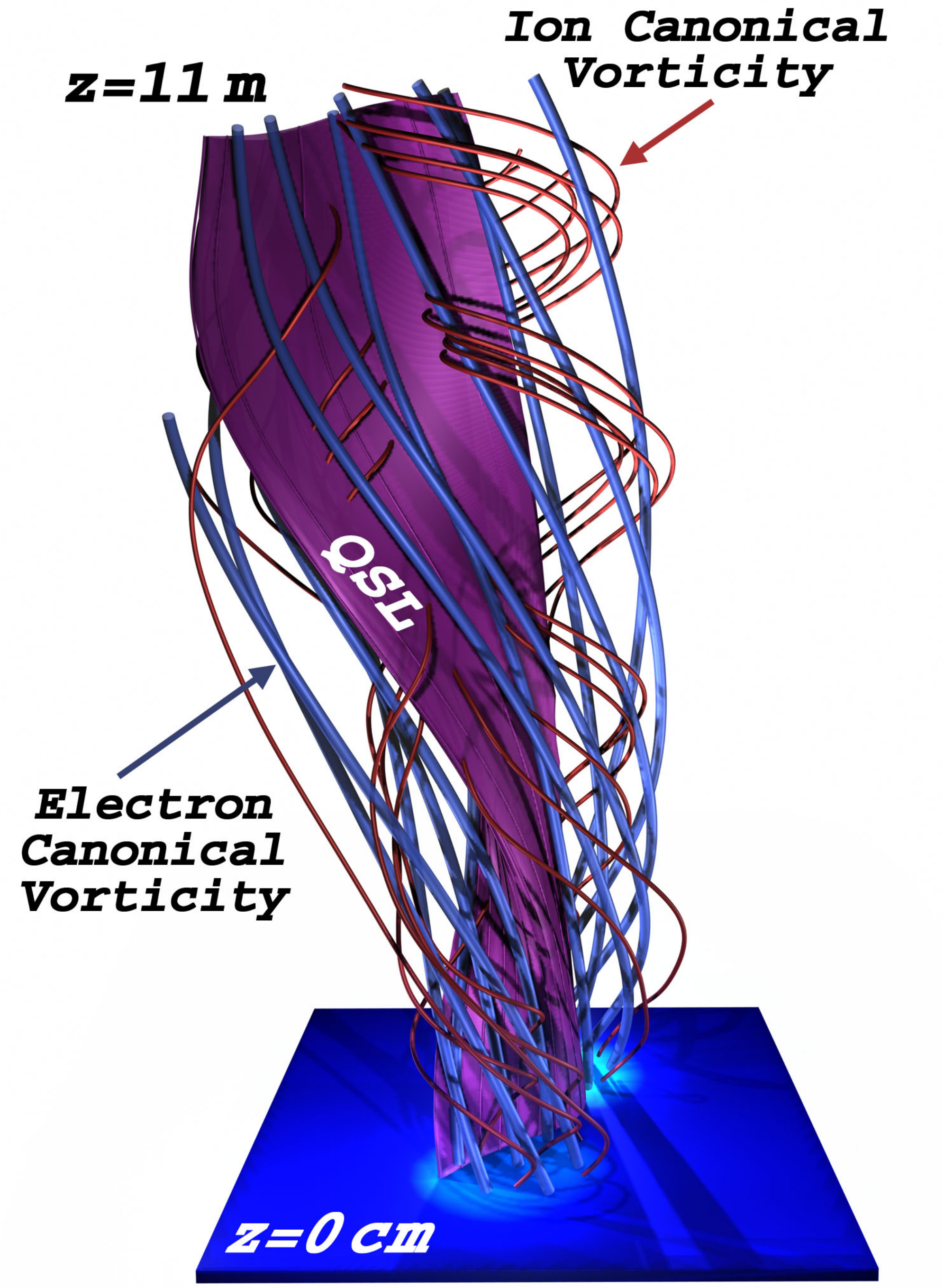

Figure 6.4 – A three-dimensional representation of (electron canonical vorticity, blue) and (ion canonical vorticity, red) at t=5.67. The two fluid approach to helicity, canonical helicity is defined as the self-linkage of these quantities.

Calculations of canonical helicity begin with the canonical momentum of a fluid element in the plasma, given by $\boldsymbol{P_q} = m_q\mathbf{v_q} + q\boldsymbol{A}$. Here, m_q and q are the mass and charge associated with a species, q, and $\mathbf{v_q}$ represents the fluid flow of that species. Generalized vorticity is introduced as the curl of canonical momentum ($\boldsymbol{\Omega}_q = \boldsymbol{\nabla}\times\boldsymbol{P}_q$). By integrating $\boldsymbol{\Omega}_q \cdot \boldsymbol{P}_q$ over the entire volume, canonical helicity is derived.

Canonical helicity is a generalized expression for a topological linking number that describes the self-linkage of canonical vorticity, $\boldsymbol{\Omega}_q$**.** The ion and electron species each have their own canonical vorticity. “Field lines” of $\boldsymbol{\Omega}_e$ and $\boldsymbol{\Omega}_i$ are shown in Figure 6.4. Because the mass of the electron is negligible, $\boldsymbol{\Omega}_e$ is equivalent to the magnetic field. One the other hand, $\boldsymbol{\Omega}_i$ includes the addition of vorticity to the magnetic field**.** Therefore, the self-linkage of $\boldsymbol{\Omega}_e$ and $\boldsymbol{\Omega}_i$ differs from one another. Each will be considered separately.

To ensure that canonical helicity is gauge invariant, an arbitrary reference field is added to each physical quantity ($\boldsymbol{B}, \boldsymbol{A}, \boldsymbol{E}$ ...) that penetrates the surface surrounding the experimental volume as in Eq. 6.2. This reference field $\boldsymbol{X'}$ satisfies the criteria $\boldsymbol{X} \cdot \nabla S = \boldsymbol{X'} \cdot \nabla S$, where $\boldsymbol{X}$ is a stand-in for any experimental quantity and *S* is the surface of the experimental volume. Using this reference field, relative canonical helicity is defined in the same manner as relative magnetic helicity:

$$\mathrm{K}_q = \int_{\mathrm{V}} \left(\boldsymbol{\Omega}_q - \boldsymbol{\Omega'}_q\right) \cdot \left(\boldsymbol{P}_q + \boldsymbol{P'}_q\right) dV \tag{6.9}$$

As before, temporal changes in K_q are broken down into a volume integral and a surface integral. This not only includes the induced electric fields but also temperature, density, plasma potential, and flows.

$$\frac{\mathrm{dK}_q}{\mathrm{dt}} = -\int_{QSL} \left(\mathbb{E}_{q+} \cdot \boldsymbol{\Omega}_{q-} + \mathbb{E}_{q-} \cdot \boldsymbol{\Omega}_{q+}\right) d\mathrm{V} - \int_{QSL} \left(h_{q-}\boldsymbol{\Omega}_{q+} + \boldsymbol{P}_{q-} \times \frac{\boldsymbol{\partial P}_{q+}}{\boldsymbol{\partial t}}\right) \cdot d\boldsymbol{S} \qquad (6.11)$$

The volume integral is the generalized source and sink of canonical helicity, where $\mathbb{E}_q = -\boldsymbol{\nabla} h_q - \frac{\boldsymbol{\partial P}_q}{\boldsymbol{\partial t}}$ and $h_q = q\phi + 1/2\, m_q \mathbf{v}_q^2 + \int dP_q/n$ for a single species q [You 2015]. The first term in the surface integral is the generalized helicity injection from an electrostatic potential. And the second term in the surface integral is the AC injection of canonical helicity from the changing vector potential $\partial\mathbf{A}/\partial t$.

Considering, first, electron canonical helicity: the dissipative term ($\mathbb{E}_e \cdot \boldsymbol{\Omega}_e$) is found to be spatially and temporally correlated with the QSL. This region of helicity decay snakes through the center of the two flux ropes as they begin to collide. The dissipation of helicity within this region is three times greater than the pure MHD case. By defining the region of interest to be within the QSL, the contribution to the resistivity from each term in $\mathbb{E}_e$ is calculated. The contribution from the induced electric field is 1.7e-5 Ω-m. The contribution from the electrostatic term is 1.0e-5 Ω-m, and the contribution from the pressure term is 1.8e-5 Ω-m. When added together, the volume-averaged resistivity within the QSL becomes approximately three to five times the classical value. Figure 6.5 plots a comparison between helicity dissipation due to the different terms in $\mathbb{E}_e$. Each term is separately coincident with the QSL. Adding the graphs yields the total amount of canonical helicity dissipated within the QSL.

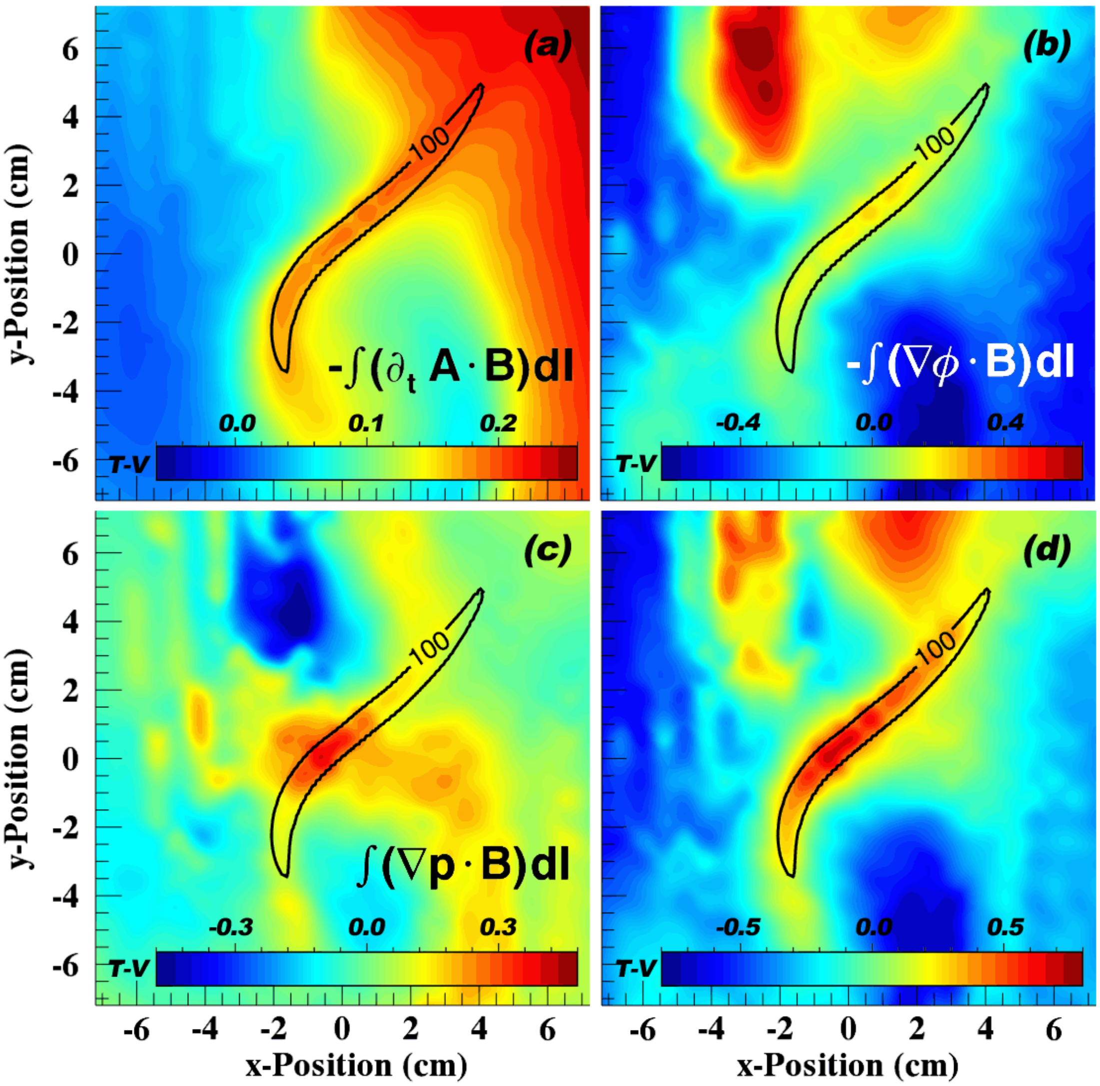

Figure 6.5 – A comparison between the amount of electron canonical helicity dissipation inside the QSL due to the terms in $\mathbb{E}_e$: **(a)** from the induced electric field, **(b)** from the electrostatic field, **(c)** from the pressure gradients. The total is plotted in **(d)**.

The arrows in Figure 6.6b represent the influx of electron canonical helicity into the QSL. Visualizing the data in this manor is a useful technique to demonstrate that as K_e is being dissipated within the QSL (represented by the color bar in Figure 6.6b), it is also being replaced by an influx of helicity across the boundary. Both the total

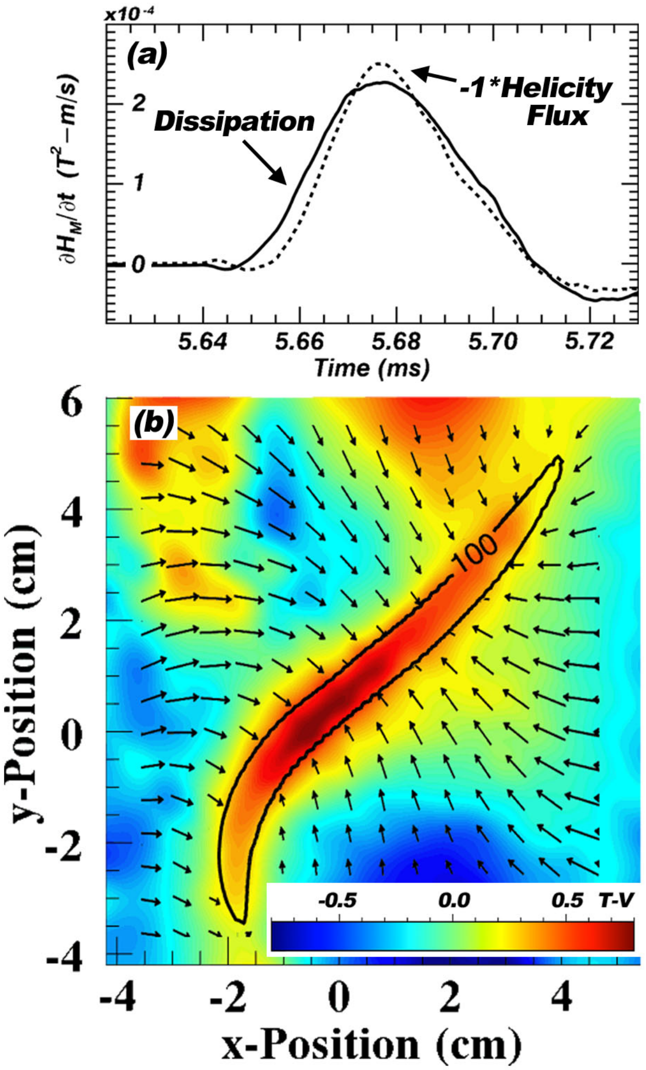

Figure 6.6 – **(a)** The dissipation and influx of electron canonical helicity (Eq. 6.9) inside the QSL (q=100). The addition of the two traces yields the time derivative of K_e during a collision between the two flux ropes. **(b)** The color map represents the dissipation of electron canonical helicity calculated at t=5.67 ms. The arrows represent the influx of the same quantity inside into the QSL calculated at t=5.67 ms where *T-V* is a Tesla-Volt.

dissipation and the total influx of K_e into the QSL are tracked during an experimental reconnection event, plotted in Figure 6.6b. Unlike Figure 6.3, which used only the induced electric field, there is a balance between canonical helicity dissipation and canonical helicity influx. This results in $dK_e/dt \sim 0$ inside the QSL. The inclusion of the electrostatic potential is crucial to the balancing of the two integrals in equation.

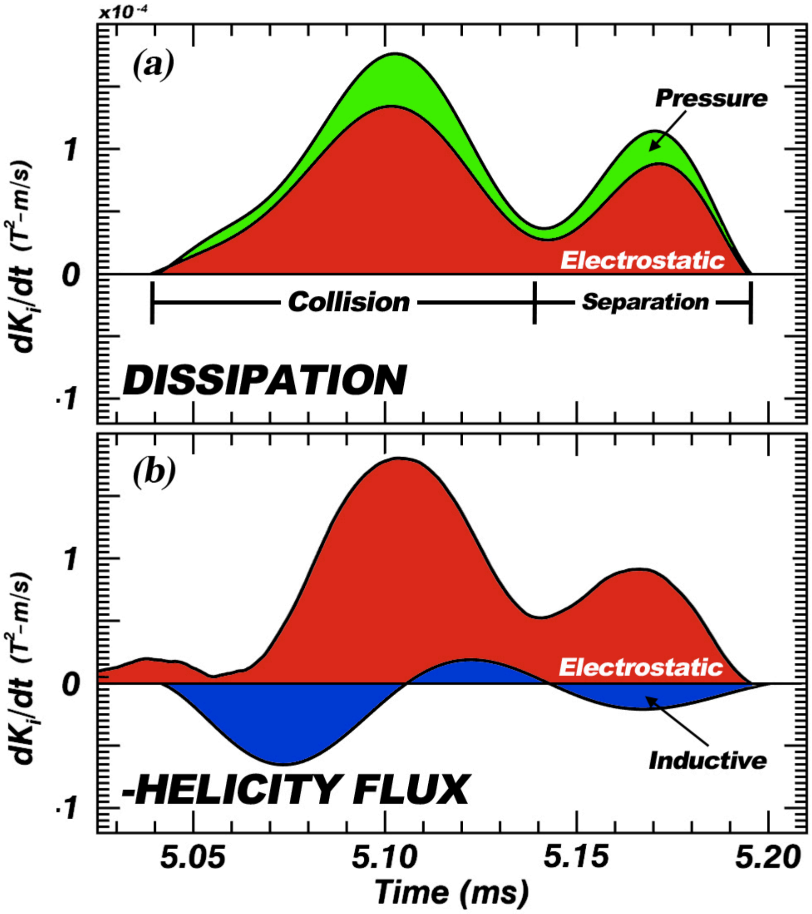

Figure 6.7 – The temporal derivative of ion canonical helicity during the collision of the flux ropes (the peak on the left and their subsequent separation (the peak on the right) **(a)** The dissipation of ion canonical helicity inside the QSL (q=100) according to the volume integral of Eq. 6.11. **(b)** The influx of ion canonical helicity into the QSL calculated using the surface integral of Eq. 6.11. Note: dK_i/dt = a-b~0.

The temporal changes in K_i are shown in Figure 6.7. Figure 6.7a plots the dissipation of K_i inside the QSL, and the Figure 6.7b plots the influx of K_i into the QSL. Both are similar in magnitude and shape. When added together Figure 6.7a and Figure

6.7b yield $dK_i/dt \sim 0$. The figure includes not only the formation of a QSL as the two ropes collide (the first peak) but also the formation of a second QSL that occurs when the flux ropes break apart (the second peak).

The second peak is the consequence of the introduction of the ion flow into the calculations. The second peak corresponds to the times in which the flux ropes are in the process of breaking apart, when another QSL forms between the flux ropes. While there is no appreciable dissipation of K_e during this period, there is for K_i. This is caused by an increase of kinetic ion flow inside the QSL. Considering the energy density of kinetic ion flow ($\frac{1}{2}m_i n\mathbf{v^2}$) within the QSL, the increase in kinetic energy as the flux ropes break apart approximately equals the energy dissipation, $\int_{QSL}(\boldsymbol{E}\cdot\boldsymbol{J})dV$, over the period of QSL formation– 20 Watts over 10 microseconds, or 2×10^{-4} Joules.

6.6 – SUMMARY

In this chapter, two dynamical flux ropes were examined to determine the effects of magnetic reconnection on magnetic helicity. Volumetric measurements of this system were taken of the magnetic field, temperature, density, plasma potential, and ion flows. The importance of measuring each term, which included non-ideal MHD physics, was demonstrated from the fact that the electrostatic component of the electric field, the induced component of the electric field, and the pressure gradient term contribute equally to the resistivity within the region of reconnection.

The flux ropes were driven kink-unstable to trigger repetitive motion. As they interacted, helicity conservation was examined in regions of reconnection. This was done by focusing on the temporal derivative of magnetic helicity instead of its absolute magnitude. The changes to helicity were separated into the dissipation of helicity and the influx of helicity. These were separately tracked within the QSL. If the changes in magnetic helicity are calculated using ideal single fluid MHD physics, helicity is not conserved. If a two-fluid approach that includes the electrostatic fields is used, the dissipation of canonical helicity is balanced by an influx of canonical helicity into the reconnection region. Both electron canonical helicity and ion canonical helicity are individually balanced in a reconnection event.

CHAPTER 7 – *CONCLUSION*

7.1 – SUMMARY OF RESULTS

Two magnetic flux ropes were created in the Large Plasma Device (LAPD) by injecting initially field-aligned currents into a background, helium plasma. The two magnetic flux ropes were driven kink-unstable. They thrash about, collide, and merge. The goal of this experiment was to simulate magnetic flux rope as they are found in the solar atmosphere: where bundles of flux ropes are ubiquitous and the collision between multiple flux ropes can initiate magnetic reconnection. This system was used to test concepts of helicity conservation theory. In the experiment, magnetic reconnection was identified during a collision between the two magnetic flux ropes. A QSL forms as the reconnection occurs. Over the reconnection event, the dissipation and flux of magnetic helicity in the QSL was examined.

First, to aid in the understanding of kink motion, a single flux rope was created in a separate series of experiments. The various components of the motion were identified by the Fourier spectrum of magnetic time traces. There are two distinct types of motion. The first type is associated with elliptical motion of the flux rope in the transverse plane. This motion is highly coherent, repeatable, and pervades the entire experimental volume. This coherent mode manifests as multiple, harmonic, peaks in the Fourier spectrum. The harmonics are the result of flux rope excursions greater than or equal to the original radius of the flux rope. The particulars of this motion depend on the current in the flux rope and the discharge power. An increase in power corresponds to an increased displacement of the flux rope in its elliptical motion.

The second motion is characterized by intermittent pulses seen by magnetic probes, which are sensitive to $\dot{\mathbf{B}}$. These magnetic pulses are associated with a spatially varying electrostatic field inside the flux rope and an induced electric field from the motion of the rope. The intermittency of the pulses prevents three-dimensional, spatial reconstruction. The signals become more intermittent as the current in the flux rope increases and does not appear to be connected with the kink threshold. Simultaneous measurements along the axis of the LAPD observe pulses that are well correlated in space. This suggests that these intermittent pulses are connected to large-scale structures, possibly related to a characteristic orbit of the large-scale flux rope. Complexity-Entropy analysis was performed on the intermittent magnetic time traces. The result showed that the time traces were chaotic.

In the magnetohydrodynamic (MHD) limit, the behavior of magnetic flux ropes is bound by rules of magnetic helicity conservation. Magnetic helicity was examined during a magnetic reconnection event between two magnetic flux ropes. Both MHD theory and an extended MHD model were used and evaluated during reconnection. Volumetric measurements of this system were taken of the magnetic field, electron temperature, density, plasma potential, and ion flows. The importance of measuring each term was demonstrated by the fact that the electrostatic component of the electric field, the induced component of the electric field, and the pressure gradient term contribute equally to the resistivity within the region of reconnection.

To identify regions of magnetic reconnection, a squashing factor, q, is computed for the field line configuration. Regions of large q are identified as quasi-separatrix layers (QSLs). Within the QSL, 0.2 G of magnetic energy is annihilated (approximately 2 mJ, 100 W over 20 μs), determined by measurements of $\mathbf{J} \cdot \mathbf{E}$. By focusing not on the magnitude of magnetic helicity but on its temporal derivative, the dissipation of helicity and the influx of helicity are tracked separately within the QSL.

Using terms only associated with MHD physics, the magnetic helicity is shown to dissipate inside the QSL due to the induced electric field from magnetic reconnection. This dissipation is not balanced by an influx of magnetic helicity into the region. Because the flux ropes are electrostatically negative with respect to the background plasma, the addition of an electrostatic term is required in order for the two to balance. The term was added using a MHD-like fluid theory of magnetic helicity, called canonical helicity [You 2012]. The inclusion an electrostatic term generates additional helicity dissipation ($-\nabla\phi_p \cdot \mathbf{B}$) inside the QSL. This dissipation is balanced by a helicity injection term ($\phi_p\mathbf{B}$). Both electron canonical helicity and ion canonical helicity are separately balanced during a reconnection event. increased flows around the reconnection site.

While previous works have used the conservation of canonical helicity to model astrophysical jets [Lavine 2017] and two, relaxing, magnetic flux ropes [You 2014], this dissertation presents the first experimental measurements of relative canonical helicity. The theoretical model ties electrostatic helicity injection to magnetic fields and flows.

This work demonstrates the importance of theoretical models which do just that. In addition, this work underlines the importance of electrostatic fields within the flux rope currents as well as in the QSL. Specifically the transport of canonical helicity into the QSL was shown to equal the dissipation within it. This has application to solar magnetic flux rope where QSLs have been used to identify magnetic reconnection as well as other types of reconnection events.

APPENDIX A – *FREQUENCY SCALING OF COHERENT ROTATION*

A.1 – INTRODUCTORY REMARKS

Equations 4.1 through 4.3 predict the threshold at which the flux rope becomes kink unstable. However, above the kink threshold ($I_{\mathrm{KS}}/2$), these equations only predict imaginary frequencies. The dispersion relation is given by

$$\frac{\omega^2}{\mathrm{v}_A^2} = \frac{\pi^2}{4L^2} - \frac{k_0^2}{4} \tag{A.1}$$

Despite this fact, the unstable system shows strong, well-defined real frequencies. The scaling of this frequency is not well understood. To that end, the frequency scaling associated with flux rope rotation will be reviewed. A single flux rope will be considered at various experimental parameters. In Section A.5, these measurements will be compared to four hypotheses that have been commonly used to explain its behavior.

A.2 – SCALING WITH MAGNETIC FIELD

Two magnetic flux ropes were separately generated: both with a radius of 3.75 cm and a length of 1100 cm. One flux rope carried 75 Amps of current while the other carried 120 Amps. The background magnetic field was varied between 330 G and 1500

G. Each flux rope was the kink unstable for the external fields used in the experiment. Figure A.1 plots the frequency of coherent rotation as a function of the background magnetic field. For each set of data, the frequency of mode increases with the background field. However, a doubling of the magnetic field does not double the frequency – as one would expect if the rotation of the flux rope were explained by a simple, standing Alfvén wave ($f = \frac{v_A}{2^{3/2}L}$). On interesting feature is that the two curves cross one another such that the dataset for I = 75 A rises above the dataset at 120 A.

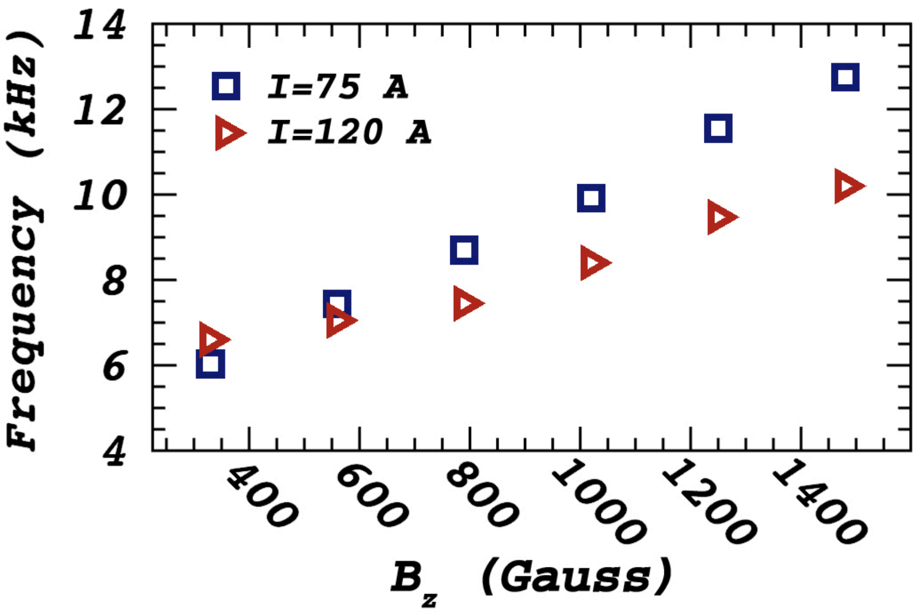

Figure A.1 – The frequency of coherent rotation as a function of the background magnetic field. Two separate flux ropes were generated (a = 3 cm, L = 1100 cm). The two instances are plotted: 1) for a flux rope of 75 A and 2) a flux rope of 120 A.

A.3 – SCALING WITH LENGTH

In a single experiment, the anode was bought closer to the LaB$_6$ cathode such that the length of the flux rope was reduced from 1100 cm to 550 cm. In this way, the character of coherent rotation could be gauged as a function of length. Without explicitly plotting the results, the scaling with the external magnetic field and the current in the rope retained the same form as Figure 4.3 and Figure 4.8. In this instance, however, the frequencies increased by a factor of 1.4.

A.4 – SCALING WITH MASS DENSITY

The LAPD has four working gasses (H, He, Ne, Ar) from which a plasma might be produced. By changing the working gas, the coherent mode may by explored as a function of mass density. This is an important quantity because it affects the Alfvén velocity. A single flux rope was embedded in an argon plasma. The current in the flux rope (a = 3.75 cm, L = 550 cm) was slowly raised until it went kink unstable. Figure A.2 plots the kink transition for the flux rope at two background fields.

Unlike the helium flux rope, drift waves play a dominant role in the transition. Drift waves can be found in flux rope experiments because the flux rope is hotter and denser than the surrounding medium (see Section 3.2). The pressure gradients between the core of the flux rope and the ambient medium are a source of free energy. This drives waves along the pressure gradients of the flux rope with a phase velocity equal to the electron diamagnetic velocity v_{De}. The frequency associated with drift waves [Swanson 1989] is given by

$$f_{De} = \frac{\mathrm{v}_{De}}{2\pi a\,(1 + (k_{\perp}\rho_s)^2)} \tag{A.2}$$

Where $k_{\perp}$ is the perpendicular wave number and ρ_s is the ion sound gyroradius. Using $\mathrm{v}_{De} \sim 4\mathrm{x}10^{5}$ cm-s^{-1} and a flux rope of 10 eV, $k_{\perp}\rho_s \sim 0.5$ for an argon plasma. This places the predicted frequency associated with a drift wave near 15 kHz. In Figure 4.2a, a distinct peak occurs near this frequency, which phases out as the kink instability is triggered. In Figure A.2b, the same mode is broad in character and does not phase out as the flux rope transitions into the coherent mode.

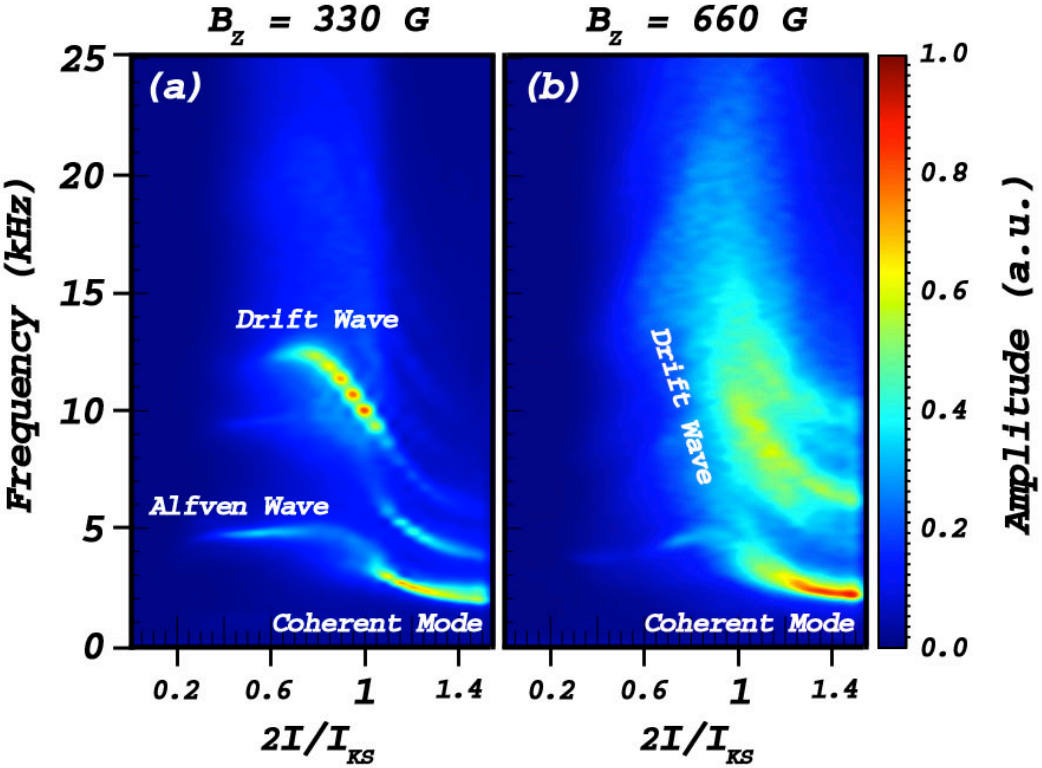

Figure A.2 – **(a)** The transition from a stable to and unstable flux rope in an argon background plasma for B_z = 330 G. **(b)** The transition from a stable to and unstable flux rope in an argon background plasma for B_z = 660 G.

This observed mode is not the standing Alfven wave predicted by Eq. A.1. The frequency predicted by Eq. A.1 is given by

$$f = \frac{v_A}{4L} \tag{A.3}$$

For an Alfvén speed of $7x10^6$ cm-s^{-1} and a length 550 cm, the predicted real frequency is

5 kHz. A faint peak in the spectrum can be observed at this frequency below $I_{KS}/2$ in Figure A.2a. This corresponds to the standing Alfvén, which also phases out as the kink instability is triggered. As it transitions into the coherent mode, frequency drops to 2 kHz. This is approximately *2.5* times lower the frequency observed under the same conditions in helium, close to but not exactly the square root of the mass ratio between argon and helium: $\sqrt{M_{Ar}/M_{He}} = 3.2$

A.5– TESTING OF COHERENT FREQUENCIES.

We explore the factors which determine the frequency of coherent, flux rope behavior. This is defined as the orbital rotation of the flux rope in the plane. Eq. 4.1 with the associated boundary conditions (Eq. 4.2 and Eq. 4.2) fails to produce real frequencies above $I_{KS}/2$. Previous experiments have the sought to explain the observed orbital rotation of the flux rope with a variety of hypotheses. These include orbital rotation driven by a radial electrostatic fields [Berger 2006, Paz-Soldan 2011], axial ion flow [Intrator 2007, Oz 2011, Van Compernolle 2011], modified boundary conditions [Gekelman 2016], and bulk resistivity [Ruytov 2006]. In this section, these hypothesis will be tested by comparing them to the observed scaling of Section 4.5.

A.5.1 – ELECTROSTATICALLY DRIVEN KINK ROTATION

[Bergerson 2006] and [Paz-Soldan 2011] proposed that the orbital rotation of the flux rope was driven by radial electric fields. The flux rope is electrostatically negative with respect to the background plasma (see Chapter 3). A radial electric field points toward the center of the flux rope, and the magnitude of the electric field scales with discharge current. This could explain the increase in frequency which accompanies the increase in flux rope current (Figure 4.3).

An investigation of this hypothesis is considered in two ways: The first deals only with the absolute magnitude of the local, radial electric field at the edges of the flux rope. The second performs a volume-averaged measurement. In the first and simplest case, the radial electric field at the edge of the flux rope is 4 V/cm. With a background magnetic field of 330 G and an orbital radius on the order of 3 cm:

$$f_{rot} = \frac{|E_r|}{|B_z|}\frac{1}{2\pi R_{Orb}} \sim 40\ kHz \tag{A.4}$$

This value is an order of magnitude too large and cannot explain the observed frequencies.

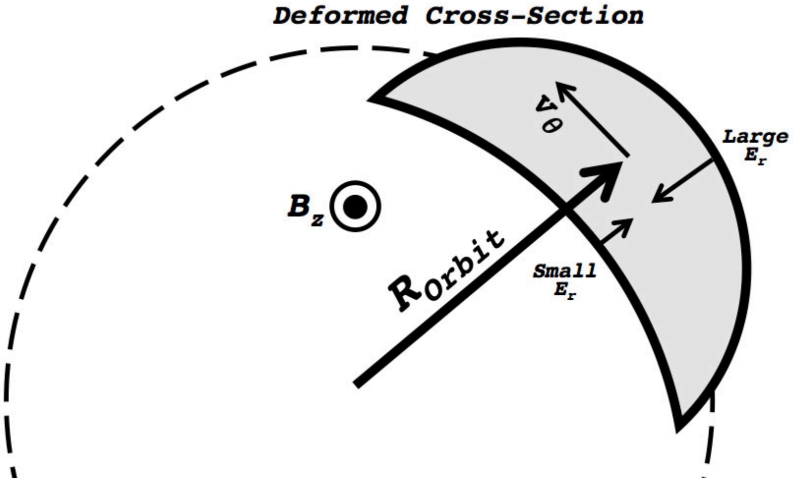

Figure A.3 – A presentation of how symmetry in the electric field can be broken and how it can establish a non-zero, volume-averaged, radial electric field. A radial electric field can be created by the deformation of the x-y cross-section. By centripetal forces, a large electric field manifests on the outer edge resulting in a non-zero electric field in the plane.

In contrast to using a $|E_r|$ at one radial location, the volume-averaged electric field is considered. In order for the volume-averaged electric field to be non-zero, axial symmetry must be broken. Suppose the flux rope is deformed according to the shaded surface in Figure A.4. This would result in a non-zero radial electric field after averaging over the rope, and the flux rope would travel in the same direction of the observed rotation (+θ) in the LAPD.

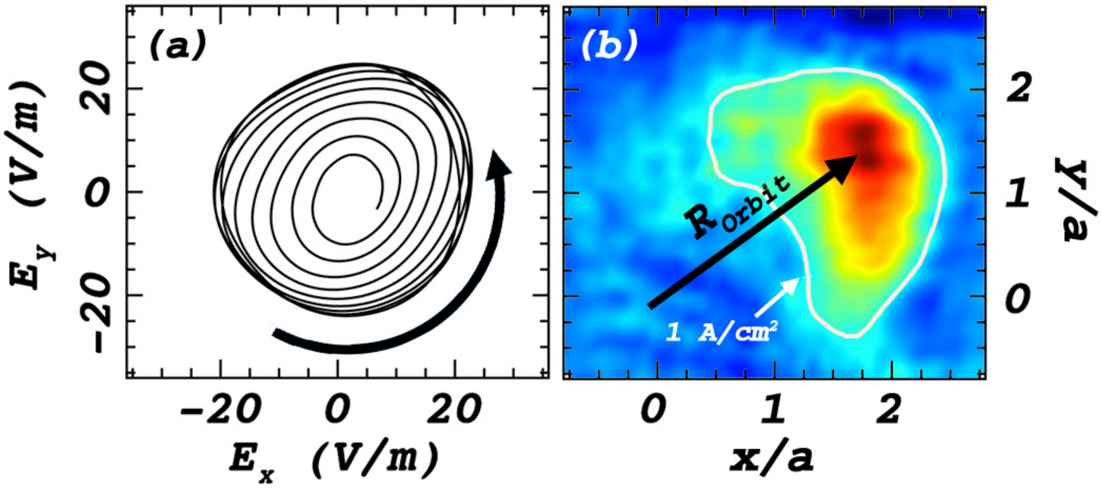

Figure A.4 – **(a)** The volume-averaged electric field vector over several periods of flux rope rotation from $t = 4$ ms to $t = 5$ ms. The vector rotates with the flux rope and produces **E×B** estimates of 2 to 10 kHz **(b)** The instantaneous current density profile as it moves in a circle around the equilibrium position. The current profile deformed into a moon shape.

For a single flux rope experiment (I_{FR} = 120 A, V_D = 220 V, B_z = 330 G, a = 3 cm, L = 1100 cm), the volume-averaged electric field was evaluated. Figure A.4 shows the radial electric field vector over several milliseconds. The vector presents itself moving in a circle with the motion of the flux rope. The resulting estimates of rotation are between 2 and 10 kHz, the correct order of magnitude to explain the phenomena.

Despite being the right order of magnitude, we experimentally verified that the frequency predicted by this hypothesis does not scale properly with B$_z$ ($f \propto 1/B_z$). Similarly, the predicted frequency has amplitude dependence ($\delta B \propto R_{Orb}$) whereas none was observed in the experiment. We rule out this effect, and will not consider the kink mode as the key driver.

A.5.2 – ION FLOW

[Ryutov 2006] introduces a state-state axial ion flow to Eq. 4.1 by applying a Galilean transformation such that the operator $\partial/\partial t$ becomes $\partial/\partial t + \mathrm{v}\,\partial/\partial z$. Modifying Eq. 4.1, the transformed description of the flux rope is

$$\left(\frac{\partial}{\partial t} + \mathrm{v}\frac{\partial}{\partial z}\right)^2 \eta = 2v_A^2\left(\frac{\partial^2\eta}{\partial z^2} + ik_0\frac{\partial\eta}{\partial z}\right) \tag{A.5}$$

When Eq. A.5 is solved and the appropriate boundary conditions imposed, the effect of axial flow is to lower the current threshold sufficient to trigger the instability. This threshold becomes

$$I_{Kink} = \frac{I_{KS}}{2}\sqrt{1 - M_A^2} \tag{A.6}$$

where M_A is the Alfvenic Mach number. As discussed in Chapter 3, this value is approximately $M_A = 0.02$. It is an order of magnitude lower than the flows expressed as a fraction of the sound speed. It is unlikely in the LAPD that the background flows of a flux rope experiment will become supersonic, and therefore, the flow of ions between the cathode and anode have little effect on the kink threshold.

However, small ion flows can introduce substantial real frequencies into the system. Above the critical, current threshold, the real frequencies governing the displacement of the plasma column are given by

$$\mathrm{Re}\,(\omega) = -\frac{\mathrm{v}B_\theta}{aB_z} = -\frac{\pi \mathrm{v}}{L}\frac{I}{I_{KS}} \tag{A.7}$$

Using ion flow as an explanation to the coherent rotation observe in numerous flow rope experiments is appealing because the frequency of the mode scales with the current in the flow ropes. Similarly, the mode is independent of the direction of the external magnetic field, and the negative sign in front of the term predicts the proper direction of rotation ($+\theta$). Using a flux rope 3.75 cm in radius, a background magnetic field $B_z = 330$ G, and $B_\theta = 10$ G, the resulting real frequency is 500 Hz. This is an order of magnitude less than the observed frequencies.

Even if the estimates of axial flow are incorrect, the mode is inconsistent on two points: 1) the theoretical mode is independent of the length of the flux rope and 2) the mode is inversely proportional to the background magnetic field. As stated above, by cutting the length of the flux rope in half, the frequency of rotation increases. To the second point, the frequency of rotation is observed to scales proportionally not inversely proportionally to the background magnetic field.

A.5.3 – MODIFIED BOUNDARY CONDITIONS.

The solution to Eq. 4.1 is sensitive to boundary conditions. A change in the boundary conditions can change threshold at which the flux rope goes kink-unstable. Similarly, a change in the boundary conditions can introduce real frequencies into the dispersion relation above the kink threshold. Because the anode is semi-transparent, the proper boundary conditions are uncertain, and therefore other boundary conditions should be tested. This section changes the boundary condition at the anode in two ways: 1) by including finite sheath resistance at the anode and 2) by changing the angle at which the flux rope meets the anode.

[Ruytov 2006] developed a dimensionless parameter κ to gauges the role of sheath resistance:

$$\kappa = \frac{c_s}{\mathrm{v}_z}\left(\frac{c}{a\omega_{pi}}\right)^2 \sqrt{\beta_e} \tag{A.8}$$

where ω_{pi} is the plasma frequency of ions, and $\beta_e = \frac{8\pi n_e T_e}{B_z^2}$. When $\kappa \gg 1$, the dispersion relation rapidly approaches Eq. A.1. When $\kappa \sim 1$, the dispersion relation yields real frequencies on the same order as the ones observed. The dispersion relation is given by:

$$\tan\left(L\sqrt{\frac{k_0^2}{4}+\frac{\omega^2}{2\mathrm{v}_A^2}}\right) = -\frac{i\kappa\mathrm{v}_A}{\omega}\sqrt{\frac{k_0^2}{2}+\frac{\omega^2}{\mathrm{v}_A^2}} \tag{A.9}$$

Similarly, instead of using Eq. 4.3 as the proper boundary condition, the boundary condition of a vibrating rod with a free end can be used.

$$\left.\frac{\partial\eta}{\partial z}\right|_{z=L} = 0 \tag{A.10}$$

Applying this boundary condition to Eq. 4.1, the following dispersion relation is

$$\tan\left(L\sqrt{\frac{k_0^2}{4}+\frac{\omega^2}{2\mathrm{v}_A^2}}\right) = -\frac{2i}{k_0}\sqrt{\frac{k_0^2}{4}+\frac{\omega^2}{2\mathrm{v}_A^2}} \tag{A.11}$$

Figure A.5 plots the predicted frequencies from Eq. A.1, Eq. A.9, and Eq. A.11 as a function of current in the rope. The calculation uses helium a flux rope with a = 2.5 cm, L = 1100 cm, B_z = 330 G, and n_e = 5×10^{12} cm^{-3}. The data is placed on the same graph for comparison.

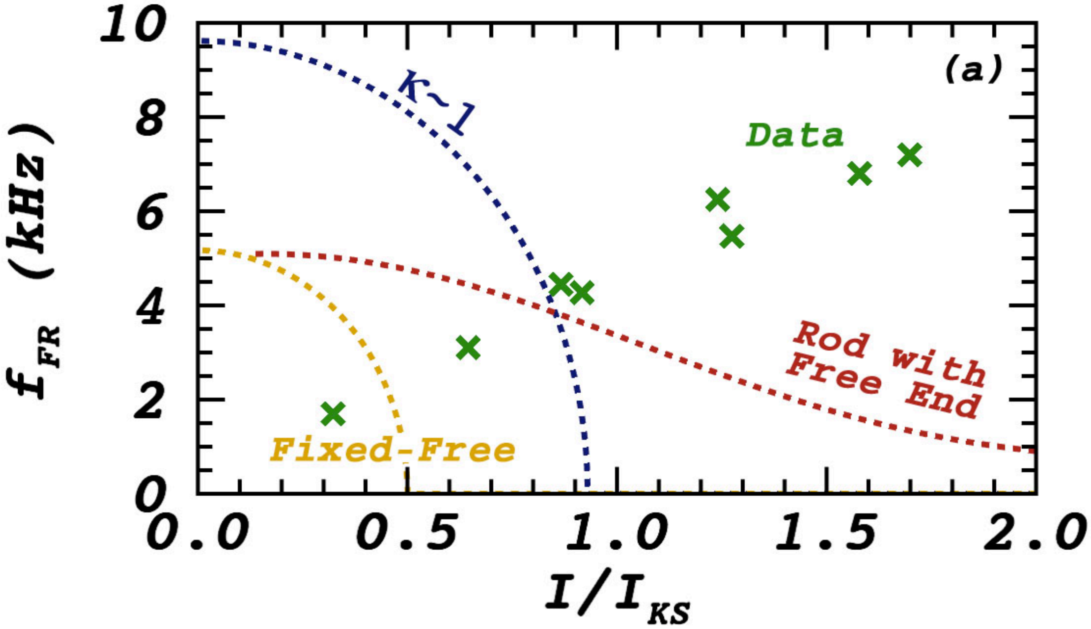

Figure A.5 – **(a)** Three dispersion relations associated with three boundary conditions: a fixed-free boundary condition (Eq. 4.3), a vibrating rod with a free end (Eq. A.11), and a boundary condition with finite sheath resistance $\kappa \sim 1$ at the anode (Eq. A.9). The data is placed on top of these curves to demonstrate incompatibility.

Both Eq. A.9 and Eq. A.11 are beneficial because they produce the frequencies the correct order of magnitude. The dispersion relations scale correctly with the Alfvén speed and the length of the system. They do not scale correctly with the current in the rope. Introducing finite sheath resistance does not produce real frequencies (for the lowest mode) above I_{KS}. Simulating the flux rope as a vibrating rod can introduce real frequencies above the limit I_{KS}. However, these frequencies do not scale in the same direction as the data. Similarly, in the limit of $0 < I_{FR} \ll I_{KS}$, Eq. A.11 predicts an unstable flux rope with $Im(\omega) = \frac{\sqrt{2}\mathrm{v_A} k_0}{\pi}$. In other words, the flux rope is always unstable when this boundary condition is used. This was not observed.

A.*5.4 – BULK RESITIVITY*

A dimensionless parameter is introduced which characterizes the role resistivity on the flux rope system:

$$\zeta = \frac{\pi v_A \tau_R}{L} \tag{A.12}$$

Where $\tau_R = 2\pi a^2 \sigma / c^2$ and σ is the plasma conductivity. In the LAPD with $L \sim 1100$ cm, $a \sim 2.5$ cm, and $\sigma \sim 5.8\times10^{-6}$ s^{-1}: $\tau_R \sim 20$ μs and $\zeta \sim 1$. [Ryutov 2006] points out that at $\zeta \sim 1$ perturbations in the plasma column can have substantial real frequencies above I_{Kink}. These real frequencies are a possible explanation of the orbital rotation seen in the experiments. Modifying the equations of motion to describe the effect of resistivity on a slender plasma column,

$$\omega^2 = 2v_A^2 \left(\frac{i\omega\tau_R}{i\omega\tau_R - 1} k^2 + k_0 k \right). \tag{A.13}$$

In the limit $\omega\tau_R \rightarrow \infty$, the two solutions for k reduce to Eq. 4.13 and Eq. 4.14. Therefore, substituting k_1 and k_2 from Eq. 4.13 and Eq. 4.14 into Eq. A.13:

$$\left(\frac{1}{k_0^2 v_A^2} \right) (i\tau_R)\omega^3 - \left(\frac{1}{k_0^2 v_A^2} \right) \omega^2 + \left(\frac{1}{2} - \frac{1}{8} \frac{I_{KS}^2}{I^2} \right) (i\tau_R)\omega - 1 = 0 \tag{A.14}$$

This is a third order polynomial, which can be solved analytically.

Solving for the real roots of Eq. A.14, the solution can be compared to the data presented above. In Figure A.6, the rotation frequency is again plotted as a function of the background magnetic field. This time, the solution to Eq. A.14 is drawn as a dashed line on top of the data. The theory and the data show good agreement. The two curves cross one another. This is due to an increase in the density of the ropes at 120 Amps. In this instance, the discharge voltage was 220 V (26 kW), leaving the density in the core of the flux rope at $8x10^{12}$ cm.$^{-3}$ In contrast, the flux rope at 75 (a 110 V discharge) has a density of $4x10^{12}$ cm^{-3}. Because increases in the density slows the Alfvén speed, the solution to Eq. A.10 decreases. Similarly, this explains the decrease in frequency when the experiment was switched to an argon plasma.

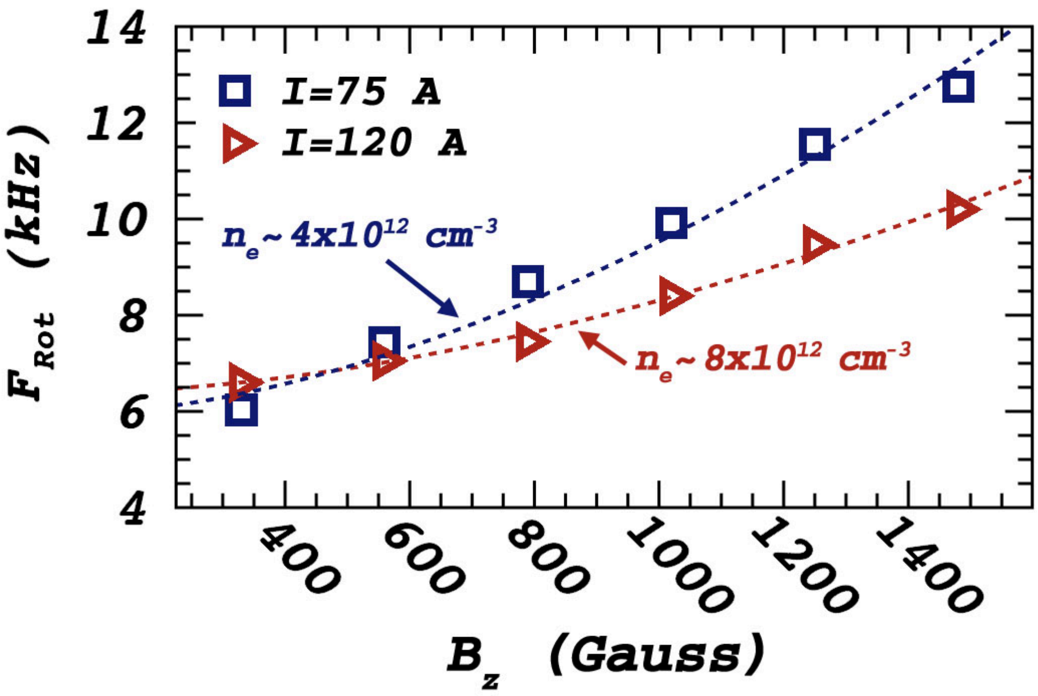

Figure A.6 –A comparison between the observed rotation of a magnetic flux rope (a=3 cm, L=1100 cm) and the frequencies predicted by Eq. 4.25 as a function of background magnetic field. The frequencies scale with the Alfvén velocity. The two curves cross because of an increase in the density for elevated discharge currents.

The predicted scaling of the mode with current is more difficult to compare to the data. When the current in the flux rope increases, there is also a corresponding increase in the temperature and density. This will affect τ_R and the solution to Eq. A.14. However, the key difference between the equations of Section A.5.3 and Eq. A.14 is that the slope of curve is positive instead of negative when $\zeta \sim 1$. The positive increase in frequency with current corresponds to the data and is the same order of magnitude.

Finally, the roots of Eq. A.14 vary as a function of the length of the flux rope. The length of the flux rope is embedded in I_{KS}^2. While measurements were only taken at two different lengths, Eq. A.14 can be used to estimate the effect of length on the frequency. When the length of the flux rope is cut in half, Eq. A.14 predicts an increase in the frequency by a factor between 1.2 and 1.6. This is equal to the observed phenomena.

A.6– SUMMARY OF APPENDIX

A single flux rope was generated in the LAPD. The flux rope was kink unstable and rotates about it equilibrium position. The background magnetic field, the current in the rope, the mass density of the rope, and the length of the flux rope were varied in order to determine the dispersion relation that governs the system. The observe frequency of rotation scales positively with the Alfvén speed. In addition, it also scales positively with the current in the ropes. This scaling was tests against several hypothesis – including orbital rotation driven by a radial electrostatic fields, axial ion flow, modified boundary conditions, and bulk resistivity. Because the Alfven transit time is on the same order as the resistive diffusion time, bulk resistivity is an important part of flux rope dynamics. Introducing resistivity into the dispersion relation predicts frequencies which are the same order of magnitude and scale in the same direction as the observed frequencies.

REFERENCES

Akasofu, S. I. (1979), Magnetospheric substorms and solar flares, *Solar Physics*, 64, 333-348.

Alfvén, H. and Fälthammer, C. G. (1963), *Cosmical Electrodynamics, Fundamental Principles*, Clarendon Press, Oxford.

Amari, T., Luciani, J. F., Mikic, Z., and Linker, J. (1999), A twisted flux rope model for coronal mass ejections and two-ribbon flares, *The Astrophysical Journal Letters*, 529, L49-L52.

Aschwanden, M. J., Wulser, J. P., Nitta, N. V., and Lemen, J. R. (2008), First three-dimensional reconstruction of coronal loops with STERO A and B spacecraft. I. geometry*, Astrophysical Journal*, 679, 827.

Avinash, K. and Fukuyama, A. (1995), Current drive due to fluid helicity, *Physics of Plasmas*, 2, 3539.

Babock, H. W. (1961). The topology of the Sun's magnetic field and the 22-year cycle, *Astrophysical Journal*, 133:572.

Bandt, C. and Pompe, B. (2002), Permutation entropy: a natural complexity measure for time series. *Physical Review Letters*, 88, 174102.

Berger, M. A. (1999), Introduction to magnetic helicity, *Physics of Plasma and Controlled Fusion*, 41, B167-B175.

Berger, M. A. and Field, G. N. (1984), The topological properties of magnetic helicity, *Journal of Fluid Mechanics*, 147, 133.

Bergerson, W. F., Forest, C. B., Fiksel, G., Hannum, D. A., Kenrick, R., Sarff, J. S., and Stembler, S. (2006), Onset and saturation of the kink-instability in a current-carrying line-tied plasma, *Physical Review Letters*, 69, 015004.

Beharrell, M. J. and Wild, J. A. (2012), Stationary flux rope at the southern terminator of Mars, *Journal of Geophysical Research*, 117, A12212.

Bellan, P. M. and Hansen, J. F. (1998), Laboratory simulations of solar prominence eruptions, *Physics of Plasmas*, 5, 1991-2000.

Bellan, P. M. (2000), Spheromaks, *Imperial College Press*, London.

Bickerton, R. J (1958), The amplification of a magnetic field by a high current discharge, *Proceeding of the Physical Society,* 72, 618-624.

Blackman, E. G. (2015), Magnetic helicity and large scale magnetic fields: a primer, *Space Science Reviews*, 188, 59-91.

Bostick, A. B. (1956), Simulation of solar prominence in the laboratory, *Physical Review*, 104, 1191.

Bothmer, V. and Schwenn, R. (1994), Eruptive prominences as sources of magnetic clouds in solar wing, *Space Science Review*, 70, 215-225.

Brookhardt, M. I. (2015), Subcritical onset of plasma fluctuations and magnetic self-organization in a line-tied screw pinch, PhD thesis, University of Wisconsin - Madison.

Burgala, L. F. (1988), Magnetic clouds and force-free fields with constant alpha, *Journal of Geophysical Research*, 93, 7217-7224.

Chen, F. F. (1965), Plasma Diagnostic Techniques, edited by R. H. Huddleston and S. L. Leonard, *Academic, New York*, Chapter 4, 113-200.

Cirtain, J. W., Golub, L., Winebarger, A. R., De Pontieu, B., Kobayashi, J., and Moore, R. L. (2013), Energy release in the solar corona from spatially resolved magnetic braids, *Nature*, 493, 501-503.

Cloutier, P. A., Law, C. C., Crider, D. H., Walker, P. W., Chen Y., Acuña, M. H., Connerney, J. E. P., Lin, R. P., Anderson, K. A., Mitchell, D. L., Carlson, C. W., McFadden, J., Brain, D. A., Rème, H., Mazelle, C., Sauvaud, J. A., d'Uston, C., Virnes, D., Bauer, S. J., and Ness, J. F. (1999), Venus-like interaction of the solar wind with mars. *Geophysical Review Letters*, 26, 2685-2688.

Cooper, C. M., Gekelman, W., and Lucky, Z. (2010), A new large area lanthanum hexaboride plasma source, *Review of Scientific Instruments*, 18, 082503.

Démoulin, P. (2006), Extending the concept of seperatricies to QSLs for magnetic reconnection, *Advances in Space Research*, 37, 1269.

Elphic, R. C. (1979). ISEE observations of flux rope transfer events at the dayside magnetopause, *Geophysical Research Letters*, 6, 33-36.

Ernst, C and Sumners, D. W. (1999), Solving tangle equations arising in a DNA recombination model, *Mathematical Proceedings of the Cambridge Philosophical Society*, 126, 23-36.

Everson, E. T., Pribyl, P., Constantin, C. G., Zylstra, A., Schaeffer, D., Kugland, N. L., and Niemann, C. (2009), Design, construction, and calibration of a three-axis, high frequency magnetic probe (B-dot probe) as a diagnostic of exploding plasma, *Review of Scientific Instruments*, 80, 113505.

Finn, J. M. and Antonsen, T. (1985), Magnetic helicity: what is it and what is it good for, *Comments on Plasma Physics and Controlled Fusion*, 9, 111.

Forbes, T. G. and Isenberg, P. A. (1991), A catastrophe mechanism for coronal mass ejections, *Astrophysical Journal*, 373, 294.

Furno, I., Intrator, T. P., Ryutov, D. D., Abbate, S., Madziwa-Nussinov, T., Light, A., Dorf, L., and Lapenta, G. (2006), Current-driven rotating-kink mode in a plasma column with a non-line-tied-free end, *Physical Review Letters*, 97, 015002.

Gekelman, W., DeHaas, T., Daughton, W., Van Compernolle, B., Intrator, T., and Vincena, S. (2016), Pulsating magnetic reconnection driven by three-dimensional flux rope interactions, *Physical Review Letters*, 116, 235101.

Gekelman, W., Lawrence, E., and Van Compernolle, B. (2012), Three-dimensional reconnection involving magnetic flux ropes, *The Astrophysical Journal*, 753,131.

Gekelman, W., Pribyl, P., Lucky, Z., Drandell, M., Leneman, D., Maggs, J., Vincena, S., Van Compernolle, B., Tripathi, S. K. P., Morales, G., Carter, T. A., Wang, Y., and DeHaas, T. (2016), The upgrade Large Plasma Device, a machine for studying frontier basic plasma physics, *Review of Scientific Instruments,* 87, 025105.

Gekelman, W., Van Compernolle, B., DeHaas, T., and Vincena, S. (2014), Chaos in magnetic flux ropes, *Plasma Physics and Controlled Fusion*, 56, 064002.

Gekelman, W., Vincena, S., Van Compernolle, B., Morales, G. J., Maggs, J. E., Pribyl, P., and Carter, T. A. (2011), The many faces of shear Alfvén waves, *Physics of Plasmas*, 18, 055501.

Goebel, D. M., Hirooka, Y., and Sketchley, T. A. (1985), Large-area lanthanum hexaboride electron emitter, *Review of Scientific Instruments*, 56, 1717.

Goldstein, H. (1983), On the field configuration of magnetic clouds in Solar Wind Five, *NASA Conference Publication*, 2280, 731-733.

Golub, L., Bookbinder, J., DeLuca, E., Karovska, M., Warren, H., Schrijver, C. J., Shine, R., Tarbell, T., Title, A., Wolfson, J., Handy, B., and Kankelborg, C. (1999), A new view of the solar corona for the transition region and coronal explorer (TRACE), *Physics of Plasmas*, 6, 2205.

Gosling, J. T. (1997), Coronal mass ejections: an overview, Coronal Mass Ejections: Geophysical Monograph, 99, 9-16

Grotian, W. (1939), Zur frage der duetung der linien im spectrum der sonnenkorona, *Naturwissenschaften*, 27, 214.

Hansen, J. F., Tripathi, S. K. P., and Bellan, P. M. (2004), Co- and counter-helicity interaction between two adjacent prominences, *Physics of Plasmas*, 11, 3177.

Hershkowitz, N. (1989), Plasma Diagnostics, *Academic, New York*, Vol. 1, Chapter 3, 113-183.

Hesse M, Forbes, T., And Birn, J. (2005), On the relation between reconnecting magnetic flux and parallel electric fields in the solar corona, *Astrophysical Journal,* 631, 1227.

Hobbs, G. D. and Wesson, J. A. (1967), Heat flow through a Langmuir sheath in the presence of electron emission, *Plasma Physics*, 9, 85-87.

Hornung, G., Nold, B., Maggs, J. E., Morales, G. J., Ramisch, M., and Stroth, U. (2011), Observation of exponential spectra and Lorentzian pulses in TJ-K stellarator. *Physics of Plasmas*, 18, 082303.

House, L. L. and Berger M. A. (1987), The ejection of helical field structures through the outer corona, *The Astrophysical Journal*, 323, 406-413.

Hsu, S. C. and Bellan, P. M. (2003), Experimental identification of the kink instability as poloidal flux amplification mechanism for coaxial gun spheromak formation. *Physical Review Letters*, 90, 215002.

Hu, Q. and Dasgupta, B. (2005), Calculation of magnetic helicity of cylindrical flux rope, *Geophysical Research Letters*, 32, L12109.

Huddis, M. and Lidsky, L. M. (1970), Directional Langmuir probe, *Journal of Applied Physics*, 41, 5011.

Hutchinson, I. H. (1988), Ion collection by probes in strong magnetic field with plasma flow, *Physical Review A*, 37, 4358.

Hutchinson, I. H. (2003), Ion collection by a sphere in a flowing plasma: 2. non-zero Debye length, Plasma Physics and Controlled Fusion, 45, 1477-1500.

Intrator, T. P., Furno, I., Ryutov, D. D., Lapenta, G., Dorf, L., and Sun, X. (2007), Long-lifetime current driven rotating kink modes in a non-line-tied plasma column with a free end, *Journal of Geophysical Research*, 112, A05S90.

Intrator, T. P., Sun, X., Lapenta, G., Dorf, L., and Furno, I. (2009), Experimental onset threshold and magnetic pressure pile-up for 3d reconnection, *Nature Physics*, 5, 521.

Jensen, T. H. and Chu, M. S. (1984), Current drive and helicity injection, *Physics of Fluids*, 27, 2881.

Kemp, R. F., and Sellen Jr., J. M. (1966), Plasma potential measurements by electron emissive probes, *Review of Scientific Instruments*, 37, 455.

Klein, L. W. and Burlaga, L. F. (1982), Interplanetary magnetic clouds at 1AU, *Journal of Geophysical Research*, 87, 113-141.

Kruskal, M. D., Johnson, J. L., Gottlieb, M. B., and Goldmand, L. M. (1958), Hydromagnetic instability in a stellarator, *Physics of Fluids*, 1, 421.

Kulsrud, R. M. and Zweibel, E. G. (2008), On the origin of cosmic magnetic fields, *Report on the Progress in Physics*, 71, 046901.

Langmuir, I. (1923), The pressure effect and other phenomena in gaseous discharges, *Journal of the Franklin Institute*, 196, 751-762.

Lavine, E. S. and You, S (2017), The topology of canonical flux tubes in flared jet geometry, *The Astrophysical Journal*, 835, 89.

Lawrence, E. and Gekelman, W. (2009), Identification of a quasiseparatrix layer in a reconnecting laboratory magnetoplasma, *Physical Review Letters*, 102, 105002.

Lehn, J. –M. (1995), Supramolecular Chemistry: Concepts and Perspectives, VCH, Weinheim, Germany.

Leneman, D. and Gekelman, W. (2001), A novel angular motion feedthrough, *Review of Scientific Instruments*, 72, 3473.

Leneman, D., Gekelman, W., and Maggs, J. (2006), The plasma source of the Large Plasma Device at University of California, Los Angeles, *Review of Scientific Instruments,* 77, 015108.

Li, H., Lapenta, G., Finn, J. M., and Solgate, S. A. (2006), Modeling the large-scale structures of astrophysical jets in the magnetically dominated limit, *The Astrophysical Journal*, 643, 92-100.

Low, B. C. (1994), Magnetohydrodynamic processes in the solar corona: flares, coronal mass ejections, and magnetic helicity, *Physics of Plasmas* 1, 1684.

Maggs, J. and Morales, G. (2012), Exponential power spectra, deterministic chaos and Lorentzian pulses in plasma edge dynamics, *Plasma Physics and Controlled Fusion*, 54, 124041.

Maggs, J., Rhodes, T., and Morales, G. (2015), Chaotic density fluctuations in L-mode plasmas of the DIII-D tokamak, *Plasma Physics and Controlled Fusion*, 57, 045004.

Mandelbrot, B. B. and Van Ness, J. W. (1968), Fractional Brownian motion, factional noise and applications, *SIAM Review*, 10, 422-437.

Martin, M. J., Bonde, J., Gekelman, W., and Pribyl, P. (2015), A resistively heated CeB_6 emissive probe, *Review of Scientific Instruments*, 86, 053507.

Martin, M. T., Plastino, A., and Rosso, O. (2006), Generalized statistical complexity measures: geometrical and analytical properties, *Phyisca Scripta A*, 369, 439.

Marubashi, K. (1984), Dynamics of solar wind plasma clouds produced by disappearing filaments, paper presented at the Join US-Japan Seminar on Recent Advances in the understanding of Structure and Dynamics of the Heliosphere during the Current Maximum and Declining Phase of Solar Activity, Kyoto, Japan, November 5-9.

Marubashi, K. (1997), Interplanetary magnetic flux ropes and solar filaments, Coronal Mass Ejections: Geophysical Monograph, 99, 147-156.

Moffat, H. K. (1978), Magnetic field generation in electrically conducting fluids, *Cambridge University Press*, Cambridge, 148.

Øieroset, M., Phan, T. D., Eastwood, J. P., Fujimoto, M., Daughton, W., Shay, M. A., Angelopoulos, V., Mozer, F. S., McFadden, J. P., Larson, D. E., and Glassmeier, K. H. (2011), Direct evidence for a three-dimensional magnetic flux rope flanked by two active magnetic reconnection X lines at Earth's magnetopause, *Physical Review Letters*, 207, 165007.

Oksuz, L. and Hershkowitz, N. (2004), Understanding Mach probes and Langmuir probes in a drifting, unmagnetized, non-uniform plasma, *Plasma Sources Science and Technology*, 13, 263-271.

Oliveira, S. R. and Tajima, T. (1995), Generalized relaxation theory and vortices in plasmas, *Physical Review E*, 52, 4287

Oz, E., Myers, C. E., Yamada, M., Ji, H., Kulsrud, R. M., and Xie, J. (2011), Experimental verification of the Kruskal-Shafranov stability limit in line-tied partial-toroidal plasmas, *Physics of Plasma*, 18, 102107.

Pace, D.C. (2009), Spontaneous thermal waves and exponential spectra associated with a filamentary pressure structure in a magnetized plasma, PhD Thesis, UCLA.

Pace, D. C., Shi, M., Maggs, J. E. Morales, G. J., and Carter, T. A. (2008), Exponential frequency spectrum in magnetized plasmas, *Physical Review Letters*, 101, 085001.

Parker, E. (1983), Magnetic neutral sheets in evolving field. I. General Theory. *Astrophysical Journal*, 264, 635-641.

Parnell, C. E. and Priest, E. R. (1994), The three-dimensional structure of x-ray bright points, *Solar Physics*, 151, 57-74.

Paz-Soldan, C., Brookhart, M. I., Clinch, A. J., Hannum, D. A., and Forest, C. B. (2011), Two-dimensional axisymmetric and three-dimensional helical equilibrium in the line-tied screw pinch, *Physics of Plasma*, 18, 052114.

Pfister, H. (1991), Dynamics and interaction of plasma currents with large self-magnetic fields and their relaxation toward a force-free configuration, PhD thesis, UCLA.

Pfister, H. and Gekelman, W. (1991), Demonstration of helicity conservation during magnetic reconnection using Christmas ribbons, *American Journal of Physics*, 59, 497.

Potemra, T. A. (1988). Birkeland currents in the earth's magnetosphere, *Astrophysics and Space Science*, 144, 155-169.

Pribyl, P. and Gekelman, W. (2004), 24kA solid state switch for plasma discharge experiments, *Review of Scientific Instruments*, 75, 669.

Priest, E. R. (1976), Current sheet models of solar flares, *Solar Physics*, 47, 41-75.

Priest, E. R. and Démoulin, P. (1995), Three-dimensional magnetic reconnection without null points, *Journal of Geophysical Research*, 100, 23443.

Rasmussen, E. N. and Blanchard, D. O. (1999), A baseline climatology of sounding-derived supercell and tornado forecast parameters, *Weather Forecasting*, 13, 1148-1164.

Ressel, C. T. and Elphic, R. C. (1979). Observation of magnetic flux rope in the venus ionosphere, *Nature*, 279, 616-618.

Rosso, O., Larrondo, H., Martin, M., Plastino, A., and Fuentes, M. (2007), Distinguishing noise from chaos, *Physical Review Letters*, 99, 154102.

Russel, C. T., Priest, E. R., and Lee, L. C. (1990), Physics of magnetic flux ropes*, Washington DC American Geophysical Union Geophysical Monograph Series*, 58.

Rust, D. M. and Kumar, A. (1994), Helicity magnetic fields in filaments, *Solar Physics*, 155, 69-97.

Ryutov. D. D., Furno, I., Intrator, T. P., Abbate, S., and Madziwa-Nussinov, T. (2006), Phenomenological theory of the kink instability in a slender plasma column, *Physics of Plasmas*, 13, 032105.

Schrijver, K. (2007), Braiding-induced interchange reconnection of the magnetic field and the width of solar coronal loops, *Astrophysical Journal*, 662, L119-L122.

Schmieder, B., Raadu, M. A., and Malherbe, J. M. (1985), Twisting motion in a disturbed solar filament, *Astronomy and Astrophysics*, 142, 249-255.

Schwager, L. A. (1993), Effects of secondary and thermionic electron emission on the collector and source sheaths of a finite ion temperature plasma using kinetic theory and numerical simulation, *Physics of Plasmas* 5, 631.

Shafranov, V. D. (1956), The stability of a cylindrical gaseous conductor in a magnetic field, *Atomic Energy*, 5 709-713.

Slavin, J. A., Lepping, R. P., Gjerloev, J., Goldstein, M. L., Fairfield, D. H., Acuna, M. H., Balogh, A., Dunlop, M., Kivelson, M. G., Khurana, K., Fazakerley, A., Owen, C. J., Reme, H., and Bosqued, J. M. (2003), Cluster electric current density measurements within a magnetic flux rope in the plasma sheet, *Geophysical Research Letters*, 30, 1362.

Spruit, H. C. and Scharmer, H. C. (2006), Fine structure, magnetic field and heating of sunspot penumbrae, *Astronomy and Astrophysics*, 447, 343-354.

Stangeby, P. C. (1984), Measuring plasma drift velocities in tokamak edge plasma using probes. *Physics of Fluids*, 27, 2699.

Steinhauer, L. C. and Tajima, T. (1997), Relaxation of a two-species magnetofluid, *Physical Review Letter*, 79, 3423.

Sun, X., Intrator, T. P., Dorf, L., Sears, J., Furno, I., and Lapenta, G. (2010), Flux rope dynamics: experimental study of bouncing and merging, *Physical Review Letters*, 105, 255001.

Swanson, D. G. (1989), Plasma Waves, Academic Press, New York, 286.

Taylor, J. B. (1974). Relaxation of toroidal plasma and generation of reverse magnetic fields, *Physical Review Letters*, 33, 1139-1141.

Titov, G., Hornig, G., and Démoulin, P. (2002), Theory of magnetic connectivity in the solar corona, *Journal of Geophysical Research*, 107, SSH 3-1.

Török, T., Kliem, B., and Titove, V.S. (2004), Ideal kink instability of a magnetic loop equilibrium, *Astronomy and Astrophysics*, 413, L27.

Tripathi, S. K. P., Bellan, P. M., and Yun, G. S. (2007), Observations of kinetic plasma jets in a coronal-loop simulation experiment, *Physical Review Letters*, 89, 135002.

Tripathi, S. K. P. and Gekelman, W. (2013), Dynamics of an erupting arched magnetic flux rope in a laboratory plasma experiment, *Solar Physics*, 0038-0938.

Turner, L. (1986), Hall effects on magnetic relaxation, *IEEE Transactions on Plasma Science*, 14, 849.

Van Compernolle, B. and Gekelman, W. (2012), Morphology and dynamics of three interacting kink-unstable flux rope in a laboratory magnetoplasma, *Physics of Plasmas*, 19, 102102.

Van Compernolle, B. Gekelman, W., Pribyl, P., and Cooper, C. M. (2011), Wave and transport studies utilizing dense plasma filaments generated with a lanthanum hexaboride cathode, *Physics of Plasmas,* 18, 123501.

Webb, D. F. (1995), Coronal mass ejections: the key to major interplanetary and geomagnetic disturbances, *Reviews of Geophysics, Supplement*, 33, 577-583.

Wendel, D. E., Olson, D. K., Hesse, M., Aunai, N., Kuznetsov, M., Karimabadi, H., Daughton, W., and Adrian, M. L. (2013), The relation between reconnection flux, the parallel electric field, and the reconnection rate in a three-dimensional kinetic simulation of magnetic reconnection, *Physics of Plasmas*, 20, 122105.

Ye, M. Y. and Takamura, S. (2000), Effect of space-charge limited emission on measurements of plasma potential using emissive probes, *Physics of Plasmas*, 7, 3457.

You, S. (2012), The transport of relative canonical helicity, *Physics of Plasmas* 19, 092107.

You, S. (2014), A two-fluid helicity transport model for flux-rope merging, Plasma *Physics and Controlled Fusion*, 56, 064007.

You, S. (2015), A field theory approach to the evolution of canonical helicity and energy, *Physics of Plasmas*, 23, 072108.

Zhang, J., Cheng, X., and Ding, M. D. (2012), Observations of an evolving magnetic flux rope prior to and during a solar eruption, *Nature Communications 3*, Article number: 474.

Zuin, M., Cavazzana, R., Martines, E., Serianni, G., Antoni, V., and Bagatin, M. (2004), Kink instability in applied-field magneto-plasma-dynamic thrusters, *Physical Review Letters*, 92, 225003.